

Institute for Biochemistry and Biology

Physical Biochemistry

The Role of Protein Metal Complexes in the Mechanics of *Mytilus californianus* Byssal Threads

**Dissertation for the attainment of the academic degree of
„doctor rerum naturalium“
(Dr. rer. nat.)**

**Submitted to the Mathematics/Natural Sciences Faculty
at the University of Potsdam**

by

Dipl. - Biol. Clemens Nikolaus Zeno Schmitt

Potsdam, 24 March 2015

This work is licensed under a Creative Commons License:
Attribution 4.0 International
To view a copy of this license visit
<http://creativecommons.org/licenses/by/4.0/>

Published online at the
Institutional Repository of the University of Potsdam:
URN [urn:nbn:de:kobv:517-opus4-74216](http://nbn-resolving.org/urn:nbn:de:kobv:517-opus4-74216)
<http://nbn-resolving.de/urn:nbn:de:kobv:517-opus4-74216>

To my parents and grandparents,
who taught me the importance of asking questions,
and to my son Cajus who reminded me of this.

Für meine Eltern und Großeltern,
die mir beigebracht haben wie wichtig es ist Fragen zu stellen,
und für meinen Sohn Cajus, der mich daran erinnert hat.

DECLARATION OF ORIGINALITY / EIGENSTÄNDIGKEITSERKLÄRUNG

I hereby declare, that this thesis work "The Role of Protein Metal Complexes in the Mechanics of Mytilus californianus Byssal Threads" is my own work and that only the denoted resources were used. In this or similar form this thesis work has not been published or submitted for the award of any other degree.

Hiermit versichere ich, dass ich die vorliegende Arbeit zum Thema "The Role of Protein Metal Complexes in the Mechanics of Mytilus californianus Byssal Threads" selbständig und unter ausschließlicher Verwendung der angegebenen Literatur und Hilfsmittel erstellt habe. Die Arbeit wurde bisher in gleicher oder ähnlicher Form keiner anderen Prüfungsbehörde vorgelegt und auch nicht veröffentlicht.

Potsdam, 24 March 2015.

Clemens Schmitt

ABSTRACT

Protein-metal coordination complexes are well known to function as active centers in enzymatic catalysis and to contribute to signal transduction, gas transport and hormone function. Additionally, they are now known to contribute as load-bearing cross-links to the mechanical properties of a handful of biological materials, including the jaws of Nereis worms and the byssal threads of marine mussels. The primary aim of this thesis work is to better understand the contribution of protein-metal cross-links to the mechanical properties of biological materials, using the mussel byssus as a model system. Specifically, the focus is on the role of histidine-metal cross-links as sacrificial bonds in the fibrous core of the byssal thread (chapter 4) and L-3,4-dihydroxyphenylalanine (DOPA)-metal bonds in the protective thread cuticle (chapter 5).

Byssal threads are protein fibers, which mussels use to attach to various substrates at the seashore. These relatively stiff fibers have the ability to extend up to about 100% strain, dissipating large amounts of mechanical energy from crashing waves. Remarkably, following damage from cyclic loading, initial mechanical properties are subsequently recovered by a material-intrinsic self-healing capability. Histidine residues coordinated to transition metal ions in the proteins comprising the fibrous thread core have been suggested as reversible sacrificial bonds that contribute to self-healing; however, this remains to be substantiated *in situ*. In the first part of this thesis, the role of metal coordination bonds in the thread core was investigated using several spectroscopic methods. In particular, X-ray absorption spectroscopy (XAS) was applied to probe the coordination environment of zinc in *Mytilus californianus* threads at various stages during stretching and subsequent healing. Analysis of the extended X-ray absorption fine structure (EXAFS) suggests that tensile deformation of threads is correlated with the rupture of Zn-coordination bonds and that self-healing is connected with the re-organization of Zn-coordination bond topologies rather than the mere re-formation of ruptured Zn-coordination bonds. These findings have interesting implications for the design of self-healing metallopolymers.

The byssus cuticle is a protective coating surrounding the fibrous thread core that is both as hard as an epoxy and extensible up to 100% strain before cracking. It was shown previously that cuticle stiffness and hardness largely depend on the presence of Fe-DOPA coordination bonds. However, the byssus is known to concentrate a large variety of metals from seawater, some of which are also capable of binding DOPA (e.g. V). Therefore, the question arises whether natural variation of metal composition can affect the mechanical performance of the byssal thread cuticle. To investigate this hypothesis, nanoindentation and confocal Raman spectroscopy were applied to the cuticle of native threads, threads with metals removed (EDTA treated), and threads in which the metal ions in the native tissue were replaced by either Fe or V. Interestingly, replacement of metal ions with either Fe or V leads to the full recovery of native mechanical properties with no statistical difference between each other or the native properties. This likely indicates that a fixed number of metal coordination sites are maintained within the byssal thread cuticle – possibly achieved

during thread formation – which may provide an evolutionarily relevant mechanism for maintaining reliable mechanics in an unpredictable environment.

While the dynamic exchange of bonds plays a vital role in the mechanical behavior and self-healing in the thread core by allowing them to act as reversible sacrificial bonds, the compatibility of DOPA with other metals allows an inherent adaptability of the thread cuticle to changing circumstances. The requirements of both of these materials can be met by the dynamic nature of the protein-metal cross-links, whereas covalent cross-linking would fail to provide the adaptability of the cuticle and the self-healing of the core. In summary, these studies of the thread core and the thread cuticle serve to underline the important and dynamic roles of protein-metal coordination in the mechanical function of load-bearing protein fibers, such as the mussel byssus.

TABLE OF CONTENTS

Abstract	I
Table of Contents	III
List of Figures.....	V
List of Tables.....	VII
List of Abbreviations.....	VIII
1 Introduction	1
2 State of the Art.....	4
2.1 Mytilus Byssal Threads	4
2.1.1 Byssus Morphology and Function	4
2.1.2 The Core of Byssal Threads	5
2.1.3 The Cuticle of Byssal Threads	8
2.1.4 The Byssal Thread Formation Process.....	10
2.1.5 Byssal Threads as a Model Material for the Study of Metal-Based Cross-Linking	12
2.1.6 Mussel-Inspired Polymers	12
2.2 Theory of Applied Methods.....	13
2.2.1 X-Ray Absorption Spectroscopy	13
2.2.2 Raman Spectroscopy	23
2.2.3 Inductively Coupled Plasma - Optical Emission Spectrometry (ICP-OES)	30
2.2.4 Amino Acid Analysis	32
2.2.5 Nanoindentation	33
3 Materials	36
3.1 Byssal Threads	36
3.2 Standards and Other Chemicals	36
4 Core	37
4.1 Aims of This Study	37
4.2 Experimental Procedures	38
4.2.1 Inductively Coupled Plasma - Optical Emission Spectrometry (ICP-OES)	38
4.2.2 X-Ray Fluorescence (XRF)	38
4.2.3 Raman Spectroscopy	38
4.2.4 X-Ray Absorption Spectroscopy (XAS).....	39
4.3 Results.....	43
4.3.1 Resting State.....	43

4.3.2	Tensile Loading	47
4.4	Discussion	55
5	Cuticle.....	60
5.1	Aims of This Study	60
5.2	Experimental Procedures	61
5.2.1	Sample Preparation	61
5.2.2	Inductively Coupled Plasma - Optical Emission Spectrometry (ICP-OES)	62
5.2.3	Amino Acid Analysis	62
5.2.4	Raman Spectroscopy	62
5.2.5	Nanoindentation	63
5.3	Results.....	64
5.3.1	Inductively Coupled Plasma - Optical Emission Spectrometry (ICP-OES)	64
5.3.2	Amino Acid Analysis	66
5.3.3	Raman Spectroscopy	67
5.3.4	Nanoindentation	69
5.4	Discussion	72
6	Conclusions and Outlook.....	75
7	References.....	79
8	Appendix	89
8.1	Assessment of the Effects of Drying and Relaxation on Byssal Threads.....	89
8.2	Alternative EXAFS Fitting Results For N = 4	91
9	Acknowledgements.....	93

LIST OF FIGURES

Figure 1 Mussel of the species <i>Mytilus californianus</i> with attached byssal threads.....	2
Figure 2 Schematic drawing of the <i>Mytilus</i> byssus.....	5
Figure 3 Stress vs. strain plot of cyclic tensile loading of the distal byssal thread portion of <i>M. californianus</i>	7
Figure 4 ESEM micrograph of a <i>M. galloprovincialis</i> byssal thread ruptured during tensile loading.....	6
Figure 5 TEM micrograph of a transverse cross section of a <i>M. californianus</i> byssal thread cuticle	10
Figure 6 Summary of events taking place when x-rays are absorbed by an atom.....	13
Figure 7 X-ray absorption spectrum of ZnO at the Zn K-edge	15
Figure 8 The standard XAS setup	20
Figure 9 Diagram of transitions between vibrational energy levels corresponding to the process of IR absorption/emission, Rayleigh and Raman scattering.....	24
Figure 10 Definition of coordinate system and sample orientation applied in Raman measurements.....	28
Figure 11 Diagram of the basic process of resonance Raman scattering.....	30
Figure 12 The Grotrian diagram of atomic hydrogen	31
Figure 13 Load displacement diagram of a typical indentation experiment.....	33
Figure 14 Side view of a typical indentation experiment	34
Figure 15 Schematic drawing of the sample preparation for tensile testing and subsequent XAS measurements	40
Figure 16 Concentrations of copper (Cu) and zinc (Zn) in native byssal threads from <i>M. californianus</i>	43
Figure 17 XRF spectrum of the <i>M. californianus</i> byssal thread core	44
Figure 18 Isotropic Raman spectrum and second derivative of the amide I region of the core of native <i>M. californianus</i> distal byssal threads.....	45
Figure 19 XANES spectra at the Zn K-edge (9659 eV) of unstretched byssal threads and organic materials coordinating Zn by histidine or imidazole.....	46

- Figure 20** XANES spectra at the Zn K-edge (9659 eV) of byssal threads at 0%, 10%, 25% and 40% strain, as well as threads stretched to 25% and relaxed, and stretched to 25% and healed for 5 days 48
- Figure 21** R-space EXAFS of the XAFS data and the fits, of byssal threads during tensile loading, after relaxation and after healing. The insets show the corresponding k-space data 50
- Figure 22** Visualization of EXAFS fitting results for Zn K-edge spectra of *M. californianus* byssal threads prior to and during tensile loading, after relaxation and after healing 52
- Figure 23** Visualization of EXAFS fitting results for Zn K-edge spectra of *M. californianus* byssal threads prior to and during tensile loading..... 53
- Figure 24** Visualization of EXAFS fitting results for Zn K-edge spectra of *M. californianus* byssal threads prior to and during tensile loading, after relaxation and after healing 54
- Figure 25** Model of the events taking place during tensile deformation, relaxing and healing of byssal threads, as derived from the combination of XAS results and the current knowledge of the system 58
- Figure 26** Schematic representation of the grouping of samples used in the cuticle study, and how individual threads were split for the different measurements..... 61
- Figure 27** ICP-OES screening of *M. californianus* byssal threads for metals with known ability to form tris-DOPA-metal complexes 64
- Figure 28** Concentrations of iron (Fe), vanadium (V) and calcium (Ca) in native threads and threads treated with EDTA..... 65
- Figure 29** Concentrations of iron (Fe), vanadium (V) and calcium (Ca) in native threads, threads treated with EDTA and EDTA treated threads subsequently soaked in a FeCl_3 or VCl_3 solution..... 65
- Figure 30** Amino acid analysis elution profile of the distal portion of byssal threads from the species *M. californianus*, collected at a wavelength of 570nm 66
- Figure 31** Summary of the Raman investigations on the DOPA-metal interaction of native threads, threads treated with EDTA and EDTA-treated threads subsequently soaked in metal solutions 69
- Figure 32** Comparison of measured reduced elastic modulus (E_r) and hardness (H) values. Each boxplot presents the measured distribution of values per treatment group..... 70
- Figure 33** Comparison of measured reduced elastic modulus (E_r) and hardness (H) values. Each boxplot presents the measured distribution of values per sample 70

Figure 34 Correlation between the concentration of iron and vanadium and the mechanical performance determined by nanoindentation for native cuticles, cuticles treated with EDTA and EDTA-treated cuticles subsequently soaked in metal solutions.....	71
Figure 35 Stress reduction of a byssal thread under wet conditions after deformation to 10% strain and stress increase of a thread stretched under wet conditions to 10% strain and subsequently dried.....	89
Figure 36 Stress reduction of a byssal thread under wet conditions after deformation to 25% strain and stress increase of a thread stretched under wet conditions to 25% strain and subsequently dried.....	90
Figure 37 Stress reduction of a byssal thread under wet conditions after deformation to 40% strain and stress increase of a thread stretched under wet conditions to 40% strain and subsequently dried.....	90

LIST OF TABLES

Table 1 Factors determining the IR and Raman activity of vibrations for a linear triatomic molecule.....	27
Table 2 EXAFS fitting results for Zn K-edge spectra of <i>M. californianus</i> byssal threads prior to and during tensile loading, after relaxation and after healing.....	51
Table 3 Measures derived from the EXAFS fitting results prior to and during tensile loading, after relaxation and after healing.....	51
Table 4 Amino acid composition of distal thread portions of <i>M. californianus</i> compared to <i>M. galloprovincialis</i> and <i>M. edulis</i>	67
Table 5 Assignments of observed Raman shifts and comparison with literature values.....	68
Table 6 Mean values of elastic modulus E_r and hardness H of measurements grouped by treatment.....	71
Table 7 Alternative EXAFS fitting results for Zn K-edge spectra of <i>M. californianus</i> byssal threads during tensile loading, relaxation and healing.....	91

LIST OF ABBREVIATIONS

AA	Amino Acid
AAA	Amino Acid Analysis
Asp	Aspartate
EDTA	Ethylenediaminetetraacetic acid
EXAFS	Extended X-Ray Absorption Fine Structure
Glu	Glutamate
His	Histidine
HRD	Histidine Rich Domain
ICP-OES	Inductively Coupled Plasma - Optical Emission Spectrometry
L-DOPA	L-3,4-dihydroxyphenylalanine
Phe	Phenylalanine
preCol	prepepsinized Collagenous proteins
preCol-D	Distal prepepsinized Collagenous protein
preCol-NG	Non-Gradient prepepsinized Collagenous protein
SAXS	Small-Angle X-ray Scattering
SEM	Scanning Electron Microscopy
SPM	Scanning Probe Microscopy
TEM	Transmission Electron Microscopy
TERS	Tip-Enhanced Raman Spectroscopy
TMP	Thread Matrix Protein
Tyr	Tyrosine
WAXD	Wide-Angle X-ray Diffraction
XAFS	X-Ray Absorption Fine Structure
XANES	X-Ray Absorption Near Edge Structure
XAS	X-Ray Absorption Spectroscopy
XRF	X-Ray Fluorescence

1 INTRODUCTION

Biological materials such as silk and nacre have fascinated humans since recorded history; however, in the last decades there has been a strong research effort to better understand the structure-function relationships which define them. A major driving force for this work is the hope of biomimetic and bio-inspired materials that integrate useful design principles from natural materials for improved performance, as well as green production processes [1].

Although biological materials are very diverse with respect to their material properties, only a limited selection of building blocks is available to organisms for their construction. The most common building blocks available to organisms are biologically synthesized components such as lipids, sugars, and proteins and inorganic components, such as mineral phases and inorganic ions. In spite of the limitations on building blocks used to construct the materials, these different components can be combined in many ways with different structures and hierarchies to achieve a quite broad range of mechanical performance [2–4]. A good example for this effect is the mother-of-pearl or nacre, found in the shells of certain mollusks. It consists of hard and brittle mineral platelets which are embedded in a softer and resilient protein matrix. Each of these components by itself would not have the desirable properties for a tough armor, which is supposed to protect the animals from a range of threatening scenarios. However, by combining both components in a specific hierarchically structured way, the resulting material can be hard, yet resistant to the inevitable formation of cracks in the mineral platelets.[5]

The example of nacre points to even more crucial aspects in the behavior of biological materials – namely, hierarchical structure and interfacial bonding. In other words, the material function of nacre depends largely on the spatial organization of the components. Additionally, the mineral platelets and proteins themselves possess specific nanoscale structures (e.g. the crystal lattice structure of the mineral phase and the folded conformation of the protein) that influence the properties of each respective building block. This seems to be a universal concept, and thus, structural and hierarchical organization of materials building blocks at multiple length scales is one of the main means of altering materials properties in nature [6]. The interface where the platelets connect to the matrix material is another vital point determining the mechanical properties of nacre. If the platelets were poorly connected to the matrix, their hardness and rigidity could not affect the mechanics of nacre in the same way [7]. In fact, the issue of interfacial properties and bonding is not only important in biomaterials – it is of utmost significance in the design of every composite material [8].

The main focus of this thesis work is the mussel byssus – a fibrous structure employed by mussels for the secure attachment to various substrates on the bottom and shore of the sea, which is composed almost entirely of proteins and a small amount of inorganic ions (Figure 1). Proteins are very diverse in terms of their functions. Enzymes and hormones, such as alcohol dehydrogenases and insulin, are probably the most commonly known group of

proteins; however, proteins are not limited to catalytic and signaling roles. In fact, there is a large group of proteins, including actins and collagens, which maintain the structural stability of the cellular cytoskeleton and the extracellular matrix [9,10]. Additionally, proteins are used to build extra-organismic materials such as silk [11–15], various marine egg cases [16,17] and as pertains to this thesis, the mussel byssus [18–20]. Frequently, proteins with physiologically relevant roles require the binding of co-factors to fulfill their functions. Such co-factors can be of proteinaceous or non-proteinaceous nature. The function of approximately one third of all proteins relies on metal ions such as Ca, Zn, Cu or Fe, as co-factors [21]. Thus, metal ions play crucial roles in the mechanisms of enzymatic catalysis, as well as signal transduction and gas transport [22]. For example, in insulin, a central pair of zinc ions binds six insulin monomers by formation of tetrahedral histidine (His)-zinc complexes. The structural changes within the monomers, induced by the binding of Zn, are thought to have consequences for the activity of insulin [23]. This example points to the tremendous influence, which metal based cross-links can have on the structure and stability of proteins.



Figure 1 Mussel of the species *Mytilus californianus* with attached byssal threads.

The example of Zn-binding in insulin demonstrates that small amounts of metal ions can have significant effects on the structure and stability of individual proteins, due to the special properties of metal coordination bonds. This is because metal coordination cross-links offer several advantages over other kinds of chemical bonds. For example, protein-metal coordination bonds such as His-Zn or L-3,4-dihydroxyphenylalanine (DOPA)-Fe possess near-covalent bond strengths [24], while providing faster reassociation rates [25]. For comparison, other non-covalent bonds (i.e. hydrogen bonding, etc.) would provide similar kinetic lability to metal coordination bonds, but at the cost of a much weaker bond. Thus, in

certain scenarios, the very special properties of metal coordination bonds can act as a means to satisfy the rather conflicting requirements of high strength and high lability.

The strategy of protein cross-linking by metal ions, however, is not restricted only to enzymes and hormones – it is also used in nature to assemble stable proteinaceous structures and materials on much larger scales and to enhance materials properties. Recent investigations, for example, have revealed insulin-like coordination of Zn via histidine and chlorine to be responsible for the hardening of the jaws of *Nereis virens*, a marine polychaete worm.[26–28] A similar cross-linking complex is proposed to be present in the hard tips of the fangs of the wandering spider *Cupiennius salei* [29] and in another marine worm, *Glycera sp.*, which utilizes Cu coordination rather than Zn. However, the hardening of proteinaceous materials by metal ion cross-linking is not limited to the use of histidine-based metal coordination complexes. In the thin outer cuticle of byssal threads, produced by the marine mussel genus *Mytilus*, DOPA – a post-translational modification of tyrosine - was found to form complexes with Fe ions to produce a hardened protective layer.[30–32] While the role of cross-linking by metal ions in hardening proteinaceous materials has become evident by the above mentioned investigations, the combination of high strength and high lability of metal-complex cross-links was recently proposed to play an important role in the self-healing capability of *Mytilus* byssal threads where they act as so-called reversible sacrificial bonds [33,34]. However, direct evidence for this involvement remains to be substantiated *in situ*.

Based on initial studies of the role of metal coordination in the byssus, several research groups have developed mussel-inspired metallopolymers with the intention of mimicking desirable properties of byssal threads (e.g. self-healing, underwater adhesion) [35,25,36]. While these initial studies are showing great promise, they do not adequately replicate the behaviors of the natural materials, likely due to an incomplete understanding of the defining biological structure-function relationships. The aim of this thesis is to improve this understanding by generating a more complete view of the specific roles of metal ions. In order to achieve a full understanding of these roles, it is essential to consider the byssus in the context of the environment in which it is adapted to function. Different *Mytilus* species have evolved to occupy a variety of habitats, varying in the amount of mechanical loading and the supply of trace elements. Since mussels are broadcast spawners, they cannot actively choose their habitat. The reliable function of their holdfast structure in a variety of environments is therefore vital to these organisms. Previously, much research was focused on the suitability of byssal threads as indicator for metal pollution in the sea.[37–42] Interestingly these investigations showed large variations in the metal content of byssal threads within the same species from different locations. As pointed out in the last paragraph, the hardening of the protective cuticle of *Mytilus* byssal threads, for example, relies on cross-linking via DOPA-Fe coordination. With this central role of metal-ions in the mechanics of the byssus cuticle, the question arises whether the observed varying concentrations of metals in the byssus affect the mechanical performance of the protective cuticle.

2 STATE OF THE ART

2.1 MYTILUS BYSSAL THREADS

2.1.1 Byssus Morphology and Function

The byssus is a holdfast structure produced by many marine bivalves, which functions to secure the organism during post-larval metamorphosis and, in some species, it is retained into the adult state [20]. The byssus of marine mussels is made almost entirely of protein with up to 1% metal ions by dry weight and consists of many threads, which are connected to the mussels' soft tissue on the proximal end via a structure called the stem (Figure 2A). An adhesive plaque on the distal end of each thread attaches the byssus to various substrates in the animals' marine habitats (Figure 2A). The plaque has been the subject of much research since it comprises a glue, which is able to provide secure attachment under wet conditions to various surfaces, including stone, wood, the shells of other mussels, and even man-made materials such as Teflon [43,44]. The portion of the byssus between the stem and the adhesive plaque is the actual byssal thread. The byssal thread is morphologically divided into a fibrous core and a protective cuticle (Figure 3) [45,46,32]. In the genus *Mytilus*, the byssal threads can be divided into two parts, namely the proximal region (close to the animal) and the distal region (close to the plaque), based on differing morphology, composition and most notably tensile mechanical behavior – the proximal region is soft and very extensible up to 200% strain [47], and the distal portion is much stiffer while remaining remarkably extensible up to strains of approximately 100% [48]. The primary focus of this dissertation work is on the fibrous core and cuticle of the distal region of the thread.

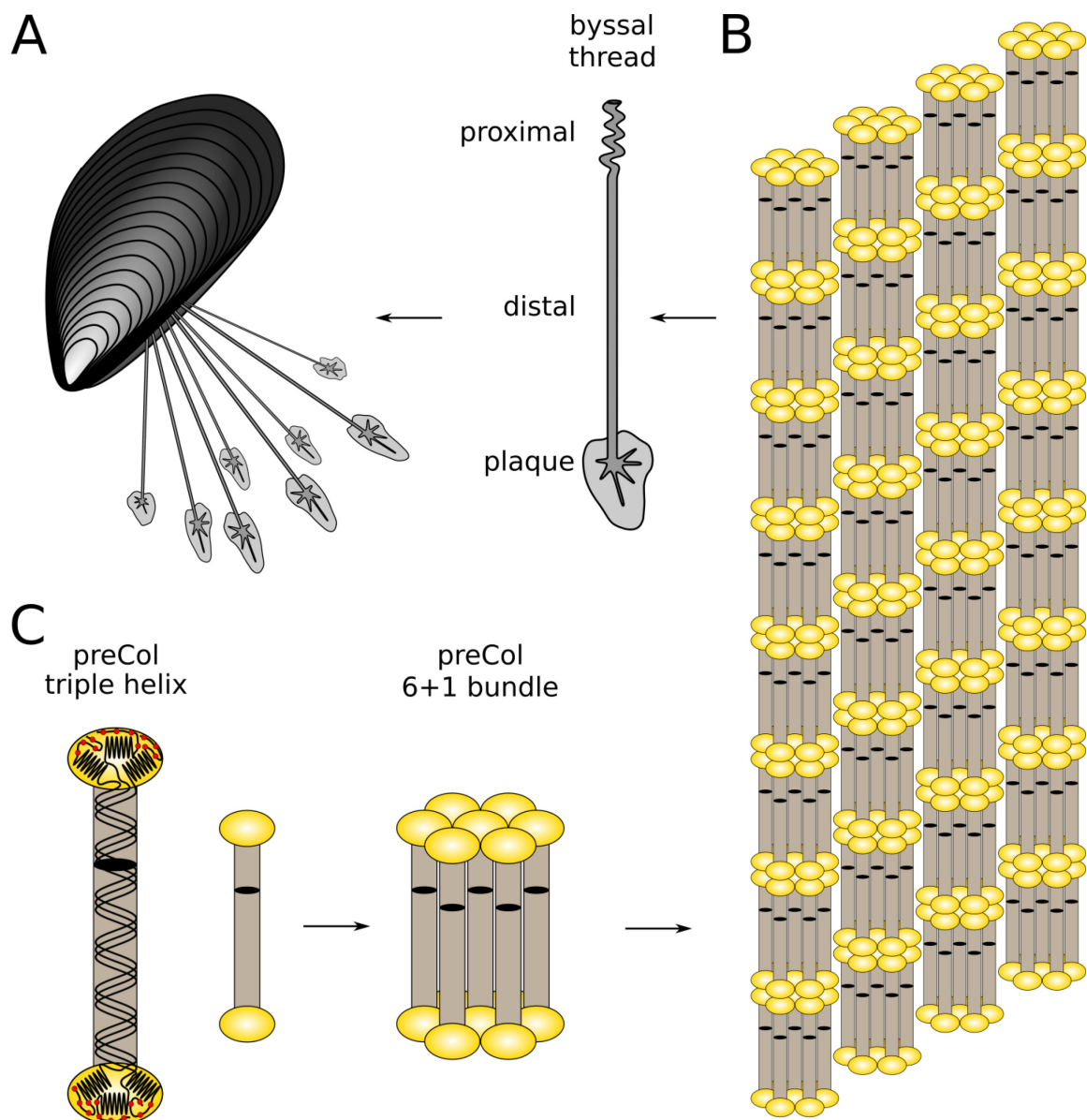


Figure 2 Schematic drawing of the *Mytilus* byssus (A), and the structural organization of preCols within the distal byssal thread (B, C). (C) Three preCols assemble into a triplet, forming a central collagenous triple helix with flanking domains and histidine rich domains (HRDs) on either end. The preCol triplets assemble into laterally aligned 6+1 bundles. (B) The 6+1 bundles are stacked end to end to form fibrils. These fibrils form fibrils in which they are axially staggered. (A) The preCol fibrils align along the threads long axis in the core of the distal thread portion. (modified from Krauss et al. [49])

2.1.2 The Core of Byssal Threads

The most striking property of the distal thread portion is arguably its ability to recover initial material properties following plastic deformation (i.e. self-healing). Figure 4 shows the typical mechanical behavior of the distal byssal thread portion under cyclic tensile loading. In the first cycle, threads show an initially stiff response, which is followed by a plateau region up to 40% strain of more or less constant stress following yield. A large hysteresis, dissipating up to 70% of the applied mechanical energy, is observed when relaxing the

thread after this first cycle of cyclic tensile loading. When stretched again immediately after this first cycle, threads display a tensile behavior with significantly reduced initial stiffness and no observable yield and plateau. However, if the threads are allowed to rest for some time (e.g. hours to days), a regeneration of mechanical performance towards the initial state is observed.[50] This self-healing capability is an impressive feature, considering that the threads lack any active cellular metabolism. Recent publications have suggested, that histidine-metal complexes in the fibrous thread core may be responsible for this behavior [33,34]; however, this will be discussed in more detail further on.

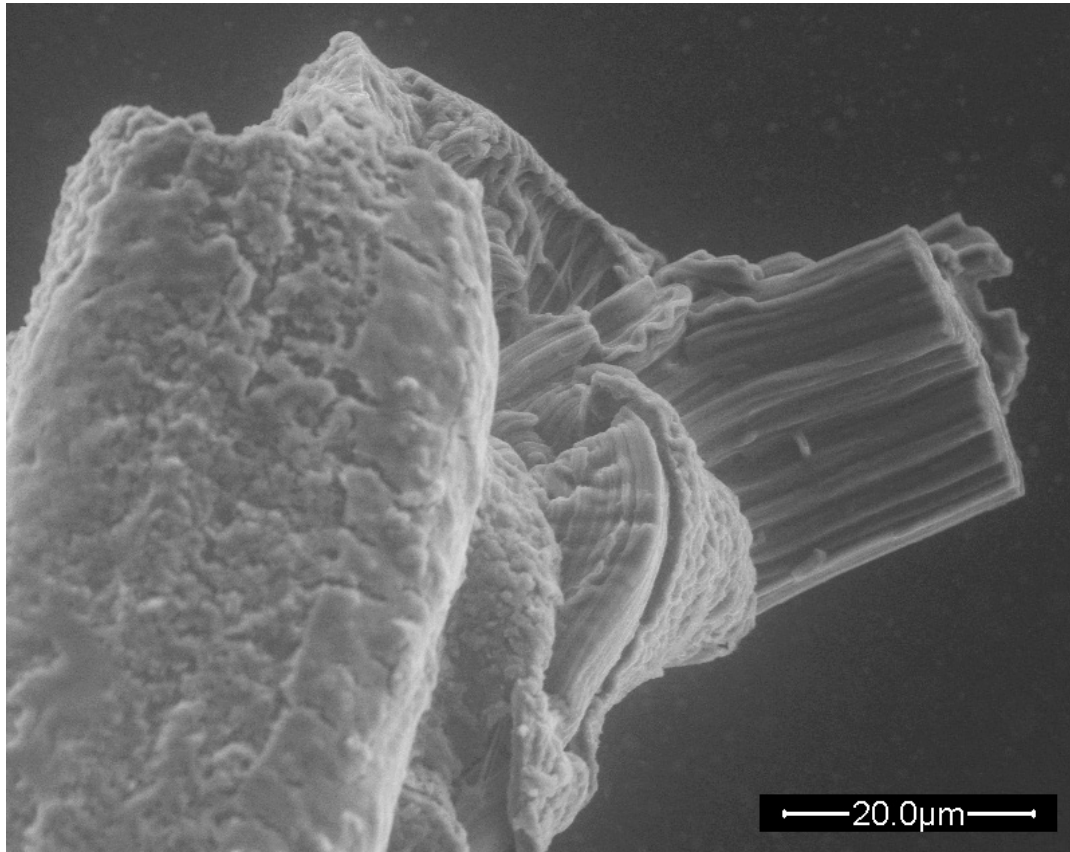


Figure 3 ESEM micrograph of a *M. galloprovincialis* byssal thread ruptured during tensile loading. The pulled-out fibers bundle from the core can clearly be distinguished from the granular structure of the cuticle.

The core of the distal thread region consists of protein fibers embedded in approximately 0.5 - 2% of dry mass of a matrix of proteins called TMP (thread matrix protein) (Figure 3) [51]. The fibers of the core are made of a group of proteins called preCols (prepepsinized Collagenous proteins) that comprise approximately 90% of the distal thread by dry weight (Figure 2B,C) [52]. In the distal part of the thread, the predominant forms of these proteins are preCol-NG (non-gradient) and preCol-D (distal). Both preCols consist of a central kinked collagen domain, which is surrounded by so-called flanking domains on both sides. Each end of each of these preCol variants is terminated at the N- and C-terminal ends by a histidine-rich domain (HRD) of 21 to 80 amino acids length which contains approximately 20 mol% of histidine. The two forms of preCols present in the distal core differ mainly in their flanking domains.[34] The flanking domain of preCol-NG is rich in the amino acid glycine, while the

same region of preCol-D possesses strong homology to alanine-rich silk-like β -sheet motifs.[34]

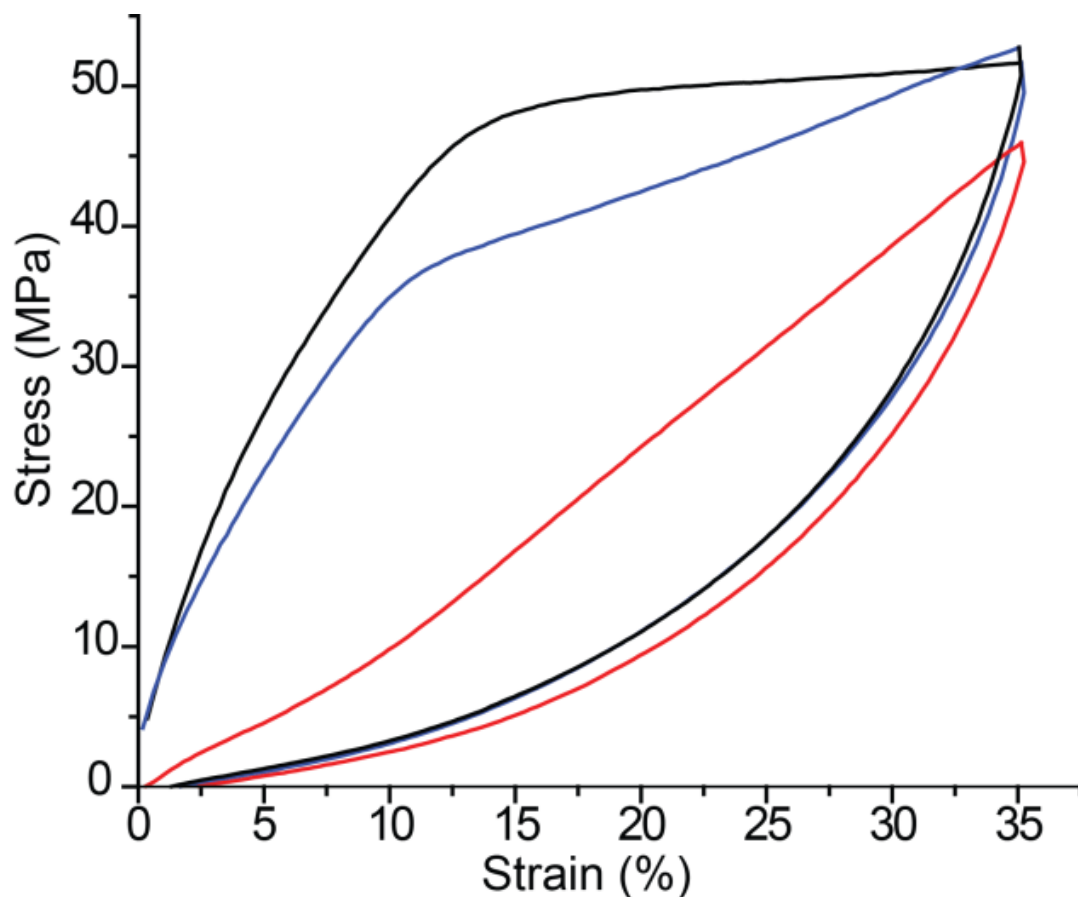


Figure 4 Stress vs. strain plot of cyclic tensile loading of the distal byssal thread portion of *M. californianus*. The first cycle (black line) shows the mechanical behavior of the native distal thread portion with an initially elastic response and a distinct plateau region after the yield point. When loaded a second time (red line) immediately after the first cycle, the material behaves less stiff, which is indicative of internal damaging resulting from the first loading cycle. However, when rested for one hour in distilled water, the threads are able to recover towards their initial mechanical performance (blue line). (modified from Harrington et al. [33])

The matrix of the core, in which the preCol fibers are embedded, is made of a group of proteins known collectively as TMP. Interestingly, non-enzymatic spontaneous deamidation of the TMP-1 variant has been shown to occur in byssal threads, resulting in the formation of significant amounts of (iso)aspartic acid over time periods of days.[51] This indicates a maturing process of TMP-1 and possibly a functional switch, after its co-secretion with the other thread components during thread formation [53]; however, the relevance of this to thread maturation or function is still unclear.

Due to the presence of the central collagen domain, the preCols have been demonstrated to form triple helices, which further assemble into hexagonal bundles of 6+1 (i.e. 7 triple helices or 21 individual preCol molecules) (Figure 2C) [54,49]. These 6+1 bundles connect end to end to form elongated fibrils, which are staggered axially by approximately 13 nm to

form semi-crystalline fibers, as opposed to the 64 - 67 nm stagger of fibrillar type I collagen (Figure 2B) [49]. A wide angle x-ray diffraction (WAXD) study has shown that the collagen domains of the preCols in the distal thread portion are only stretched by approximately 2% at thread strains up to 60%, indicating that the majority of the observed thread strain arises from the unfolding of the flanking and histidine-rich domains [33]. In a small angle x-ray scattering (SAXS) study, these domains were confirmed to unfold during tensile loading and to refold quickly after the load is removed. However, the mechanical recovery (i.e. self-healing) takes place over much longer time scales, which has been suggested to be due to the slow reformation of strong sacrificial cross-links. It has been proposed based on these studies that the elastic framework of the core provides a means of bringing these sacrificial cross-link sites back together close enough so they can reform easier, aiding the 'mechanical healing' of the core material.[49]

Several candidates for sacrificial bonds in the distal core have been suggested in the literature. FT-IR measurements of threads during stretching suggest that the β -sheet rich flanking domains of preCol-D unfold during stretching.[55]; however, predicted fast reformation of intra-sheet β -strand hydrogen bonding [56–58] and the immediate recovery of the overall structure of the elastic preCol framework following removal of load [49] would argue against β -sheet refolding being solely responsible for thread healing. Alternatively, increasing evidence points to the possibility that histidine-metal coordination bonds may act as sacrificial cross-links in the byssus core [33,34]. The presence of highly conserved His residues in the HRDs of *Mytilus* species [34,59] and the elevated content of His-binding metal ions in the thread (e.g. Zn and Cu) [38] are highly suggestive of the presence of His-metal coordination, as first suggested by Waite [19]. This hypothesis is further supported by the observation that EDTA-, pH- and DEPC-treatments, aimed at the disruption of histidine-metal bonds result in perturbed mechanics and the absence of the healing ability [33,34,50]. Another recent study used soft-colloidal probe measurements to investigate the mechanical behavior of a peptide derived from the preCol HRD. The results highlight the strong reversible properties of the metal-mediated histidine cross-links, which further strengthens the argument for their possible role as a sacrificial bond in thread mechanics [60]. These data present compelling evidence for the presence and mechanical role of the metal-binding via the HRDs; however, direct evidence confirming this hypothesis is still lacking. A major focus of this thesis work is to further probe the contribution of His-metal coordination to thread mechanical function, which is addressed in chapter 4.

2.1.3 The Cuticle of Byssal Threads

Surrounding the fibrous distal byssal thread core is a hard and flexible outer cuticle of about 2 - 10 μm , which protects the core from the surrounding environment [46]. Interestingly, despite its higher hardness and stiffness, the cuticle of certain *Mytilus* species is able to tolerate the large extensions of the fibrous core (up to $\sim 100\%$ in *M. californianus*, for example) without catastrophic failure [46,32]. This has been suggested to be due to the peculiar structure of the cuticle. Figure 5 shows a cross-section of a *M. californianus* byssal thread cuticle. The cuticle morphology resembles a particle-reinforced composite – i.e. a

material in which spherical granules are embedded in a matrix. Under tensile loading the matrix was observed to deform significantly in *M. galloprovincialis*, while the embedded granules reacted much stiffer to the applied load. At very high strains, micro-cracking was observed in the matrix and proposed to function as a means of redistributing the damage, thus avoiding the formation of large cracks. Thus, it has been hypothesized that the softer matrix provides damage tolerance in tensile loading, while the supposedly harder granules protect the byssal threads from abrasion damage.[46]

Similar to the core, current evidence suggests that the cuticle is composed almost entirely of protein and a small proportion of metal ions, primarily Fe [53]. The cuticle has been suggested to possibly contain lipids [61], but up to now there is no clear experimental evidence supporting this claim. Currently, the only identified protein building-block of the cuticle is MFP-1 (mussel foot protein-1). In contrast to the highly structured preCols of the core, MFP-1 has been reported to lack well-defined structure [62]; however, recent evidence from circular dichroism (CD) spectroscopy shows a notable degree of polyproline II (PPII) structure in MFP-1 under certain conditions [63]. Perhaps the most notable feature of MFP-1 is that many of the tyrosine residues of this protein are post-translationally modified to DOPA. The content of DOPA in native MFP-1 is about 10 to 15 mol%. Interestingly, two populations of MFP-1 were identified, differing only in the degree of post-translational modification of tyrosine to DOPA.[53]

The interaction of DOPA with metal ions or metal oxide surfaces has been shown to result in strong, but reversible cross-links in a previous study. Lee et al. showed with AFM based experiments that DOPA is critical to adhesion, whereas tyrosine showed no interaction, and that the binding mechanism is not hydrogen bond formation. The same investigation found the metal-DOPA based cross-linking to be of surprisingly high strength yet fully reversible.[24] The specific localization of iron in the cuticle and the presence of high DOPA content, led researchers to hypothesize the presence of DOPA-Fe complexation within the cuticle [64]. Confocal Raman spectroscopic imaging of the cuticle confirmed the presence of DOPA-Fe cross-linking in the cuticle and further demonstrated that the granules contained a higher DOPA-metal cross-link density than the matrix [30]. The removal of metals with EDTA removed the DOPA-metal resonance Raman signal and resulted in the reduction of thread hardness by approximately 50% [31]. Collectively, these results led to the current model of cuticle structure–function relationship and the role of metal ions. This model assigns the abrasion resistance and hardness of the cuticle granules to be due to a higher degree of cross-linking. The lower degree of metal-DOPA based cross-linking of the cuticle matrix enables the material to follow the large extensions of the core. The reversibility of the metal-DOPA cross-links has also been suggested to possibly enable self-healing of cuticle micro-cracks formed during extensive tensile deformation of byssal threads [46].

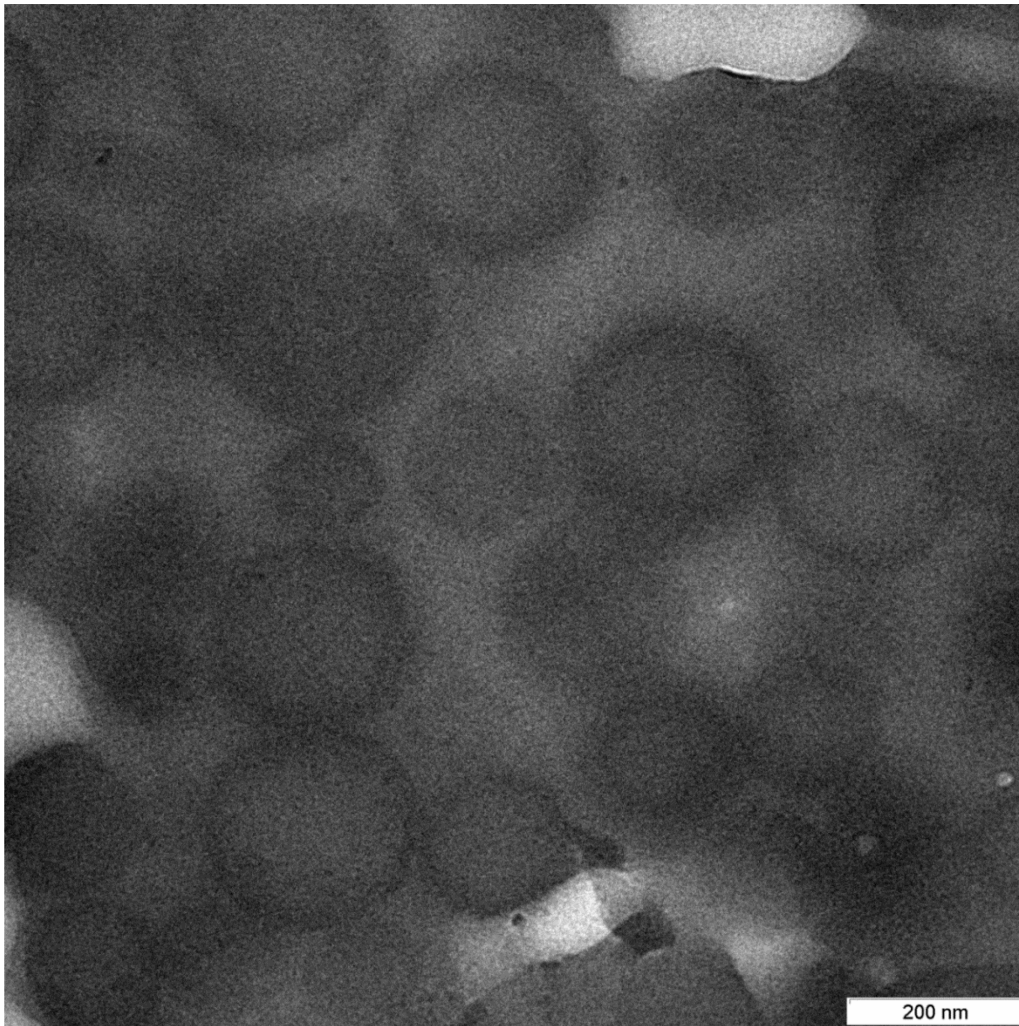


Figure 5 TEM micrograph of a transverse cross section of a *M. californianus* byssal thread cuticle. The denser granules can clearly be distinguished from the surrounding matrix.

2.1.4 The Byssal Thread Formation Process

Bearing in mind the rich morphological and ultra-structural features of the byssal thread core and cuticle, the formation process employed for their production appears to be rather coarse. The byssal threads are produced one by one in the ventral groove along the mussel's foot, by a process resembling injection molding [65,66]. The main protein building-blocks of the thread core, the preCols, are produced and stored in the secretory vesicles of specialized glands, along the foot groove [65,66]. Within the vesicles the preCols are stored at a pH of approximately 4 and form organized liquid crystal phases [67,66]. When a thread is formed, the content of the secretory vesicles is secreted into the foot groove and eventually the newly assembled thread is released into the seawater environment. The pre-production and storage of the thread materials allows relatively short thread production times of several minutes, enabling the mussels to quickly attach new threads when necessary. During this secretion process the proteins undergo a pH change up to about pH 8. At low pH values, both nitrogen atoms of the histidine ring are protonated, while at higher pH values ($pK_a \approx 6.6$) one of the nitrogen atoms is deprotonated [34], allowing it to bind to metal ions. It is

thought that the pH step during the secretion process induces metal-mediated cross-linking of the threads protein building blocks, essentially acting as a pH-trigger for self-assembly [34,19]. In fact, this pH dependent production method was successfully applied *in vitro* to form fibers from extracted preCol solutions [68].

It has been proposed that after the formation of the fibrous core, the vesicles containing the cuticle protein MFP-1 are secreted [18]. A similar pH-induced mechanism was proposed for the cross-linking of MFP-1, and a system of DOPA-Fe complexes has been shown to act as cross-link for the hardening of the cuticle [46,31,32]. In fact, the suggested pH-induced cross-linking mechanism via DOPA-metal complexes was shown *in vitro* to enhance mechanics, when introduced into PEG-based hydrogels [25]. It has been hypothesized, that a heterogeneous distribution of the two MFP-1 species could be the basis for the observed structure of the cuticle – granules contain DOPA-rich MFP-1 whereas the matrix contains MFP-1 with a lower DOPA content [30]. The differences in the DOPA content of the granules and the matrix may result in a different degree of metal-DOPA cross-linking. This would explain the different intensities of metal-DOPA resonance bands of the granules and the matrix, previously observed in a Raman imaging study of the thread cuticle. Alternatively, the granular structure of the cuticle could be the result of a maturation process of MFP-1 within the secretory vesicles prior to thread secretion.[30] During this maturation process the proteins undergo a phase separation within the secretory vesicles, forming granules surrounded by a matrix.[69] However, the two possible explanations for the granular structure of the cuticle could be interconnected. The differential cross-linking of the two MFP-1 species could well be the basis for the observed phase separation within the secretory vesicles.[30]

One significant open question concerning thread formation is how the metal ions in the cuticle and core are incorporated. This may occur via passive diffusion of metal ions into the threads or through an active uptake by the mussel followed by co-secretion of metals during thread formation. Since mussels are sessile filter feeders in the adult phase, a lot of research effort has been dedicated into the investigation of the suitability of mussels (or parts of them) as markers for environmental pollution [37,38,70–72,39–42,73]. Radiolabeling of metal ions such as V, Fe and Ni has demonstrated that metal ions are ingested and pass through the soft tissue before being integrated into the byssus – suggesting an active process for the uptake of metal ions by mussels [70,74–76]. While Zn, Cu and Fe are known to dominate the transition metal content of byssal threads, numerous other metals can be integrated in the byssus, including V, Ni, Co, and even Ur, Pu and Pb [37,38,71]. As specified above, mussels heavily depend on the presence of metal ions to form load-bearing cross-links for the function of the byssus holdfast structure. Together with the observed variability of metals in the byssus, this raises questions about the effect of introducing other metals capable of binding to byssus metal coordination sites on the mechanical performance of the material. In other words, can the introduction or exchange of metal ions be “toxic” to the materials mechanical function? This is a second major focus of this thesis, which will be addressed in chapter 5.

2.1.5 Byssal Threads as a Model Material for the Study of Metal-Based Cross-Linking

In the last paragraphs, the molecular structure and the formation process of the two proteinaceous materials of the distal byssal threads (i.e. the core and cuticle) were described. Both situations require the pre-production of protein building blocks, which are cross-linked to form the highly structured fibrous core and the somewhat less structured cuticle. For both materials a cross-linking strategy via metal-protein complexes has been identified. The proposed histidine-metal cross-links in the core seem to act as reversible sacrificial bonds enabling the recovery from plastic deformation [34,50]. However, the example of *Nereis* jaws shows that the very same Zn-mediated cross-linking strategy via histidine can act to produce a hardened rigid material [27]. In the cuticle of byssal threads the DOPA-Fe cross-links are utilized to achieve both the hardening of the material and possibly self-healing of the cuticle matrix via the reformation of these sacrificial bonds [30]. The byssal threads of the *Mytilus* species, therefore, provide an ideal model material to study the versatile effects of cross-linking via protein-metal complexes on the mechanics of a proteinaceous material, which is the major focus of this thesis work.

2.1.6 Mussel-Inspired Polymers

The findings about the role of metal-based cross-linking in the mussel byssus have inspired several research groups to develop self-healing metallopolymers based on DOPA-metal and His-metal complexes [35,25,36]. The characterization of the obtained PEG-based hydrogels has shown that the metal-coordination-based gelation strongly depends on the pH, which is consistent with the findings about the byssal thread formation process. However, while these materials are certainly capable of self-healing, they exhibit a $10^5 - 10^7$ lower stiffness than observed in the byssal thread core or cuticle (comparing storage modulus G' of the gels and reduced elastic modulus E_r of the core and cuticle). [35,46,25,36] One of the possible reasons for this could be that the obtained materials lack the hierarchical structuring found in the byssal threads. Therefore, further investigations on the design principles in the core and cuticle have the potential to inspire the production of new and improved self-healing polymeric materials with enhanced mechanical properties.

2.2 THEORY OF APPLIED METHODS

2.2.1 X-Ray Absorption Spectroscopy

X-ray absorption spectroscopy (XAS) is a technique widely used to obtain information about the short range environment and chemical state of an elemental species in a sample. It is element specific and depends on the emission of electrons upon absorption of X-rays.

X-Ray Absorption and Relaxation Processes

Figure 6A shows the Bohr model of a calcium atom. In its center is the nucleus and around it are the electron shells. The closer an electron shell is to the nucleus the higher is its binding energy, i.e. the energy needed to remove the electron from the atom. The electrons in the outer orbitals are called valence electrons. These electrons take part in chemical bonds. The closely bound electrons of the inner orbitals are called core electrons.[77]

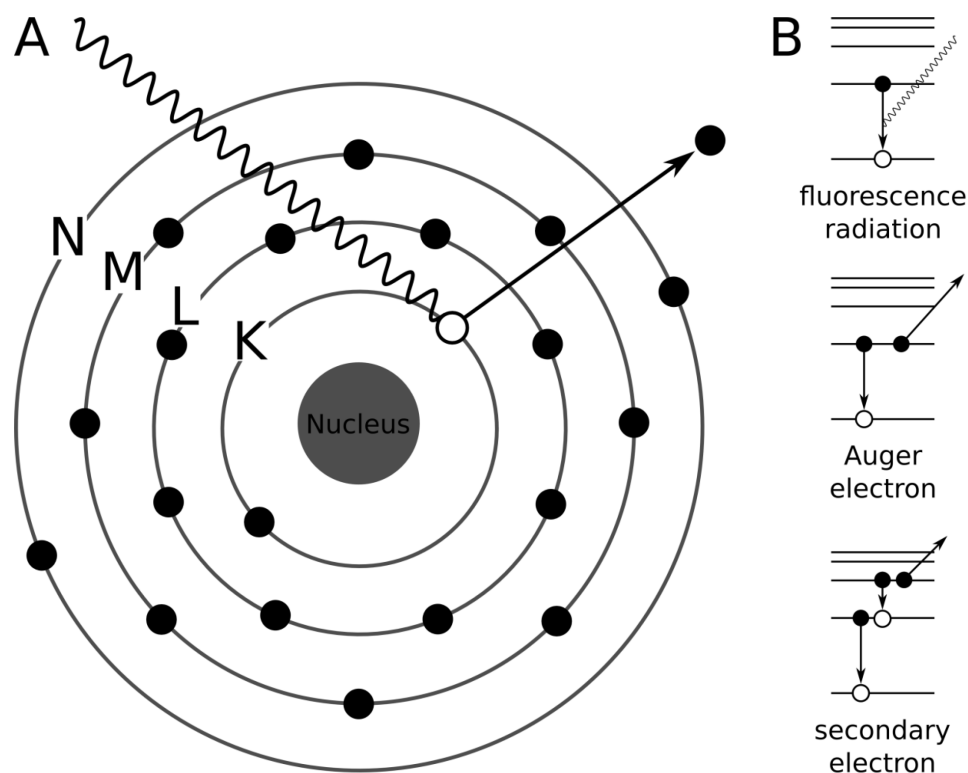


Figure 6 Summary of events taking place when x-rays are absorbed by an atom. (A) A Bohr model of a calcium atom showing the creation of a core hole, in the K-shell of the atom, by absorption of an X-ray. (B) The core hole is filled by the relaxation of electrons from shells with higher energy. The energy which is released during this relaxation can be emitted in the form of fluorescence radiation, emission of Auger electrons or the emission of secondary electrons. In the latter two cases the energy from one electron's relaxation is absorbed by another electron, which is then excited to a higher orbital or is emitted into the continuum. (modified from Kelly et al. and Teo [78,79])

When an incoming X-ray has enough energy to excite an electron to a higher unoccupied orbital or into the continuum (i.e. its binding energy), it is absorbed. If the X-ray energy is higher than the binding energy, the difference between X-ray energy and the electrons binding energy is equal to the kinetic energy of the emitted electron [78]. This process is called photoionization and as described above, it depends on the energy of the incident X-ray. The excited electrons are called photoelectrons. If the photoelectron was a core electron, the empty orbitals they leave are called core holes. The excited ionized state of an atom with a core hole is very unstable, and usually within femtoseconds the core hole is filled by relaxation of an electron from an energetically higher orbital. The relaxation of this electron causes the emission of energy.[78] Figure 6B summarizes the ways in which the energy can be emitted. It can be in form of fluorescence radiation, emission of Auger electrons or emission of secondary electrons [79]. In the case of Auger and secondary electron emission, the energy of the relaxation of one electron excites another electron, which is then emitted [77]. If the energy is emitted as fluorescence, the energy of the fluorescence radiation is the same as the energy difference between the electron's orbital of origin and the orbital with the core hole. Since the energies of the electron orbitals are distinct for every element, the energy of the fluorescence radiation is unique for each element [77,78].

The X-ray Absorption Coefficient and Absorption Edges

The intensity of X-rays transmitted I_t through a sample decreases exponentially with the samples thickness x and the X-ray absorption coefficient μ of the material [78].

$$I_t = I_0 e^{-x\mu} \quad (1)$$

The X-ray absorption coefficient μ is the probability of an X-ray being absorbed by a sample [78]. It depends on the atomic number Z and the atomic mass A of an element, and the density ρ of a material. Denser materials and higher- Z elements have a higher X-ray absorption coefficient. As described in the previous section the absorption of X-rays also depends on their energy E . [80] Thus, the X-ray absorption coefficient μ can be approximated as

$$\mu \propto \frac{\rho Z^4}{AE^2}. \quad (2)$$

If Equation (1) is solved for μx it is possible to determine the X-ray absorption coefficient by measurement of the X-rays incident intensity I_0 and the transmitted intensity I_t .

$$\mu(E)x = \ln \frac{I_0}{I_t}. \quad (3)$$

As explained above, X-ray fluorescence depends on the creation of core holes. The more X-rays are absorbed, the more core holes are produced and thus more X-ray fluorescence occurs. The X-ray absorption coefficient μ is therefore proportional to the intensity I_f of fluorescence lines

$$\mu(E)x \propto \frac{I_f}{I_0}. \quad (4)$$

The measurement of transmitted X-rays (I_t) and fluorescence X-rays (I_f) are the two most common detection methods used in XAS.

As mentioned above, the probability for an X-ray to be absorbed increases dramatically when its energy matches the binding energy of an electron in one of the atoms orbitals. These steps in the function of the X-ray absorption coefficient are called absorption edges.[78] An example of such an absorption edge is shown in Figure 7. The absorption edges are named after the shell that the photoelectron occupied in its unexcited ground state, so in the case of Figure 6A one would speak of the “Ca K-edge”. Like the fluorescence radiation following the absorption of an X-ray, the absorption edges are element specific and can be used to identify and quantify the elements present in a sample. By tuning the incident X-ray’s energy, it is possible to select the element to be monitored.

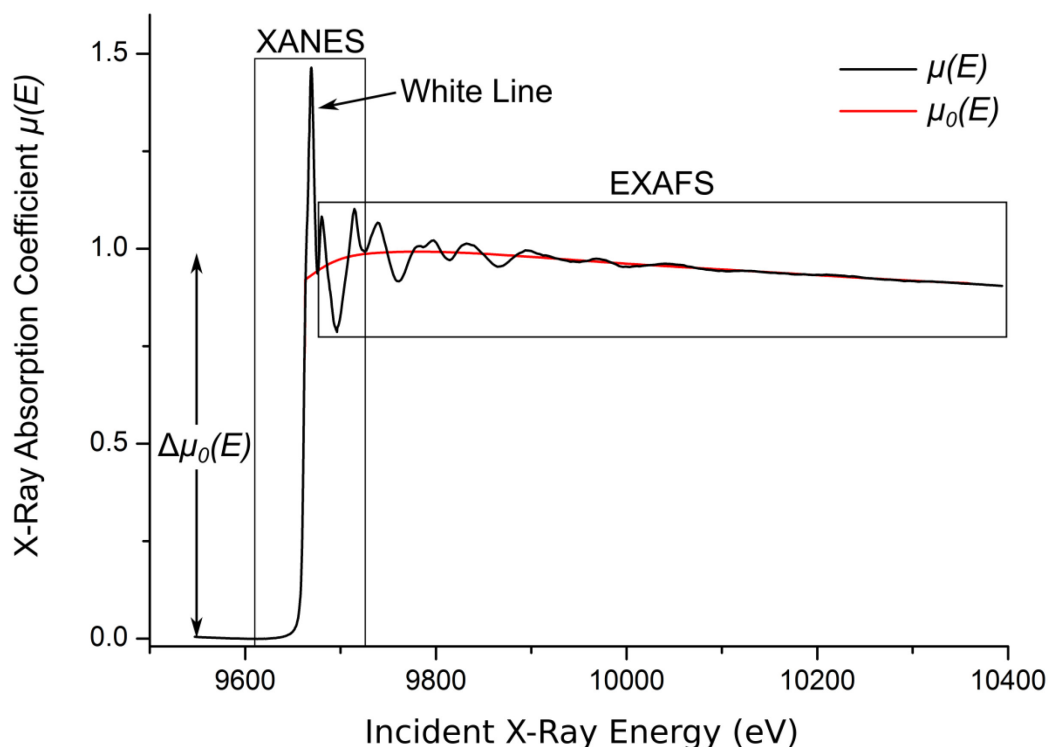


Figure 7 X-ray absorption spectrum of ZnO at the Zn K-edge. The black line shows the measured signal $\mu(E)$. The smooth red background function $\mu_0(E)$ describes the absorption of an isolated Zn atom. $\Delta\mu_0(E)$ is the edge step of the absorption coefficient. The white line, XANES and EXAFS region are marked.

X-Ray Absorption Fine Structure (XAFS)

Absorption spectra, like the one in Figure 7, are divided into two regions namely the X-Ray Absorption Near Edge Structure (XANES) and the Extended X-Ray Absorption Fine Structure (EXAFS). Each region contains information about different aspects of the environment of the absorbing elemental species. In the framework of scattering theory, the same basic physical

description applies to both regions. However, due to the influence of other physical effects, like resonances and electronic transitions to unoccupied energetic states, on the XANES, the current theoretical understanding allows a more quantitative analysis of the EXAFS than is possible for XANES [80]. Due to these circumstances and the comparative approach of the XANES analysis in this study, the following theoretical description of XANES spectra will be of a more qualitative nature than the description of EXAFS. An exhaustive theoretical description is given in the literature [78,79,81]. A very comprehensible introduction to the theory of EXAFS is given in [80]. The latter is the source for the following basic theoretical description of the source of XAFS.

From a quantum mechanics point of view, the absorption of X-rays and the subsequent excitation of a core level electron is a transition from an initial state (before the interaction of the X-ray and the electron) to a final state (with the created core hole and the photoelectron). Quantum mechanically these states can be described as wave functions of the core electron. These wave functions describe the probability for the electron to be at a certain point in space. With the picture drawn by this concept, $\mu(E)$ can be written as

$$\mu(E) \propto |\langle i|H|f\rangle|^2, \quad (5)$$

with the initial state $\langle i|$, the final state $|f\rangle$, and the interaction term H , leading from the initial to the final state. In the initial state, the core electron is tightly bound by the nucleus of the absorbing atom and the surrounding atoms have no effect on it. Thus, the wave function $\langle i|$ contains no information about the environment of the absorbing atom. This changes with the creation of the photoelectron. The photoelectron can interact with the neighboring atoms e.g. by scattering from them. Due to this interaction the electron wave function $|f\rangle$ now contains information about the neighboring atoms. As stated above, $|f\rangle$ is an electron wave function describing the probability distribution of the photoelectron in space. If just the point of origin of the photoelectron, i.e. its initial orbital around the absorbing atom, is observed, the function $|f\rangle$ describes the probability for the photoelectron to be where it was before the interaction with the X-ray, i.e. in the initial state $\langle i|$. Depending on the distance from the absorbing atom to the neighboring atoms, this probability is either adding to or subtracting from $\mu(E)$ (which was defined above as the probability of an X-ray being absorbed at the energy E). This is the source of the oscillations in XAFS.

The two regions of XAFS, XANES and EXAFS, are best distinguished by the variation of kinetic energy of the emitted photoelectrons. As the sample is irradiated by scanning the incident X-ray over an energy range, with higher X-ray energies an increasing amount of kinetic energy E_K is given to the photoelectron. E_K is the difference between the energy of the incident X-ray E , and binding energy of the electron E_0 (i.e. the absorption edge energy)[78].

$$E_K = E - E_0 \quad (6)$$

The kinetic energy of the emitted photoelectron influences the probability of it being scattered by the surrounding atoms. At the high kinetic energies of the EXAFS region this probability is so low that mostly single scattering paths are contributing to the signal. At the low kinetic energies of the XANES region, the contribution of multiple scattering paths is increasing.[81] This has consequences for the type of information contained in the signal of the two regions, which will be discussed in the following two sections.

The high probability of scattering at low kinetic energies of the photoelectron, and the low probability of interaction with surrounding atoms at high kinetic energies of the photoelectron, point to XAS being a very localized probe of the environment of the absorbing element. The short life time of the core hole, i.e. the time until the empty core orbital is filled by relaxation processes, also limits the range probed by XAS. However, it is important to emphasize, that even though XAS is probing only a limited range around the absorber, the extracted information still represents the average of all environments around the absorbing element, present in the total sample volume illuminated by the X-ray beam.

X-Ray Absorption Near Edge Structure (XANES)

The portion of XAFS spectra attributed to XANES depends on the observed element and also varies in literature, but generally the range from about -50 to +50 eV (from the edge energy) is considered in XANES analysis [78]. The energy at which the emitted photoelectron has a wavelength equal to the distance between the absorbing atom and its nearest neighbor, is frequently used to divide the two regions [82,81].

As mentioned in the last section, multiple scattering of the photoelectron dominates the XANES signal. It therefore contains information about the spatial arrangement and geometry of the atoms surrounding the absorbing atom [81]. The edge energy, the energy of the steepest increase in absorption [82], varies with the oxidation state of the absorbing atom, with a higher (positive) oxidation number shifting the edge position a few electronvolts to higher energies. This is due to the electrons, of an atom in a higher oxidation state, being more tightly bound, and thus, having a higher binding energy [78]. The opposite case applies to atoms with a lower (negative) oxidation number. Additionally, the availability of unoccupied electron orbitals, to which the photoelectron can be excited, influences the shape of the absorption edge. These influences show up in the XANES spectrum as decorations like isolated peaks, shoulders or so-called white lines.[78] A white line is a strong peak on top of the absorption edge like the one shown in Figure 7.

Since there are a lot of physical phenomena which influence the XANES, a full theoretical description has not yet been achieved. This makes the interpretation more complicated, and the use of well-chosen standards is of high importance in the analysis of XANES spectra.[82,81]

Extended X-Ray Absorption Fine Structure (EXAFS)

The EXAFS is usually observable in the region from just above the absorption edge up to about +1000 eV, depending on signal quality. With the increase in kinetic energy towards the

end of the EXAFS region, the scattering of the photoelectron by the surrounding atoms becomes more and more unlikely. This is the reason for the decay of the EXAFS oscillations in Figure 7. Above, the source of the XAFS was explained, and it was stated that the photoelectron in the final excited state influences the probability of X-ray absorption. An important deduction from this is that, in order to take part in the EXAFS, the photoelectron has to be scattered elastically from the surrounding atoms and return to its initial position before the core hole has been filled again by relaxation of the excited absorber atom. Compared to the XANES, the EXAFS is influenced by fewer physical phenomena. This, together with some approximations, enables a full theoretical description and allows a more quantitative interpretation of the EXAFS.[80] In particular, the EXAFS region provides information about the type and number of atoms surrounding an absorbing atom, as well as the interatomic distances and the degree of local molecular bonding disorder [78].

Figure 7 shows the X-ray absorption spectrum ($\mu(E)$) of ZnO at the Zn K-edge. The red line is the calculated absorption spectrum of an isolated Zn-atom ($\mu_0(E)$). After the absorption edge step $\Delta\mu_0(E)$ is subtracted from $\mu(E)$, the only differences in the two spectra are the oscillations of $\mu(E)$. As explained above, these oscillations arise from the superposition of the emitted photoelectron wave and the photoelectron wave backscattered from the atoms surrounding the absorbing Zn-atom and the absorbing Zn-atom itself. It is this part of the data which contains the information about the environment of the absorbing atom (in case of Figure 7, Zn). From the information above, the EXAFS function is defined as

$$\chi(E) = \frac{\mu(E) - \mu_0(E)}{\Delta\mu_0(E)}. \quad (7)$$

As we saw above, the EXAFS is best described in terms of the wave behavior of the photoelectron. Therefore, the X-ray energy is usually converted to the photoelectron wave number

$$k = \sqrt{\frac{2m(E - E_0)}{h^2}}, \quad (8)$$

with the photoelectron mass m , the X-ray energy E , the absorption edge energy E_0 and Planck's constant h . Each of the frequencies, which contribute to the oscillations in EXAFS, corresponds to the interaction of the photoelectron with different neighboring atoms. The scattering caused by one pair of absorbing and scattering atom is called a scattering path and the surrounding atoms at similar distance from the absorbing atom belong to one coordination shell.[80] The EXAFS equation is the sum of all scattering paths from each coordination shell

$$\chi(k) = \sum_j \frac{N_j f_j(k) e^{-2k^2 \sigma_j^2} e^{\frac{-2R_j}{\lambda(k)}}}{k R_j^2} \sin[2kR_j + \delta_j(k)], \quad (9)$$

with the number of neighboring atoms N at the distance R from the absorbing atom and σ^2 the disorder of R . For multiple scattering, R represents half the length of the full scattering path. The amplitude $f(k)$ and the phase-shift $\delta(k)$ are determined by the scattering properties of the neighboring atoms.[82] These scattering properties can be calculated by analysis software like FEFF provided in the Demeter XAS analysis package [83]. The mean free path $\lambda(k)$ of the photoelectron is the mean distance the photoelectron travels before it scatters inelastically and before the core hole is filled again. It is on the order of 5 to 30 Å and, together with the R^{-2} term, it limits the environment probed by XAFS to about 5 Å. By knowing the scattering amplitude $f(k)$ and the phase-shift $\delta(k)$ the EXAFS equation can be used to determine N , R and σ^2 of the surrounding atoms, within this range.[80]

The XAFS Measurement

XAFS requires a high intensity X-ray beam tunable over a large energy range. Therefore, usually a synchrotron is used as an X-ray source. The beam energy is selected by a tunable silicon monochromator. The monochromators used for XAFS have to provide a stable beam of high purity, with respect to higher harmonics, as well as a high energy resolution of about 1 eV or better. Frequently monochromator stabilization devices are used to overcome instabilities caused by the optical elements of the monochromator itself. The most common ways to detect the XAFS are the detection of the transmitted or the fluorescent X-rays. For transmission measurements the sample needs to be uniform in terms of X-ray transmission and of the right thickness. Usually thick samples or samples with low concentrations of the absorbing element require the detection of the fluorescence signal, but other factors like sample geometry and sample inhomogeneity also influence the choice of detection method.[80,82]

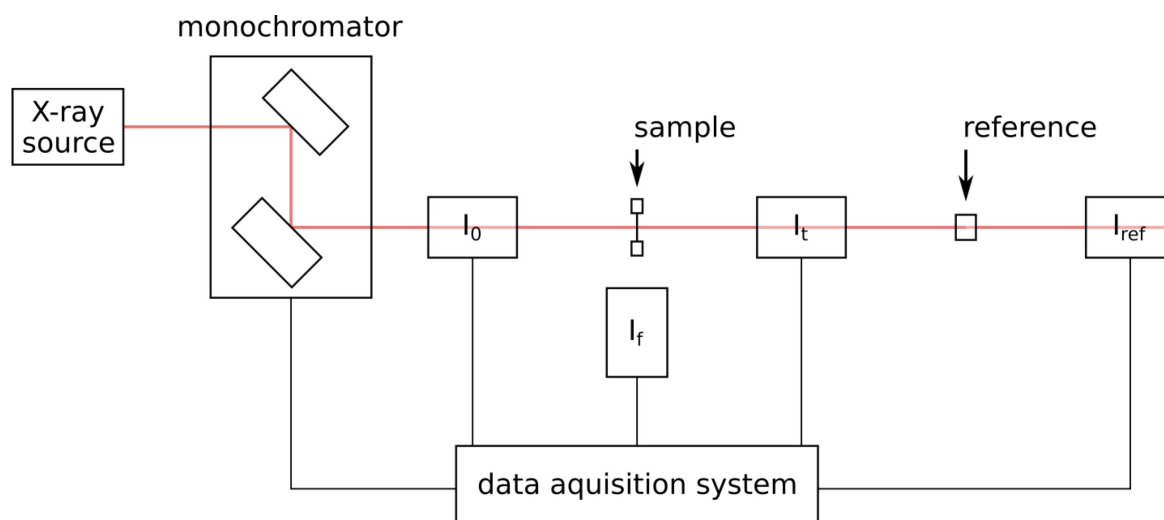


Figure 8 The standard XAS setup for measurements of samples in transmission (I_t) or fluorescence (I_f), and the simultaneous measurement of a standard reference in transmission (I_{ref}). The X-rays are tuned to a specific energy by the monochromator optics and the incident x-ray intensity is measured by an ion chamber (I_0). The sample signal can be measured either with an energy dispersive fluorescence detector (I_f) at 90° to the x-ray beam or in transmission by a second ion chamber (I_t) after the sample, in line with the x-ray beam. The reference standard is usually measured in transmission by either an ionization chamber or a photosensitive diode (I_{ref}).

The standard setup is shown in Figure 8. It consists of three detectors in line, to measure I_0 , I_t and I_{ref} , and a detector for the measurement of I_f at right angle to the incident beam. The sample is placed between I_0 and I_t and a standard sample is placed between I_t and I_{ref} . The measurement of standard samples is necessary for energy calibration, to identify structural features in the XANES and for the evaluation and constraint of EXAFS fitting parameters [82]. I_0 and I_t are ionization chambers and I_{ref} can either be measured by the same kind of detector or a photosensitive diode. The detectors for the fluorescence measurement are usually energy dispersive, which enables the selection of single fluorescent lines in multi-element samples.[82] For a fluorescence measurement, the detector is placed at 90° to the incident beam and the sample is oriented at 45° to the incident beam and the detector. This is done since the influence of elastic scatter is reduced at 90° due to the polarization of synchrotron radiation.[80] The time needed for a fluorescence measurement is mainly determined by the counting time the detector needs to count enough photons of the fluorescence of the studied element in order to obtain a suitable signal to noise ratio. Another aspect, of fluorescence detectors, to consider is the saturation of it by an overload of the signal. This happens when the detectors count rate too low to count all the incoming photons and results in the so-called dead time of the detector. If this dead time is too high it can significantly distort the XAFS signal.[82]

Generally, XAFS can be applied to a wide range of samples, since it probes only a small volume around the selected element and is very flexible in terms of the sample environment [82]. Usually little to no sample preparation is necessary. However, especially for biological

samples, a reasonable amount of consideration has to be given to the issue of radiation damage. The long measurements at high beam intensities can result for example in photo-reduction and -oxidation, and the formation of free radicals in organic and hydrated materials. While radiation damage cannot be prevented, precautions like measuring at low temperatures or scanning along the sample may reduce the effect on the measurement.[82] The careful inspection of several subsequent scans of the same sample can be used to evaluate the occurrence of radiation damage. Another issue with the measurement of XAFS can be the occurrence of self-absorption. For standards, which usually contain high concentrations of the absorbing element, it is sometimes necessary to measure finely ground powders or thin films with grain sizes or thicknesses below the calculated absorption length of the material (or thin films etc), in order to prevent influences of self-absorption. Many biological materials, however, contain only very low concentrations of inorganic absorbers in an organic matrix of lighter elements, so self-absorption for this kind of sample is usually not an issue.

Data Analysis

A more elaborate overview of data analysis can be found in the literature [78,82]. Here, only the most important aspects for the analysis involved in this study will be considered. All described steps are drawn from the above mentioned literature.

Before the XAFS data can be analyzed and interpreted, a considerable amount of pre-processing is necessary. The spectra need to be cleaned from instrumental noise and over-sampling, and the data range for analysis is determined. Before all scans of a sample can be averaged, the energies of all scans have to be aligned to a reference standard. After merging all scans, the EXAFS function $\chi(E)$ can be extracted from the measured spectrum $\mu(E)$. From Equation (7) we can see that this involves the subtraction of a background function $\mu_0(E)$, describing the absorption of an isolated atom, and the normalization to the edge step $\Delta\mu_0(E)$. Additionally a smooth pre-edge function is subtracted to remove the absorption from other edges and any instrumental noise. The data in Figure 7 has already been treated in this way. Now the value of the absorption edge energy E_0 can be determined by the global maximum of the first derivative of the spectrum.

The next step is to convert the data to a function of k using the description of EXAFS from Equation (9). Since also in k -space the EXAFS oscillations are damped for higher values of k , the data is commonly multiplied by k to the power of 2 – 3. Using a Fourier transform, it is now possible to extract the frequencies the EXAFS oscillations consist of, and transfer them into r -space. However, the peak positions in r -space do not correspond directly to the bond lengths since there is still a phase shift and other factors involved.

In order to obtain the bond lengths and other information about the environment of the absorbing element, a model for the extracted data in r -space has to be built and fitting analysis has to be applied. Usually, techniques other than XAS are applied to gain some initial knowledge about the material in question. In the case of proteins one can then browse the protein data base (PDB) as a source for crystal structures of proteins which have

similar components. The next step is to generate scattering paths from PDB data. This involves the calculation of the parameters describing the scattering properties ($f_j(k)$, $\delta_j(k)$ and $\lambda(k)$) and distances (R_j) of the atoms thought to surround the absorbing element. The scattering paths are used to assemble a model to describe the experimental data. The theoretical model is then evaluated by fitting the EXAFS equation from the model to the experimental data. For this evaluation of the EXAFS model, two parameters are added to the EXAFS function in Equation (9), to obtain

$$\chi(k) = \sum_j \frac{S_0^2 N_j f_j(k) e^{-2k^2 \sigma_j^2} e^{\frac{-2R_j}{\lambda(k)}}}{k(\Delta r + R_{eff,j})^2} \sin[2k(\Delta r + R_j + \delta_j(k))] \quad (10)$$

S_0^2 is the amplitude reduction factor, accounting for amplitude reductions due intra-atomic processes of the absorber atom. It is determined by the measurement of a standard at the same conditions as the sample measurement. S_0^2 only depends on the elemental species of the absorber atom and is the same for each scattering path included. The absorber-scatterer distance R_j is now defined as $\Delta r + R_{eff,j}$. $R_{eff,j}$ is the calculated absorber-scatterer distance determined from the PDB data and Δr is the change of this distance determined by fitting of the model to the measurement data. For each scattering path j , selected from the PDB data, $f_j(k)$, $\delta_j(k)$ and $(R_{eff,j})$ are calculated. N_j , Δr , σ_j^2 and ΔE_0 are parameters determined during the fit of the model to the data. N_j is the degeneracy of a path (i.e. the number of times this path occurs). σ_j^2 is the mean square variation of the absorber-scatterer distance R_j . It describes the thermal and structural disorder of the atoms involved in this path. ΔE_0 is a small edge energy shift, which allows the alignment of the theoretical model to the measured data.

As with every measurement technique, the analysis of EXAFS also has its limitations. For example, it is important to note that there is a maximum for the number of fitting parameters, which can be used in a fit of a certain data range. This is determined by the number of independent points (degrees of freedom) of the measurement data within the range by $N_{max} = \pi \Delta R \Delta$. Also, the fitting parameters form two groups, namely the ones which add to the amplitude of the EXAFS spectrum (S_0^2 , N_j and σ_j^2) and the ones which determine the phase (ΔE_0 and R_j). Especially within these groups there is considerable correlation between the fitting parameters. Resulting from this, the maximum accuracy of the determined coordination number and the bond lengths is estimated to be about 10% and 1%, respectively.[82] A further limitation of the technique concerns the differentiation between scattering paths of atoms with similar atomic weights at similar distances from the central absorbing atom. Since the scattering properties of these atoms are very similar, they are virtually indistinguishable from each other by means of EXAFS analysis.

2.2.2 Raman Spectroscopy

Raman spectroscopy is a technique widely used to observe modes of vibration and rotation in molecules. It exploits the phenomenon of inelastic scattering of photons during the interaction of light with matter. It enables one to identify the characteristics of chemical bonds and furthermore can provide information about the orientation and conformation of molecules in a sample.

The Frequency of Light and the Energy Levels of Molecules

According to quantum mechanics, a bound particle can only occupy discrete energy levels. This model of quantized energy levels can be applied to electrons in the electronic cloud around an atomic nucleus, but it also applies to the energy of larger molecules. In this case, the energy levels refer to the vibrational, rotational and translational modes possible in a molecule. Each of these modes occupies a discrete energy level. In order to transfer from one of these levels to another, the molecule needs to absorb or emit a quantum of energy.

The quantum of light is called a photon, and its energy can be described by a linear correlation to its frequency

$$E = h\nu \quad (11)$$

with the energy E , the frequency ν and a linear factor h known as Planck's constant. If Equation (11) is applied to the difference between two energy levels of a molecule we get

$$\Delta E = E_n - E_m = h\nu = \frac{hc}{\lambda} \quad (12)$$

with E_n and E_m the energies of the excited and initial state of the molecule, c the speed of light and λ its wavelength. In other words, the energy needed to promote the molecule from its initial energy state to the excited state can be written in terms of the frequency or wavelength of the electromagnetic radiation. With this, it is possible to calculate the frequency that an incoming photon needs to possess in order to promote the molecule to the higher energy level. In the case of molecular vibrations and rotations, this frequency corresponds to the infrared range of electromagnetic spectrum.

Interaction of Light and Matter

When light interacts with matter, its photons may either be absorbed or scattered (Figure 9). If the energy of the incoming photon has the energy needed to promote the molecule from its ground energy state to a higher vibrational energy state, it is absorbed and the molecule now occupies the corresponding higher vibrational state. This is the base of infra-red (IR) absorption spectroscopy, where a broad range of IR radiation is sent through the sample and the transmitted radiation spectrum is collected and analyzed.

However, as stated above, it is also possible for the incoming photon to be scattered from the molecule. The incoming photon, in this case, has an energy that does not match any of the energy differences between the discrete vibrational energy states of the molecule. The

molecule is, thus, not excited to a higher state of vibrational energy, but rather the electron cloud around the atomic nuclei of the molecule is distorted (polarized), resulting in a virtual energy state of the molecule. The incoming and the emitted photon can have the same energy (elastic or Rayleigh scattering) or slightly differ in energy (inelastic or Stokes scattering). The inelastic scattering constitutes what is known as the Raman scattering. While the majority of scattered photons undergo Rayleigh scattering, only one in every 10^6 - 10^8 photons is inelastically scattered, which means that the Raman signal only has about 10^{-5} of the incident beam intensity [84,85]. The weakness of the inelastically scattered light was one of the main reasons why Raman spectroscopy was marginally used in materials characterization before lasers, intense monochromatic light sources, had been discovered. As pictured in Figure 9 anti-Stokes scattering requires molecules to be in an excited vibrational state, but the Maxwell-Boltzmann distribution law states that (at room temperature) most molecules will be in the vibrational ground state. Therefore, Stokes scattering makes up for most of the Raman signal (at room temperature). In either case of inelastic scattering, the energy difference of the incoming and emitted photon results in a frequency shift of the emitted light compared to the incoming light. It is this frequency shift (also called Raman shift) that Raman spectroscopy detects (Figure 9).

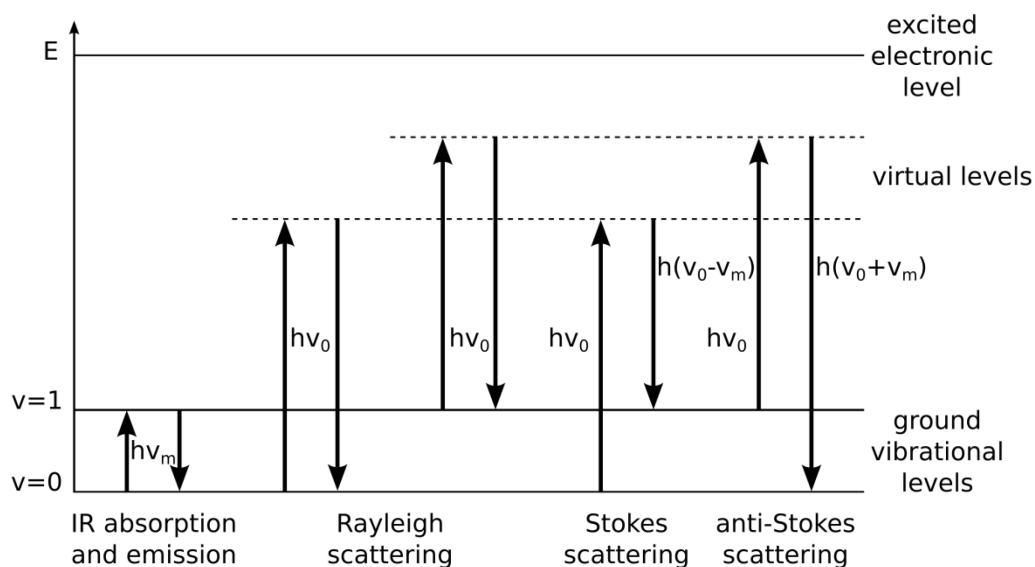


Figure 9 Diagram of transitions between vibrational energy levels corresponding to the process of IR absorption/emission, Rayleigh and Raman scattering. (modified from Chalmers and Griffith [86])

The Frequency of Molecular Vibrations

From Figure 9, we can see that the energy difference between the incoming and emitted photon in Raman scattering matches the energy difference between two vibrational states of the molecule. In the previous section, it was observed that this energy difference is connected to the frequency shift of the incoming to the emitted light. However, the energy of the molecule is also connected to the frequency of vibration of the molecule.

The vibration of a diatomic molecule can be described by a model of two masses connected by a spring representing the chemical bond between the molecules atoms. The displacement q of the two particles can be described by

$$q = q_0 \cos 2\pi\nu_m t \quad (13)$$

with q_0 the maximum displacement and ν_m the frequency of the vibration given by

$$\nu_m = \frac{1}{2\pi} \sqrt{\frac{K}{\mu}}. \quad (14)$$

Here K is the force constant of the spring representing the strength of the chemical bond and μ the reduced mass of the system, with $\mu = \frac{m_1 m_2}{m_1 + m_2}$. [84] Since the energy difference ΔE between two vibrational states of the molecule can be measured as explained in the last section, the frequency ν_m of the molecular vibration can now be calculated by Equation (11). Equation (14) shows that the frequency ν_m of the vibrating system will be higher for light atoms connected by strong bonds and lower for heavy atoms with weak bonds. From this theoretical understanding, it is possible to assign certain Raman shifts to specific vibrational levels of molecules.

The next section will give a theoretical explanation of how the excitation light interacts with these molecular vibrations to give rise to the Raman signal.

The Origin of Raman Spectra According to Classical Theory

The incoming light from the laser source can be described as an electromagnetic wave. Since the magnetic component of this wave is not involved in the scattering, it is sufficient to consider only the electric field strength E of the incident light. It oscillates with time t and can be described by

$$E = E_0 \cos 2\pi\nu_0 t \quad (15)$$

with E_0 the vibrational amplitude and ν_0 the frequency of the incident laser light. The electric dipole moment P of a diatomic molecule irradiated by light is

$$P = \alpha E = \alpha E_0 \cos 2\pi\nu_0 t \quad (16)$$

with a proportionality constant α called the polarizability of the vibration. The nuclear displacement q of the molecule vibrating at a frequency ν_m is stated in Equation (13). For small vibrational amplitudes $\alpha \propto q$, so α can be stated as a linear function of q ,

$$\alpha = \alpha_0 + \left(\frac{\partial\alpha}{\partial q}\right)_0 q + \dots \quad (17)$$

with α_0 the polarizability at the equilibrium position and $\left(\frac{\partial\alpha}{\partial q}\right)_0$ the rate of change of α with respect to the rate of change of q , at the equilibrium position. By combination of Equations (13), (16) and (17) we obtain

$$\begin{aligned} P &= \alpha_0 E_0 \cos 2\pi\nu_0 t + \left(\frac{\partial\alpha}{\partial q}\right)_0 q E_0 \cos 2\pi\nu_0 t \\ &= \alpha_0 E_0 \cos 2\pi\nu_0 t + \left(\frac{\partial\alpha}{\partial q}\right)_0 q_0 E_0 \cos 2\pi\nu_0 t \cos 2\pi\nu_m t . \end{aligned}$$

And with $\cos x \cos y = \frac{\cos(x+y) + \cos(x-y)}{2}$ we can write

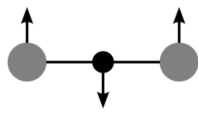
$$\begin{aligned} P &= \alpha_0 E_0 \cos 2\pi\nu_0 t \\ &\quad + \frac{1}{2} \left(\frac{\partial\alpha}{\partial q}\right)_0 q_0 E_0 [\cos\{2\pi(\nu_0 + \nu_m) t\} + \cos\{2\pi(\nu_0 - \nu_m) t\}] \end{aligned} \tag{18}$$

with the first term describing the Rayleigh scattered light with the frequency ν_0 and the second term corresponding to Raman scattered light with frequency $\nu_0 + \nu_m$ (anti-Stokes) and $\nu_0 - \nu_m$ (Stokes) (also see Figure 9). As Equation (18) shows, there is no Raman scattering term if the rate of change of polarizability $\left(\frac{\partial\alpha}{\partial q}\right)_0$ is zero. In other words, Raman-activity of a vibration depends on a change in its polarizability.[84]

Types of Molecular Vibrations and Their Raman Activity

In a non-linear molecule with N atoms, there are $3N - 6$ vibrational degrees of freedom and for linear molecules, there are $3N - 5$ [85]. For a triatomic molecule, these degrees of freedom (vibrational modes) are symmetric- and asymmetric stretching and bending or deformation of the bonds. Table 1 shows the three modes of vibration for a linear triatomic molecule and their corresponding activities in IR and Raman spectroscopy. Since the symmetric stretching mode of this molecule produces large changes in polarizability, it gives strong Raman scattering and low IR absorption (which relies on changes in dipole moment). On the other hand, the asymmetric stretching and the bending mode have almost no polarization change, but rather a high change in dipole moment. They therefore produce strong IR signal, but the Raman signal is almost non-existent.[86]

Table 1 Factors determining the IR and Raman activity of vibrations for a linear triatomic molecule. (modified from Chalmers and Griffith [86])

	symmetric stretch	asymmetric stretch	bending deformation
normal mode of vibration			
dipole moment	0		
IR activity	-	+	+
polarizability ellipsoid			
Raman activity	+	-	-

Polarization Dependence of Raman Scattering

In addition to chemical information about a sample, Raman scattering can also provide information about the orientation of molecules. This is done by exploiting the polarization dependence of Raman scattering.

As described above, Raman scattering depends on the polarizability α of the electron cloud of a bond by the excitation light. The dipole moment of a molecule, irradiated by light, is given in Equation (16). The polarizability of the electron cloud depends on the polarization of the incoming light. Linearly polarized light affects the electron cloud of the molecule in all possible polarization planes. The intensity of the interaction, however, depends on the relative orientation of the electron cloud and incoming light [85]. To describe this, the simple expression in Equation (16) needs to be expanded to account for the dipole change along the x-, y- and z-axis of space. The dipole change along the x-axis is

$$P_x = \alpha_{xx}E_x + \alpha_{xy}E_y + \alpha_{xz}E_z \quad (19)$$

with the first subscript referring to the direction of polarizability of the molecule, and the second to the polarization of the excitation light. To account for the change along all three axes, the polarizability is expressed as a tensor

$$\begin{bmatrix} P_x \\ P_y \\ P_z \end{bmatrix} = \begin{bmatrix} \alpha_{xx} & \alpha_{xy} & \alpha_{xz} \\ \alpha_{yx} & \alpha_{yy} & \alpha_{yz} \\ \alpha_{zx} & \alpha_{zy} & \alpha_{zz} \end{bmatrix} \begin{bmatrix} E_x \\ E_y \\ E_z \end{bmatrix}. \quad (20)$$

The strength of the polarizability of a vibration varies along each of the three axes. This is called the shape of the Raman tensor (polarizability). The shape of the tensor defines the relationship between the incoming and the (Raman-)scattered light, such that the polarization of the incoming and scattered light does not necessarily have to be the

same.[85] These differences in polarizability can be utilized to identify the orientation of bonds in larger samples.

To vary the polarization of the excitation and scattered light, many Raman spectroscopy setups are equipped with a polarizer and an analyzer (Figure 10). By adjusting the settings of these polarization optics to the change of polarization of incoming light to the scattered light, it is possible to identify the average orientation of bonds in the sample. To clarify this, consider a fibrous sample. Fibers have a very anisotropic distribution of bonds. To find the orientation of this bond in the sample, one would orient it as in Figure 10, and set the polarizer to a certain angle and the analyzer to the same setting (assuming there is no polarization shift from incoming to scattered light). The setting is determined by the orientation of the polarization tensor of the (Raman-active) bond vibration. Starting from this setting, spectra would be acquired in steps over 180° , changing the polarizer and analyzer setting after each step. If there was a preferred orientation of this bond in the sample, the peaks assigned to this bond vibration would reach a maximum, somewhere along the 180° . By knowing the orientation of the Raman tensor of this bond vibration, and therefore its polarizability, the orientation of the bond itself can be obtained by these measurements.

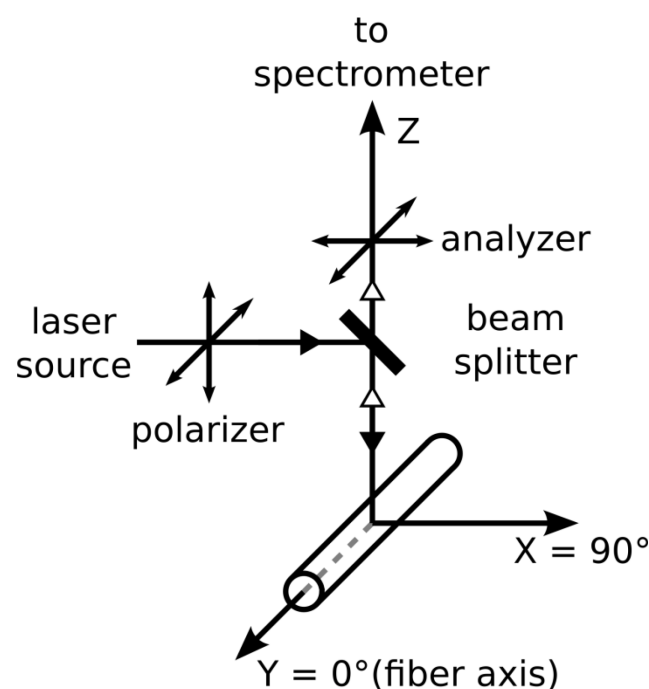


Figure 10 Definition of coordinate system and sample orientation applied in Raman measurements. The path of excitation light is indicated by the black triangles, the path of scattered light by the white ones. (Modified from Lefèvre et al. [4]).

Orientation-Insensitive Raman Spectra

The available setup for Raman microspectroscopy in our lab only allows for excitation with a polarized laser beam. It is therefore necessary to account for the fact that only bonds with their Raman tensor parallel to the polarization plane of the incident light are excited and thus, measurable with this setup. Recently an elegant solution to this issue has been provided by Frisk et al.[87], and was adapted to the use with spectra acquired by Raman microspectroscopy by Lefèvre et al.[88]. It enables one to calculate orientation-insensitive spectra (also called isotropic spectra) from the measurement of four polarized spectra by

$$I^{iso}(3 + 6R_{iso}) = I_{yy} + 2I_{xx} + 4I_{xy} + 2I_{xz} \quad (21)$$

with I^{iso} the isotropic intensity, R_{iso} the depolarization ratio and I_{ij} the intensities of the four measured polarized spectra. The first subscript i in this notation refers to the polarization plane of the incident laser light and the second subscript j to that of the scattered light (Figure 10). The depolarization ratio R_{iso} can be obtained from measuring the depolarization ratio of an isotropic sample.[88] A detailed description of the theory is given in the above mentioned publications.

Resonance Raman Scattering

Figure 9 shows the excitation and emission energy profile in the case of normal Raman spectroscopy. Note that in this case the frequency of the excitation laser is chosen so that its energy is far below the energy necessary to promote the molecule to its first excited electronic state. This is done to prevent sample decomposition through photodecomposition or heating and the occurrence of fluorescence, which produces a much stronger signal than Raman scattering making it impossible to measure a Raman spectrum [85]. In resonance Raman spectroscopy, the excitation frequency is chosen to be close to that of the electronic transition of a particular chromophoric group in a molecule (Figure 11). The result is that the Raman bands corresponding to this chromophoric group are enhanced by 10^3 to 10^5 . [84] In the case of the byssal threads this enables measurements of the modes of DOPA metal interaction even though there is a large fluorescence background.

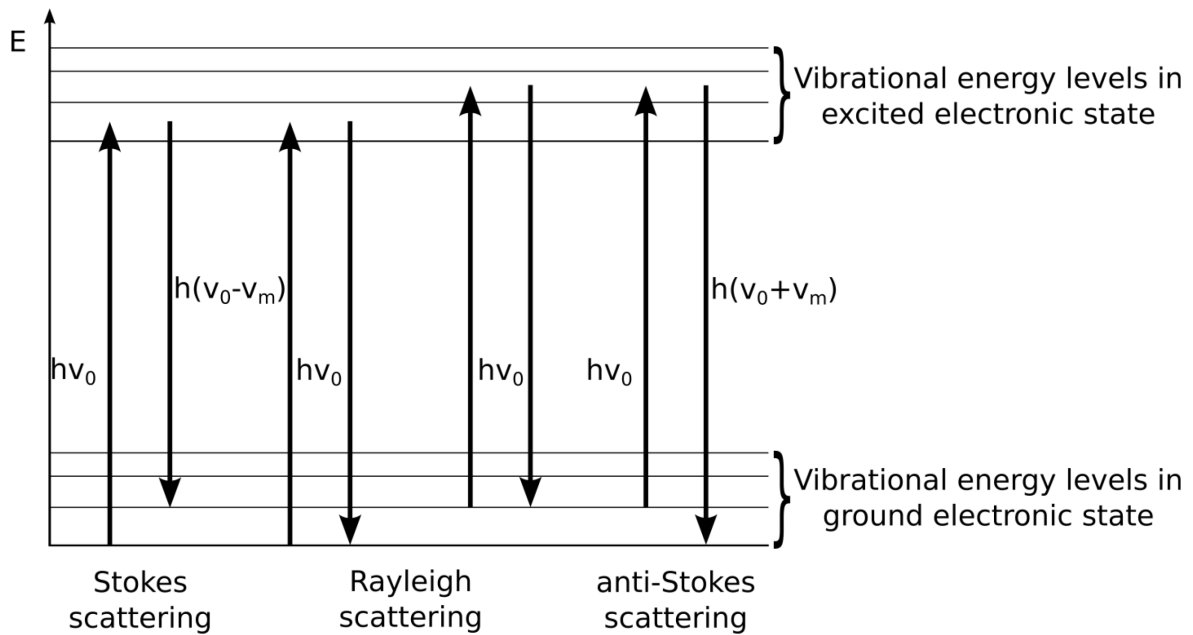


Figure 11 Diagram of the basic process of resonance Raman scattering (modified from Smith and Dent [85]).

2.2.3 Inductively Coupled Plasma - Optical Emission Spectrometry (ICP-OES)

ICP-OES is a method for the quantitative elemental analysis of a sample. It is based on the emission of photons of characteristic wavelengths, when atoms and their ions are excited to higher electronic energy levels.

Usually all atoms of a sample at room temperature are in an energetic ground state. For the valence electrons of an atom this means that they occupy the available orbitals with the lowest possible energy. When a sample is heated, the valence electrons can absorb energy and are elevated to higher orbitals i.e. energetic levels. This is referred to as an excited electronic state. The lifetime of this excited state is short and the electron relaxes to lower open orbitals. During this process electromagnetic radiation of a specific wavelength is emitted. Figure 12 shows the possible transitions of excited valence electrons for hydrogen. Similar diagrams can be drawn for more complex atoms. As depicted in Figure 12, the wavelength of the emitted radiation depends on the transition the electron undergoes during the relaxation. The emitted radiation of a certain wavelength is called an emission line. Every element has its specific emission lines, by which it can be identified.[77,89]

The first step of elemental analysis by ICP-OES is usually to dissolve the sample in a liquid solvent. This solution is converted to a fine mist by pumping it, together with a gas (nitrogen or argon), through a nebulizer. The sample mist is then transported, by the gas flow, to a heated region. As the name of the technique indicates, a plasma torch, usually with an Argon source, is applied in this area. The interaction of the mist with the plasma results in the atomization of the sample. Throughout the process of atomization, the solvent is separated from the sample spray by vaporization. This produces a fine molecular aerosol of the sample. The molecules then dissociate into their atoms resulting in an atomic gas. The atoms of the

gas are ionized and electronically excited by collision with the electrons and ions of the plasma.

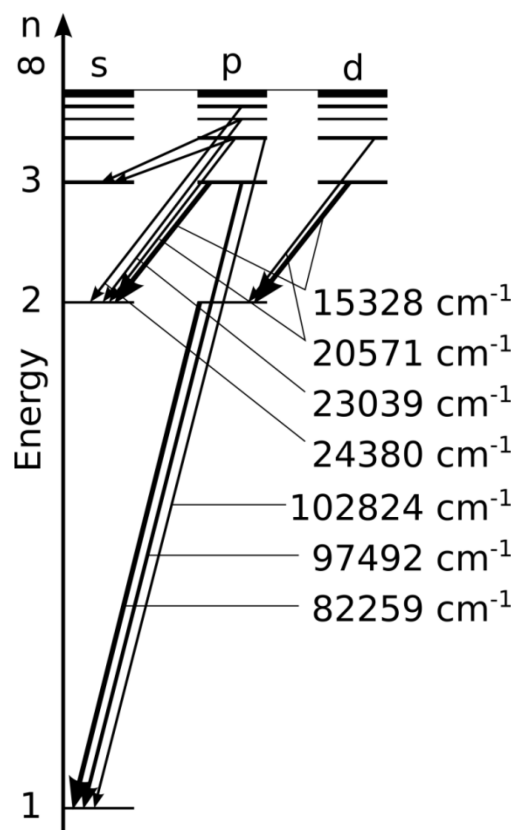


Figure 12 The Grotrian diagram of atomic hydrogen. The arrows indicate allowed relaxations of excited electrons. The thicker the arrow, the more likely the particular relaxation path. The numbers give the wavenumbers of the electromagnetic radiation emitted during the electrons relaxation. (modified from Atkins [77])

It is important to note that in each step of atomization, not all molecules and atoms are dissociated or ionized. This leads to a mix of electronically excited molecules, excited single atoms and excited ions. Therefore, the emission spectrum consists of a molecular as well as two atomic components. However, due to the high temperature of the applied plasma (4000 – 8000 K), the degree of atomization in ICP-OES is higher as compared to other atomization methods used in optical emission spectroscopy. Thus, the molecular component will have only a very small influence on the spectrum. Since the atomization takes place in a chemically inert environment, ICP-OES is also less prone to chemical perturbations, such as oxidation of the analyte. The few chemical interferences in ICP may be overcome by dilution of samples, adjustment of the plasma source or other instrumental conditions.[90,89]

The emitted radiation from the plasma is usually detected axial to the plasma flow direction. For the detection of one element at a time, the emitted radiation is directed into a monochromator, which selects the required wavelengths to detect the element to be measured. Modern setups are capable of measuring many elements at the same time. One of the ways to accomplish this is the use of a two part polychromator. A prism and an échelle grating are positioned in line, so that their directions of dispersion and diffraction of light are perpendicular to each other. The result is that the emitted radiation is split up in two-dimensions, one over different orders of diffraction and the other over a range of wavelengths. This signal is then focused on a two-dimensional CCD-array which detects the samples emission spectrum.[90,89]

The most common problem in ICP is spectral interference of emission lines, when many elements are present in the sample. The use of high-resolution CCD-detectors counteracts this problem. However, in some cases it is necessary to apply advanced background correction techniques or choose a different analytical wavelength.[90]

2.2.4 Amino Acid Analysis

The term amino acid analysis stands for several methods applied to quantify the amounts of individual amino acids in protein-containing samples. In this study, post-column ninhydrin derivatization amino acid analysis was performed. The first step of this procedure is to hydrolyze the sample at 110 °C in 6 M HCl in an oxygen-free environment to cleave the protein into the individual amino acids. The free amino acids are then separated by ion-exchange chromatography.[91–93] The amino acid analyzer used in this study is a high pressure liquid chromatograph separating the amino acids by pH and cationic strength gradients. Separation is enhanced by a temperature gradient, which changes during the course of the run. After the separation step, the amino acids react with ninhydrin, forming colored compounds which absorb at 440 nm and 570 nm wavelength. An integrated dual-channel photometer detects the absorbance at these wavelengths. A linear correlation of area to concentration is established from standard amino acid solutions with known concentrations. With this correlation, it is then possible to derive the concentration of individual amino acids within samples and thus, also the percent mole (mol%) composition of each amino acid [93].

As with all measurement techniques, certain limitations also apply to the form of amino acid analysis used in this study. One significant drawback is that the amino acid Tryptophan cannot be detected by this setup. Furthermore, during hydrolysis, Asparagine (Asn) and Glutamine (Gln) are converted to Aspartic Acid (Asp) and Glutamic Acid (Glu), respectively. It is, therefore, only possible to detect the sum of each of these amino acid pairs as Asx (Asn and Asp) and Glx (Gln and Glu). In the present study, this is of little importance, since the method was only applied to measure the concentration of DOPA in the distal part of the thread. Since DOPA is unstable under protein hydrolysis conditions, it is necessary to protect it by the addition of phenol to the hydrolysis solution. While it is unknown how exactly this

DOPA instability is caused, it is presumed to be due to the elevated levels of chlorine atoms in the hydrolysis solution.[94]

2.2.5 Nanoindentation

The technique of nanoindentation enables the local mechanical characterization of samples with sub-micron resolution. As in larger scale indentation, an indenter tip, usually a diamond of a specific geometry, is pressed into a sample while the resulting force on the tip and its displacement are recorded. From the load displacement curve, one can obtain the local elastic modulus E and hardness H . The following section gives an outline of the method to determine the elastic modulus E and the hardness H , provided by Oliver and Pharr [95]. A load displacement curve of a typical indentation experiment is shown in Figure 13.

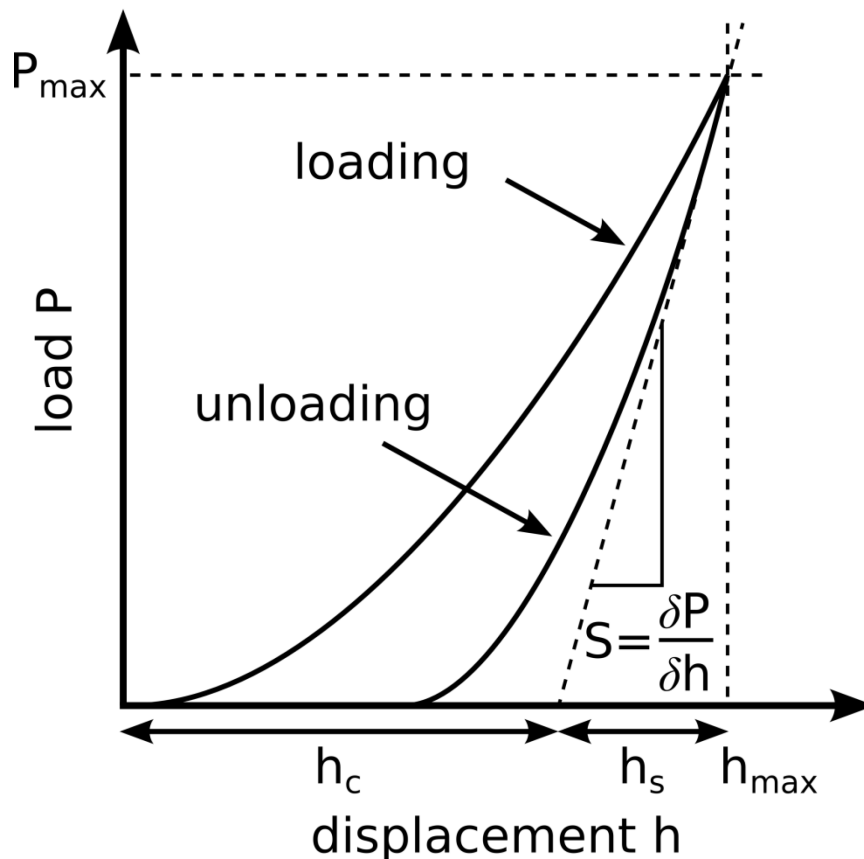


Figure 13 Load displacement diagram of a typical indentation experiment (modified from Oliver and Pharr [95]).

To obtain the elastic modulus E , first the contact stiffness S of the sample-indenter tip configuration and the reduced elastic modulus E_r of the sample are determined. The contact stiffness S is derived from the upper (linear) portion of the unloading data (Figure 13). In this part of the unloading curve S can be approximated as $\frac{\delta P}{\delta h}$, the change of load (P) with the change of displacement h . The contact stiffness S is related to the reduced elastic modulus E_r and the projected area of elastic contact A by

$$S = \frac{\delta P}{\delta h} = \frac{2}{\sqrt{\pi}} E_r \sqrt{A}. \quad (22)$$

This can be rewritten as

$$E_r = \frac{\sqrt{\pi} S}{2 \sqrt{A}}, \quad (23)$$

to obtain an expression by which the reduced modulus E_r can be determined through measurement of the stiffness S .

The area itself is a function of the penetration depth h_c of the tip into the sample (Figure 14), so

$$A = F(h_c). \quad (24)$$

This tip area function F needs to be established experimentally from indentations of a standard material.

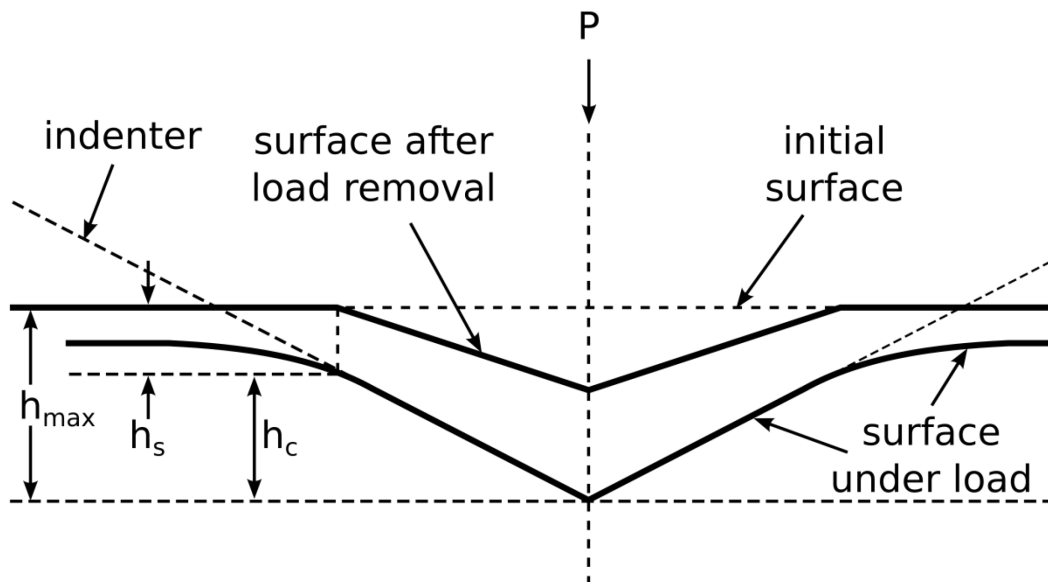


Figure 14 Side view of a typical indentation experiment. During the indentation the surface of the sample deflects under the load P , and relaxes again after the load is removed. The maximum displacement h_{max} of the indenter tip is the sum of the displacement of the sample surface h_s , and the penetration depth h_c of the tip into the sample. (modified from Oliver and Pharr [95])

Since the displacement h_{max} of the indenter tip is the sum of the displacement of the sample surface h_s , and the penetration depth h_c of the tip into the sample (Figure 14), h_c is determined by

$$h_c = h_{max} - h_s. \quad (25)$$

h_c also depends on the geometry of the used indenter tip.

Equation (22) and Figure 13 show that S is the slope of the initial unloading curve. With the relation of displacements given in Equation (25), it is possible to deduce that the displacement of the sample surface is

$$h_s = \epsilon \frac{P_{max}}{S}, \quad (26)$$

with the maximum load P_{max} and the constant ϵ depending on the geometry of the indenting tip. With the definition of these parameters it is now possible to obtain the reduced elastic modulus E_r by measurement of P_{max} and S .

If the Poisson's ratio of the material is known, the elastic modulus can be derived from the reduced elastic modulus by

$$\frac{1}{E_r} = \frac{(1 - \nu^2)}{E} + \frac{(1 - \nu_i^2)}{E_i}, \quad (27)$$

with E and ν the elastic modulus and Poisson's ratio of the sample, and E_i and ν_i the same for the indenter.

As indicated above, the reduced elastic modulus is determined by the elastic part of the unloading curve of the indentation experiment. The elastic relaxation of the material is driven by the relaxation of strained chemical bonds, and not by bonds broken during the loading phase. The reduced elastic modulus therefore provides a measure of the number of strained bonds, rather than one of the strength of chemical bonds of a material.

The second mechanical parameter which can be measured by this method is the hardness H of the material. It is

$$H = \frac{P_{max}}{A}, \quad (28)$$

with A the projected area of contact from Equation (24). Unlike the (reduced) elastic modulus, the hardness measures the resistance of a material to plastic deformation, due to the indenter being pressed into it.

3 MATERIALS

3.1 BYSSAL THREADS

Byssal threads of *Mytilus californianus* were supplied from the laboratory of J. Herbert Waite at the Marine Science Institute of the University of California (Santa Barbara, CA 93106, USA). The mussels were collected from Goleta Pier (Goleta, CA, USA) and kept at 12 – 15°C in tanks with flowing sea water. Mussels were allowed to produce byssal threads for up to 3 weeks. The threads were then collected, washed thoroughly in distilled water and stored in distilled water at about 4°C until testing.

3.2 STANDARDS AND OTHER CHEMICALS

The calibration standard foils for XAS were purchased from Goodfellow GmbH (Bad Nauheim, Germany). The standard solution for amino acid analysis was from purchased from Sykam GmbH (Eresing, Germany). For ICP a 28 element standard solution from Carl Roth GmbH & Co. (Karlsruhe, Germany) was used. All other chemicals were purchased from Sigma-Aldrich (Karlsruhe, Germany).

4 CORE

4.1 AIMS OF THIS STUDY

Previous studies have suggested that histidine-metal coordination bonds play a primary role in the self-healing capability of *Mytilus* byssal threads (see chapter 2, state of the art); however, this was based on exposing threads to treatments known to disrupt His-metal bonding (e.g. EDTA metal chelation, acidic conditions, diethylpyrocarbonate) and observing the mechanical consequences [33,34,50]. Direct proof of the role of metal coordination remains to be substantiated. This study is, therefore, focused on two main goals: (i) the identification of histidine-metal coordination bonds within the core of *M. californianus* byssal threads, and (ii) the tracking of changes in the metal coordination structure throughout tensile loading and healing of the threads. The results of these spectroscopic investigations provide new insights into the self-healing mechanism of the byssus, which will aid in the design of self-healing polymeric materials [35,25,36].

The presence of metals in the thread known to bind to histidine was tested by ICP-OES, and XRF was used to confirm their specific presence in the core of the distal byssal thread portion. In an attempt to identify the binding of metals by histidine, Raman microspectroscopy was applied to longitudinal cross-sections of the *M. californianus* byssal thread core. Lastly, XAS was used to probe the coordination environment of Zn in byssal threads at rest, under tensile loading, after relaxation from tensile loading and after healing from tensile loading followed by analysis of the XANES and EXAFS regions. Taken together, these measurements provide substantial direct evidence for the role of metal coordination in the deformation and self-healing behavior of *Mytilus* byssal threads.

4.2 EXPERIMENTAL PROCEDURES

4.2.1 Inductively Coupled Plasma - Optical Emission Spectrometry (ICP-OES)

The distal portions of 25 *M. californianus* byssal threads were dissected from the rest of the thread. From these, 5 groups of 5 threads were pooled as one sample for ICP-OES. The samples were freeze dried and then weighed. Subsequently, they were dissolved in 500 μl aqua regia (167 μl HNO_3 + 333 μl HCl) at 40°C for 24h. The resulting solutions were diluted at a 1:10 ratio with Millipore H_2O and emission spectra were recorded with an ICP-OES analyzer (Optima 8000, Perkin-Elmer). A concentric glass nebulizer (type A, Meinhard, Golden, CO, USA) equipped with a glass cyclonic spray chamber (Meinhard, Golden, CO, USA) was used, together with an Argon plasma torch, to atomize the sample solutions. The setup uses a dual échelle polychromator in combination with a CCD detector, as described above, to record sample spectra. Each sample was measured two times. Standard solutions, containing the elements in question at a number of different concentrations, were measured to obtain the correlation of element concentration and intensity of spectral lines. Analysis was done with the devices measurement software WinLab32 for ICP-OES.

4.2.2 X-Ray Fluorescence (XRF)

For the XRF measurement, the core region of the distal portion of 3 threads was separated from its cuticle using a cryo-microtome (HM560, Microm) and a micro laser dissection device (P.A.L.M. Microlaser Technologies GmbH, Germany, with a pulsed UV-A laser at 355 nm, CryLas GmbH, Germany). XRF measurements were carried out at the KMC-2 beamline at BESSYII (Berlin-Adlershof, Germany) with an x-ray energy of 11000 eV, using a SiGe(111) double-crystal monochromator. The fluorescence of the samples was detected with an energy-dispersive detector (Röntec X-Flash). Beamline KMC-2 operates on a bending magnet and high-order harmonics are removed by harmonic rejection mirrors in front of the monochromator. The ring current was between 150 and 300 mA during measurements.

4.2.3 Raman Spectroscopy

Distal byssal thread portions from *M. californianus* were cut longitudinally to 10 μm thick sections using a cryo-microtome (HM560, Microm). Spectra of the byssus core were obtained with a Confocal Raman Microscope (alpha300, WITec, Germany) equipped with a piezo-scanner (P-500, Physik Instrumente, Karlsruhe, Germany). The frequency doubled linearly polarized Nd: YAG laser ($\lambda = 532$ nm, WITec, Germany) was focused on the sample through a 60x water immersed objective (Nikon, NA = 1.0). The laser power on the sample was set to 15mW. The spectra were acquired using a thermoelectrically cooled CCD detector (DU401A-BV, Andor, Belfast, North Ireland) behind a 600 g mm^{-1} grating spectrograph (UHTS 300, WITec, Ulm, Germany) with a spectral resolution of 3 cm^{-1} . The spatial resolution of the setup is calculated to 325 nm using the simplified Rayleigh criterion

$$r = 0.61 \frac{\lambda}{NA} \quad (29)$$

with numerical aperture NA and excitation laser wavelength λ .

The ScanCtrlSpectroscopyPlus software (Version 1.38, WITec, Ulm, Germany) was used for measurement setup. The core was identified visually and the sections were aligned as depicted in Figure 10. At least 3 measurements were taken from different spots within the core area for each setting of the polarizer and analyzer. These settings were chosen as described above and as depicted in Figure 10 to be 0°- 0°, 90°- 90°, 90°- 0° and 0°- 90° (polarizer- analyzer). A polynomial background was removed from the spectrum with the OPUS software package version 7.0 (Bruker Optik GmbH). The calculation of the isotropic spectrum was performed with the OriginPro Software version 8.6 (OriginLab Corporation, Northampton, MA 01060 USA), according to the method described above and in Lefèvre et al. [88]. The depolarization ratio R_{iso} , appearing in Equation (21), was determined to be 0.21 by measurements of gelatin.

The byssus core isotropic Raman spectrum was deconvoluted into individual peaks in the region from 1520 - 1730 cm^{-1} using a previously described method [96]. Initial assessment of number and position of peaks was determined by second derivative spectra, as well as previous knowledge of expected secondary structures and side chains based on protein sequence [34] and related materials (e.g. silk and collagen). During fitting, efforts were made to minimize the number of components, while avoiding excessive peak widths (e.g. $>35 \text{ cm}^{-1}$). If wider peaks were observed, another peak was added in the region. Fitting was performed using the OPUS software package. Based on initial assessment criteria, the spectrum was determined to consist of eight individual peaks centered at 1550, 1570, 1587, 1608, 1630, 1650, 1667 and 1685 cm^{-1} . The eight bands were entered into the fitting software with an initial width of 20 cm^{-1} and were permitted to assume a mixture of Gaussian and Lorentzian functions. Fitting was performed using the Levenberg-Marquardt method through numerous iterations until a reasonable fit was achieved.

4.2.4 X-Ray Absorption Spectroscopy (XAS)

Sample Preparation

Prior to the XAFS measurements threads were dried and for each sample the ends of 5 threads were glued side by side to plastic strips. On top of each plastic strip, another strip was glued to maintain good fixing of the threads from top and bottom (Figure 15). The sample length between the gluing points was 4mm. After gluing, the samples were allowed to cure for 24 hours under a fume hood. During this time the open thread parts were covered by a plastic foil, to prevent the deposition of glue fumes on the thread surface.

Before stretching each sample to its respective length, the samples were allowed to rehydrate for at least one hour in Millipore water. The samples were clamped with the plastic strips and fully submerged in Millipore water throughout tensile testing. The tensile testing was carried out on a custom built motorized tensile tester, equipped with a 50N load cell. The applied strain rate was $5 \times 10^{-4} \text{ s}^{-1}$ and the strain was measured by video extensimetry. The samples for measurements on strained threads were dried (at least 3 days at room temperature) keeping the strain fixed at 10%, 25% and 40%. These samples were glued to plastic frames to prevent them from relaxing during the XAFS measurements.

The 25% strained and relaxed samples were dried after being relaxed and unclamped. The 25% strained and healed samples were relaxed and unclamped and rested in Millipore water for 5 days at RT. After this time, these samples were also dried to stop any additional healing. An assessment of the effects of drying and (wet) relaxation on the stress in distal byssal threads stretched to 10%, 25% and 40% strain is given in Appendix 8.1

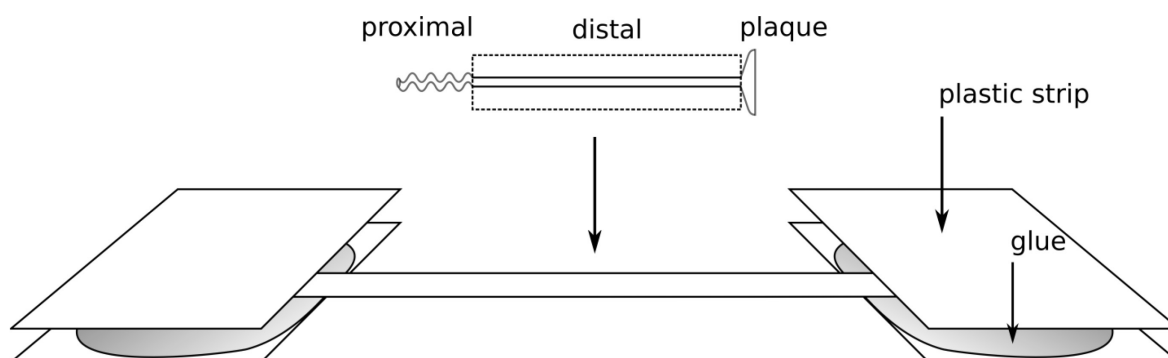


Figure 15 Schematic drawing of the sample preparation for tensile testing and subsequent XAS measurements.

Data Acquisition

The XAFS measurements were carried out at the Zn K-edge (9659 eV) on the KMC-2 beamline at the BESSY II synchrotron (Berlin-Adlershof, Germany), using a SiGe(111) double-crystal monochromator. Beamline KMC-2 operates on a bending magnet and high-order harmonics are removed by harmonic rejection mirrors in front of the monochromator. The ring current was between 150 and 300 mA during measurements. Throughout the measurement the beam intensity was kept stable at 70% of the maximum beam intensity (at 10300 eV) with MOSTAB electronics. The beam intensity, before and after the sample, was recorded with ionization chambers. Simultaneous to the fluorescence measurement of the samples with an energy-dispersive detector (Röntec X-Flash), a zinc standard was measured in transmission with a Si-PIN photodiode. The beam size on the sample was approximately $0.5 \times 0.5 \text{ mm}^2$. The EXAFS data was collected in the range from 9550 to 10400 eV with the following settings (energies relative to edge position): the pre-edge region from -110 to -20 eV was sampled with steps of 10 eV, the pre-edge region from -20 to -15 eV was sampled with steps of 1 eV, the edge region from -15 to +5 eV was recorded in steps of 0.2 eV, the post-edge XANES region from +5 to +20 eV was collected in steps of 0.5 eV and the EXAFS region from +20 to +800 eV was sampled with steps of 2 eV. For each data point the exposure time of the fluorescence detector was 6 s. At least 6 spectra were recorded for each sample to test the reproducibility of the spectra and to ensure that no radiation damage occurred. All scans of a single sample were averaged to improve the signal to noise ratio.

Data Reduction

The XAFS spectra were deglitched, energy calibrated, aligned, averaged and background corrected with the Athena module of the Demeter XAS software package [83]. The edge position of each spectrum was set to the energy at the first maximum of the first derivative.

For each spectrum the energy calibration was performed according to the simultaneously collected spectrum of a Zn foil standard. The edge step $\Delta\mu_0(E)$ for normalization was determined by fitting a linear function to the pre-edge region and a quadratic polynomial to the post edge data. The background function $\mu_0(E)$ was modelled with a spline function using the autobk algorithm of Athena. The signal below 1 Å in r-space was minimized by setting the cutoff parameter $R_{bkg} = 1.05 \text{ \AA}$. After conversion to k-space the usable data range was determined to be from 2 to 9.5 Å⁻¹.

Data Analysis

XANES

A comparative approach to the analysis of the XANES region was applied in this study. For this, the spectral region from -20 eV to +80 eV (with respect to the edge energy E_0) of the byssal thread spectra in the unstrained state was compared to inorganic and organic standards containing Zn. These standards were finely powdered samples of ZnO, ZnCl₂, insulin, *Nereis virens* jaws, and mixtures of imidazole and a poly-histidine peptide with Zn in the ratio 3:1. The acquired spectra were pre-treated as described before and then examined for common features and shifts of the edge energy. The XANES data was analyzed using the Athena module of the Demeter XAS software package [83].

EXAFS

The EXAFS data was analyzed using the Artemis module of the Demeter XAS software package [83]. Based on the previous knowledge about the protein composition of the core, the protein data base (PDB) was searched for proteins known to coordinate Zn by histidine (His) and aspartate (Asp). Based on a previous publication on the classification of Zn coordination sites in proteins, the expected number of 1st shell ligands (coordination number) was between 3 and 6 [97]. However, as discussed below, the results of the XANES analysis indicated the maximum possible coordination number to be between 4 and 5. Therefore, the fitting attempts were limited to coordination numbers within this range. Using Artemis, theoretical model data was constructed from the crystallographic data in the protein data base (PDB) of the Zn sites in numerous proteins. However, the crystallographic data of one of the zinc sites in human collagenase 3 (MMP-13, PDB entry 4fu4), containing 3 His and 1 Asp, was selected out of all tested structures, since it allowed the best fit of the theoretical model to the data. For the construction of models, the coordinates of all atoms within 6 Å from the Zn atom were extracted from the PDB data with PyMol [98], using a previously described procedure [99]. The program FEFF (with Artemis) was used to calculate the theoretical scattering amplitudes $f(k)$ and the phase-shifts $\delta(k)$. The theoretical model was built from the most important scattering paths contributing to the r-range of interest. All fits were performed with Artemis applying a Hanning-shape window function. Typical measurement uncertainty in R is 0.2 Å. The value of the amplitude factor $s_0^2 = 0.926$ was determined from the fit of a ZnO standard. The number of the closest nitrogen atoms (i.e. the degeneracies of the corresponding scattering paths) of His-residues was fit. The number of the closest carbon atoms of His-residues and the closest oxygen and carbon atoms of Asp-

residues were defined relative to the number of the closest nitrogen atoms of His-residues. This was done to test the initial hypothesis that the Zn-coordination environment is not changing in the course of tensile deformation. After a stable fit was obtained, the defined degeneracies were tested for stability by allowing them to vary. However, if this procedure did not produce a stable fit of the respective degeneracy, it was allowed to vary throughout the fit. All other fitting parameters were first allowed to vary with the fit, and were then either left to vary during the fitting procedure, or stepped in the fixed state until a good fit was obtained. Throughout the whole fitting procedure, the maximum allowed number of variables was two-thirds of the number of independent points of the data in the fitting window. After a good fit for the first shell was established, the second shell paths were added. All obtained parameters were tested for stability by variation of the initial guess values.

4.3 RESULTS

4.3.1 Resting State

Inductively Coupled Plasma - Optical Emission Spectrometry (ICP-OES)

ICP-OES was performed to confirm the presence of Cu and Zn in the distal byssal threads used for the XAS measurements. The content of these metals was $0.37 \pm 0.17 \mu\text{mol/g}$ of Cu and $1.04 \pm 0.12 \mu\text{mol/g}$ of Zn.

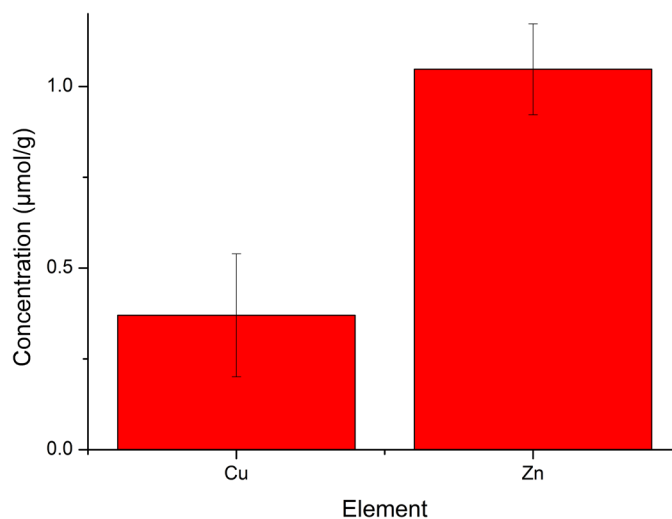


Figure 16 Concentrations of copper (Cu) and zinc (Zn) in native byssal threads from *M. californianus*. Values are the means of 2 measurements per sample, with 5 samples measured. The error bars are standard deviations of all measurements grouped together.

X-Ray Fluorescence

The XRF spectrum of the byssus core (Figure 17) shows the presence of Cu, Zn, Cl and S in the core. The Ar peak comes from the air surrounding the sample.

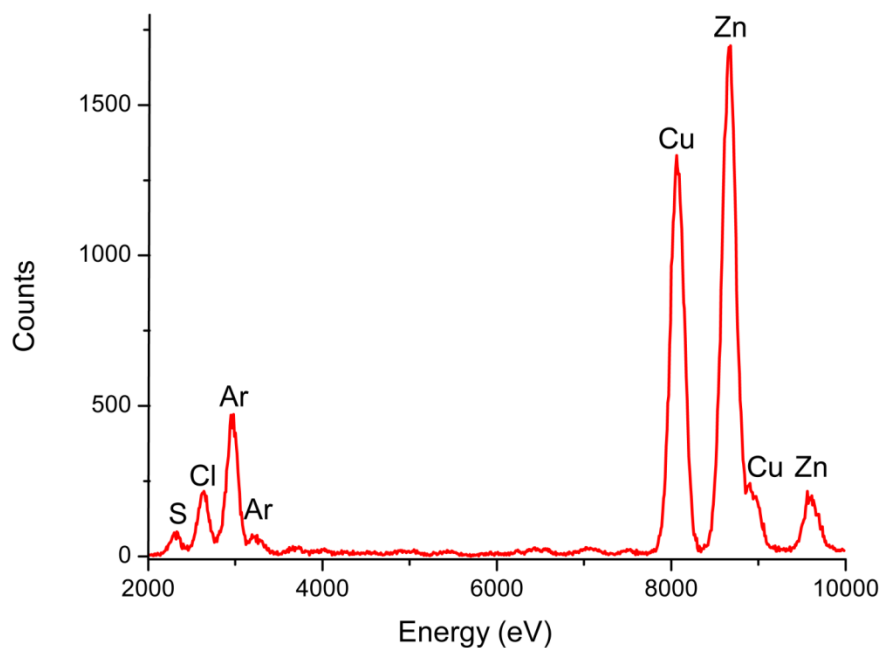


Figure 17 XRF spectrum of the *M. californianus* byssal thread core with an x-ray excitation energy of 11000 eV. The spectrum shows the presence of Cu, Zn, Cl and S in the core. The Ar peak comes from the air surrounding the sample.

Raman Spectroscopy

Raman fitting analysis of the amide I and II region from the byssal thread core (Figure 18) led to the identification of bands at 1570 cm^{-1} , 1587 cm^{-1} and 1608 cm^{-1} , which could be related to the metal free $N_{\tau}\text{-H}$, N_{π} His-tautomer and metal binding via the $N_{\tau}\text{-H}$, $N_{\pi}\text{-M}$ and the $N_{\tau}\text{-M}$, $N_{\pi}\text{-H}$ His-tautomers, respectively [100,101]. The assignment of these bands, based on the currently available literature, will be further touched upon in the discussion. Other bands, unrelated to His, were located at 1550 cm^{-1} , 1630 cm^{-1} , 1650 cm^{-1} , 1667 cm^{-1} and 1685 cm^{-1} . All of these bands can be related to protein secondary structures. Bands in the region of 1550 cm^{-1} can be assigned to α -helical [102] or β -sheet [103] structures. Previously, bands around 1636 cm^{-1} have been observed in gelatin [104]. Therefore, the fitted band at 1630 cm^{-1} could potentially be related to vibrations of the collagen-like domain in the preCols. The peak at 1650 cm^{-1} is most commonly assigned to α -helical structures [105,102]. Both, C=C stretching of the collagen triple helix [106] and C=O stretching of beta-sheet structures [96] give rise to bands close to or at 1667 cm^{-1} . The band at 1685 cm^{-1} has previously been assigned to disordered, non-hydrogen-bonded structures [106] and beta-turns [96].

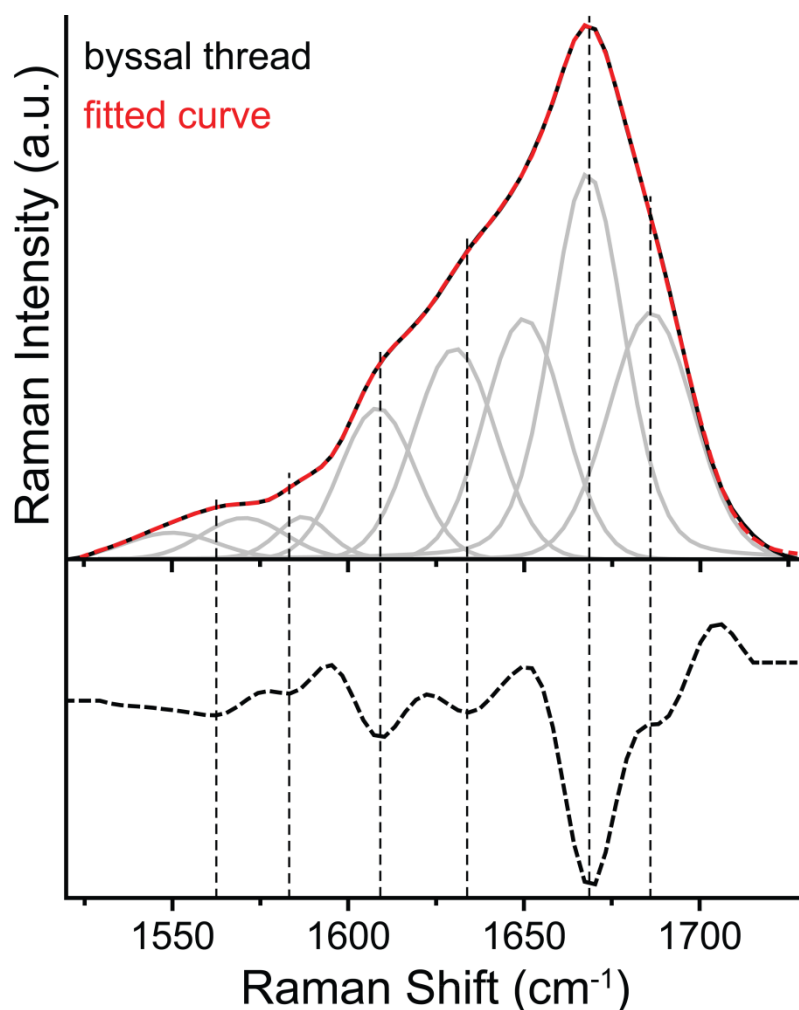


Figure 18 Isotropic Raman spectrum and second derivative of the amide I/II region of the core of native *M. californianus* distal byssal threads. The grey peaks and the red line are the result of the fitting procedure described in the experimental section. The dotted vertical lines indicate peak positions as determined by minima of the second derivative. For the second derivative minima at about 1565 cm^{-1} and 1635 cm^{-1} the fitted peaks exceeded the width limit, so each had to be split into two individual peaks.

X-Ray Absorption Spectroscopy

XANES

The coordination geometry of the Zn sites in byssal threads was investigated by the qualitative analysis of the XANES region. Figure 19 shows a comparison of the byssal thread Zn K-edge XANES region with other organic materials, which coordinate Zn by histidine or imidazole. The intensity of the Zn K-edge spectra white line has been shown to be indicative of the coordination number of Zn, with values of 1.5 or greater associated with octahedral coordination and values less than 1.5 associated with tetrahedral Zn-coordination [107]. The white line intensity of the byssal thread spectrum was about 1.4, whereas the intensities of the other measured samples were 1.3 or below – including insulin, which is known to exhibit

tetrahedral Zn coordination. Thus, Zn in the byssal threads appears to possess a coordination number between 4 and 6 atoms in the first coordination shell. In the spectra of the organic standards, a double peak was observed, which is missing in the spectrum of the byssal threads. The intensity ratio of this double peak was shown to be sensitive to the angle between the Zn-N bond and the N-C bonds in the histidine-based Zn coordination in insulin [107]. The Zn K-edge position of the byssal thread spectrum was determined to $E_0 = 9662.4$.

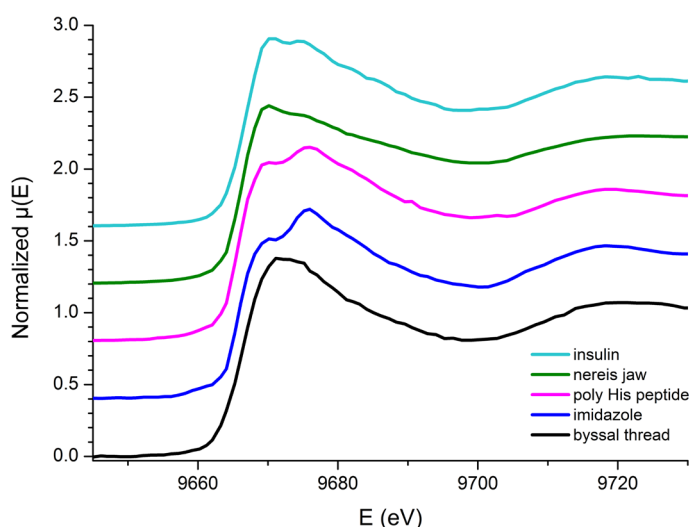


Figure 19 XANES spectra at the Zn K-edge (9659 eV) of unstretched byssal threads and organic materials coordinating Zn by histidine or imidazole.

EXAFS

Based on the XANES white line intensity and the most probable Zn-binding amino acids found in the byssus core, EXAFS models were fitted with both 4 (Table 7 in Appendix 8.2) and 5 (Table 2) first shell N/O ligands, corresponding to a mixture of His and Asp amino acid ligands. Models with 4 first shell ligands were not preferred, as they necessitated a change the amplitude reduction factor s_0^2 obtained from the ZnO standard. In contrast, satisfactory fitting models with 5 first shell N/O ligands were achieved while restricting the value of s_0^2 to the one obtained from the standard. After screening numerous models based on crystallographic data of Zn binding sites with 5 ligands from the PDB, the most reasonable fit was obtained with a model based on the collagenase, MMP-13. This model possessed 2.4 N and 2.6 O atoms in the first coordination shell and C atoms in the second shell at distances correlating to His and Asp residues. A summary of parameters derived from this EXAFS fitting analysis is displayed in Table 2, and the fit in r-space and k-space is given in Figure 21. It must be noted that due to their similar atomic number, it is nearly impossible to distinguish between scattering resulting from N and O atoms. Therefore, the actual number of N and O in the first coordination shell could vary from the ones determined by the fit. Nonetheless, the speciation of longer Zn-N/O bonds and shorter Zn-N/O bonds in the first coordination

shell is significant and noteworthy. The bond lengths of these two groups are in agreement with literature values for Zn-bonds of His, Asp/Glu and H₂O [108].

As described in the experimental section, the initial model for the unstrained threads was deduced from theoretical data for Zn coordination by histidine and aspartate. The numbers of second shell C atoms were therefore constrained to values fitting with this model initially. To test this assumption, the dependencies of long and short distance second shell C atoms were switched; however, this resulted in a concurrent switch in the distances of the two groups of C atoms - supporting the initial assignment of dependencies of the number of second shell C atoms.

4.3.2 Tensile Loading

XANES

The XANES spectra of byssal threads during tensile loading, after relaxation and after healing also have a white line intensity of about 1.4 and lack any additional features, correlating to the coordination geometry around the Zn atoms within the samples (Figure 20). Notably, however, significant shifts of the Zn K-edge position compared to the edge position of the unstrained sample were observed. The shifts, compared to the edge position of the unstrained sample, at the given thread conditions were as follows: $\Delta E_0(10\%) = +0.55$ eV, $\Delta E_0(25\%) = -0.97$ eV, $\Delta E_0(40\%) = -2$ eV, $\Delta E_0(\text{relaxed}) = -1.36$ eV and $\Delta E_0(\text{healed}) = -1.18$ eV. Shifts in the edge position occur due to variations of the core electron energy levels, which are caused by changes in the charge distribution in the coordination environment of the absorbing atom [81]. Therefore, the observed edge energy shifts indicate changes in the coordination environment, affecting the charge distribution around the central Zn atoms.

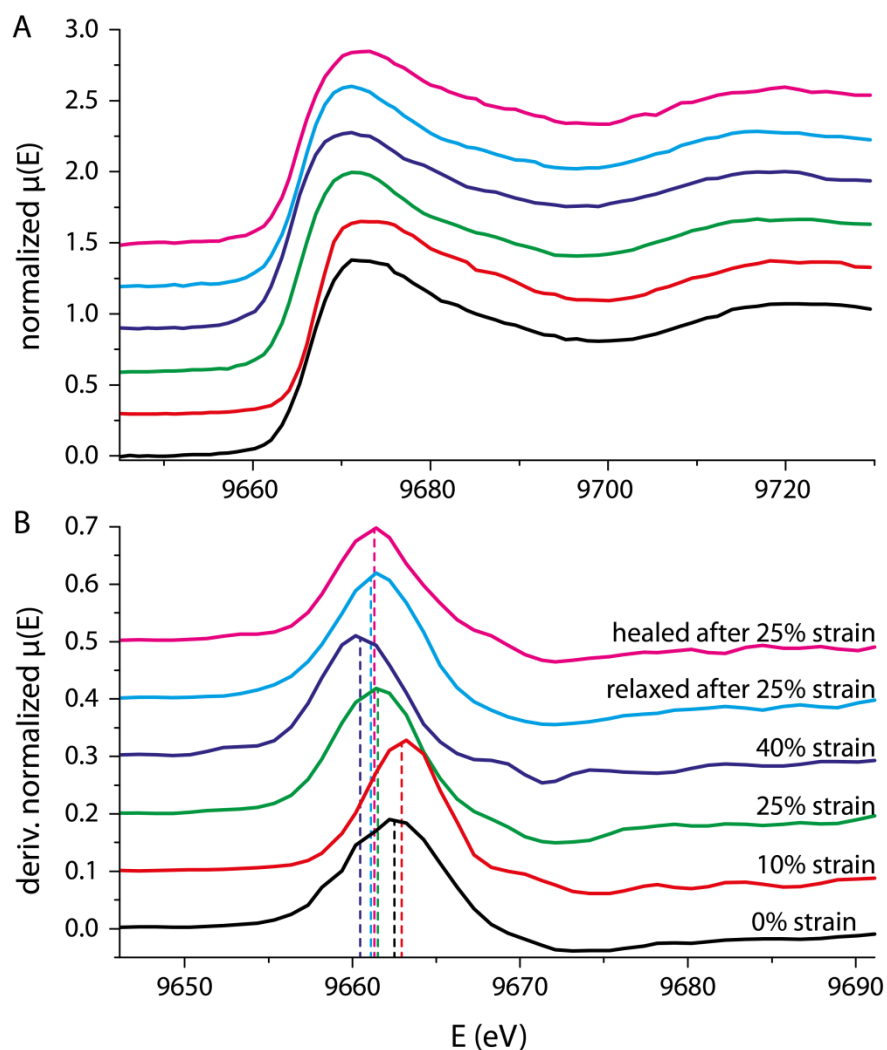


Figure 20 XANES spectra at the Zn K-edge (9659 eV) of byssal threads at 0%, 10%, 25% and 40% strain, as well as threads stretched to 25% and relaxed, and stretched to 25% and healed for 5 days. **A)** Normalized $\mu(E)$ spectra - all spectra have white line intensities below 1.5. **B)** First derivative of normalized $\mu(E)$ - the edge energy (E_0) shifts significantly during stretching and healing (absolute shift values are given in the text above the figure).

EXAFS

The coordination environment of Zn in the thread was probed for mechanically induced changes by applying EXAFS fitting analysis to the XAFS spectra of byssal thread samples during tensile loading, after relaxation and after healing. As described in chapter 4.2.4, the approach for fitting the stretched, relaxed and healed threads was to begin with the same model used in the native state (i.e. assume no changes), and if this did not produce a satisfactory fit, the fitting parameters were freed until a reasonable and logically consistent fit was achieved. At 10% thread strain, the model of the unstrained threads could be maintained by including second shell C atoms at distances and numbers in agreement with those of histidine and aspartate – thus, justifying this approach. However, beginning from 25% strain this initial model had to be altered, indicating changes to the Zn coordination

environment (also supported by the XANES edge shift (Figure 20)). The most reasonable fitted models of the data are displayed in r-space and k-space in Figure 21 and the parameters of the fitted models are summarized in Table 2. The fitted lengths of Zn-N/O bonds are all in agreement with the literature values for Zn-coordination bonds of His, Asp/Glu and H₂O [108]. In the stretched, relaxed and healed thread samples, clear changes are observed in the bond lengths, the relative amount of short and long Zn-N/O bonds ($N/O_{\text{long}}:N/O_{\text{short}}$) and the ratio of second shell C to first shell N/O atoms (C:N/O). The trends in these data are summarized in Table 3 and visualized in Figure 22-24. Figure 23 and 24 indicate that during thread stretching, the average Zn-N/O bond length increases by up to 1.5%, remains increased in relaxed threads, but returns to near native levels in healed threads. More specifically, Figure 22A-B reveals that the shorter Zn-N/O bonds increase in length at 10% strain, but decrease to near native levels in all other samples. The longer Zn-N/O bonds, on the other hand, do not increase in length at 10% strain, but increase significantly at 25% and exhibit even higher lengths in relaxed threads. Notably, the length of the longer Zn-N/O bond returns to near native levels in healed threads. Changes in the $N/O_{\text{long}}:N/O_{\text{short}}$ ratio followed a similar trend to bond length – namely, the relative number of longer bonds increases at 25% strain, remains elevated in relaxed threads, and drops to near-native levels in healed threads. As indicated in Figure 23B and 24B, the C:N/O ratio remained essentially constant through stretching, relaxing and healing, with the notable exception of the 40% strained threads, which exhibited a sharp drop in the number of second shell C atoms (associated with AA ligands) – likely due to exchange of AA ligands with H₂O molecules. It is also worth mentioning that at 40% strain, fitting was no longer able to distinguish between groups of long and short bonds; hence, the 40% strain data is absent from Figure 22C.

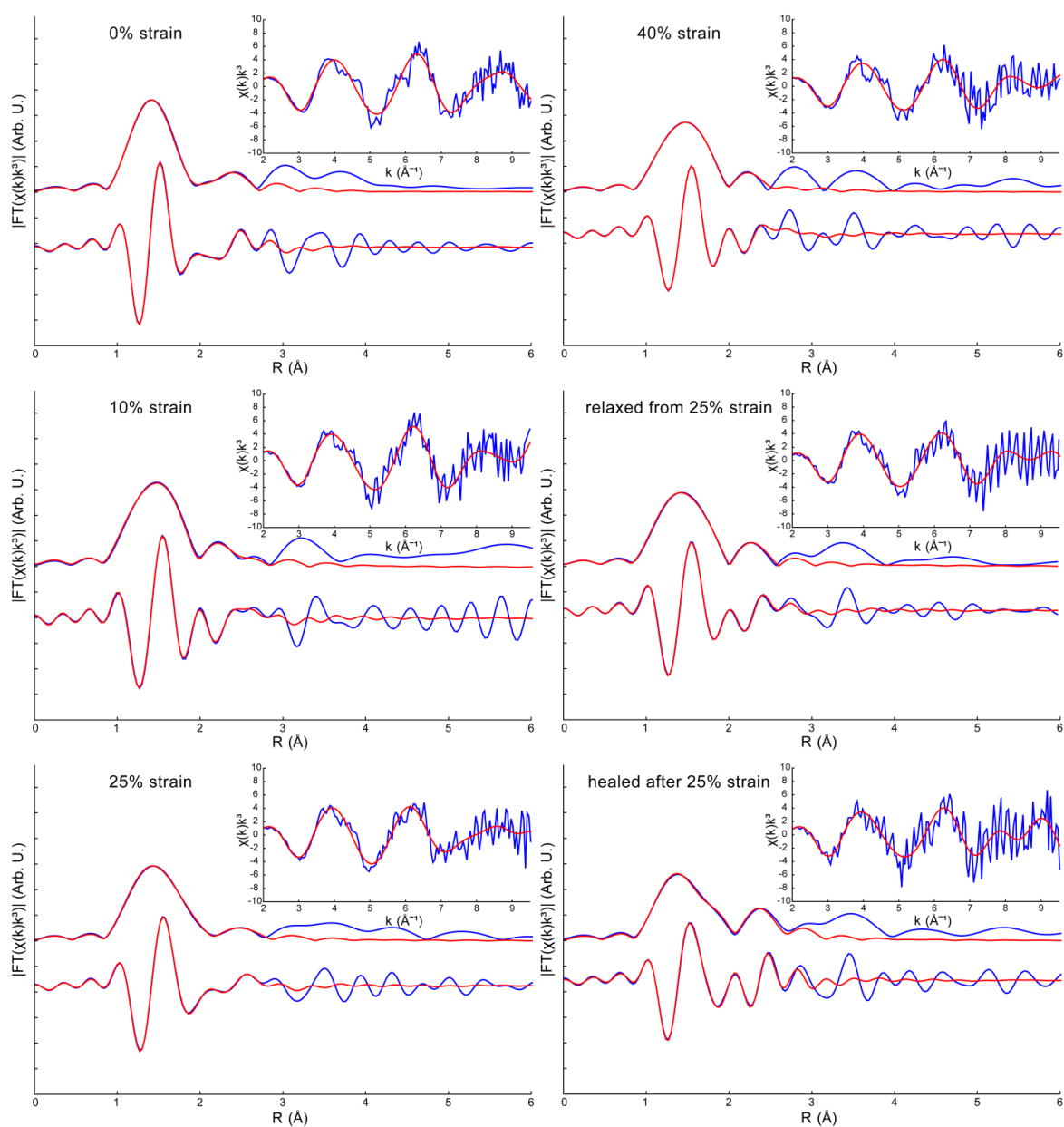


Figure 21 R-space (magnitude and real part of the Fourier transform) EXAFS of the XAFS data (blue line) and the fits (red line), of byssal threads during tensile loading, after relaxation and after healing. The insets show the corresponding k-space data (blue line) and the fits (red line).

Table 2 EXAFS fitting results for Zn K-edge spectra of *M. californianus* byssal threads prior to and during tensile loading, after relaxation and after healing.

EXAFS fitting results									
sample	E_0 (eV)	1 st coordination shell							
		N/O_{long}			N/O_{short}				
		R (Å)	N	σ^2 (Å ²)	R (Å)	N	σ^2 (Å ²)		
0% strain	5.08 f	2.03 (0.01)	2.4 (0.1)	0.010 (0.001)	1.94 (<0.01)	2.6	5- N/O_{long}	0.004 (<0.001)	
10% strain	5.26 f	2.03 (0.01)	2.3 (0.2)	0.013 (0.002)	1.97 (<0.01)	2.7	5- N/O_{long}	0.003 (<0.001)	
25% strain	5.26 f	2.06 (0.01)	2.9 (0.4)	0.006 (<0.001)	1.95 (<0.01)	2.1	5- N/O_{long}	0.006 (<0.001)	
40% strain	5.46 f	2.01 (0.01)	4.7 (0.2)	0.006 (<0.001)	-	-	-	-	-
relaxed (25%)	5.44 f	2.07 (0.01)	2.8 (0.4)	0.006 (0.001)	1.95 (<0.01)	2.2	5- N/O_{long}	0.005 (<0.001)	
healed (25%)	5.41 f	2.04 (0.01)	1.8 (0.2)	0.008 (0.002)	1.96 (<0.01)	3.2	5- N/O_{long}	0.010 (<0.001)	
2 nd coordination shell									
sample	E_0 (eV)	C_{long}			C_{short}				
		R (Å)	N	σ^2 (Å ²)	R (Å)	N	σ^2 (Å ²)		
0% strain	5.08 f	2.89 (0.01)	4.8 $2 \times N/O_{long}$	0.013 (0.002)	2.57 (0.02)	1.3	$\frac{1}{2} \times N/O_{short}$	0.008 (0.003)	
10% strain	5.26 f	2.91 (0.01)	4.6 $2 \times N/O_{long}$	0.010 (0.002)	2.58 (0.02)	1.3	$\frac{1}{2} \times N/O_{short}$	0.008 (0.004)	
25% strain	5.26 f	2.95 (0.01)	4.1 (0.9)	0.013 (0.003)	2.66 (0.01)	2.3	(0.3)	0.003 (0.003)	
40% strain	5.46 f	2.91 (0.02)	2.4 (1.2)	0.014 (0.005)	2.54 (0.02)	1.0	(0.4)	0.010 (0.005)	
relaxed (25%)	5.24 f	2.85 (0.01)	4.1 (0.9)	0.014 (0.004)	2.52 (0.02)	1.1	$\frac{1}{2} \times N/O_{short}$	0.006 (0.004)	
healed (25%)	5.41 f	2.90 (0.01)	3.7 $2 \times N/O_{long}$	0.003 (0.002)	2.58 (0.01)	1.6	$\frac{1}{2} \times N/O_{short}$	0.003 (0.001)	

s_0^2 was set to 0.926 according to the fits of the standards. The overall degeneracy of 1st shell paths (N/O) was set to 5. f indicates fixed parameters. Numbers in parentheses are fit uncertainties. If no uncertainty is given, the formula for the calculation of the parameter is stated.

Table 3 Measures derived from the EXAFS fitting results prior to and during tensile loading, after relaxation and after healing.

Measures derived from the EXAFS fitting results			
sample	avg. $\Delta R_{1st\ shell}$	C : N/O	$N/O_{long} : N/O_{short}$
0% strain	-	1.22 (0.1)	0.92 (0.1)
10% strain	0.59 (0.44)	1.19 (0.2)	0.86 (0.1)
25% strain	1.47 (0.94)	1.27 (0.2)	1.40 (0.5)
40% strain	1.13 (0.5)	0.71 (0.3)	-
relaxed (25%)	1.72 (0.98)	1.05 (0.1)	1.28 (0.4)
healed (25%)	0.12 (0.66)	1.05 (0.2)	0.58 (0.1)

For the calculation of C : N/O ratios the overall degeneracies of C and N/O, determined by the EXAFS fits, were used. At 40 % strain it was not possible to distinguish between N/O_{long} and N/O_{short} , therefore, no $N/O_{long} : N/O_{short}$ ratio was calculated. Calculated SD values for the ratios are given in parenthesis. The average (weighted by path degeneracy) of 1st shell bond lengths was used for the calculation of the avg. $\Delta R_{1st\ shell}$. Uncertainties calculated from the uncertainties of the fit parameters are given in parenthesis.

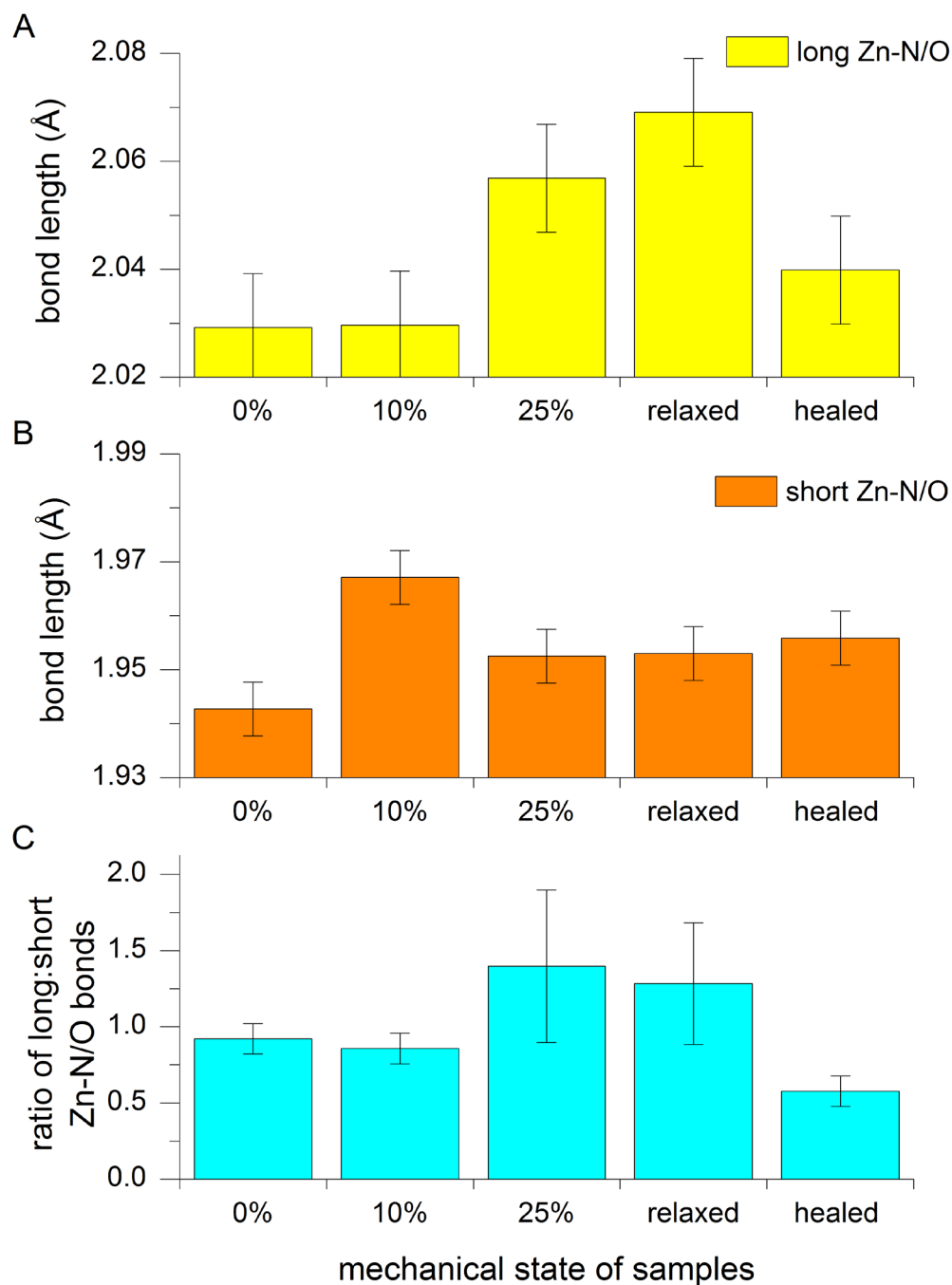


Figure 22 Visualization of EXAFS fitting results for Zn K-edge spectra of *M. californianus* byssal threads prior to and during tensile loading, after relaxation and after healing. Relaxed and healed refer to samples relaxed and healed respectively, after being strained to 25%. **A)** Length of long Zn-N/O bonds. **B)** Length of short Zn-N/O bonds. **C)** The ratio of long to short 1st shell ligand-Zn bonds. Error bars in A and B are fit uncertainties. Error bars in C are uncertainties calculated from the uncertainties of fit parameters.

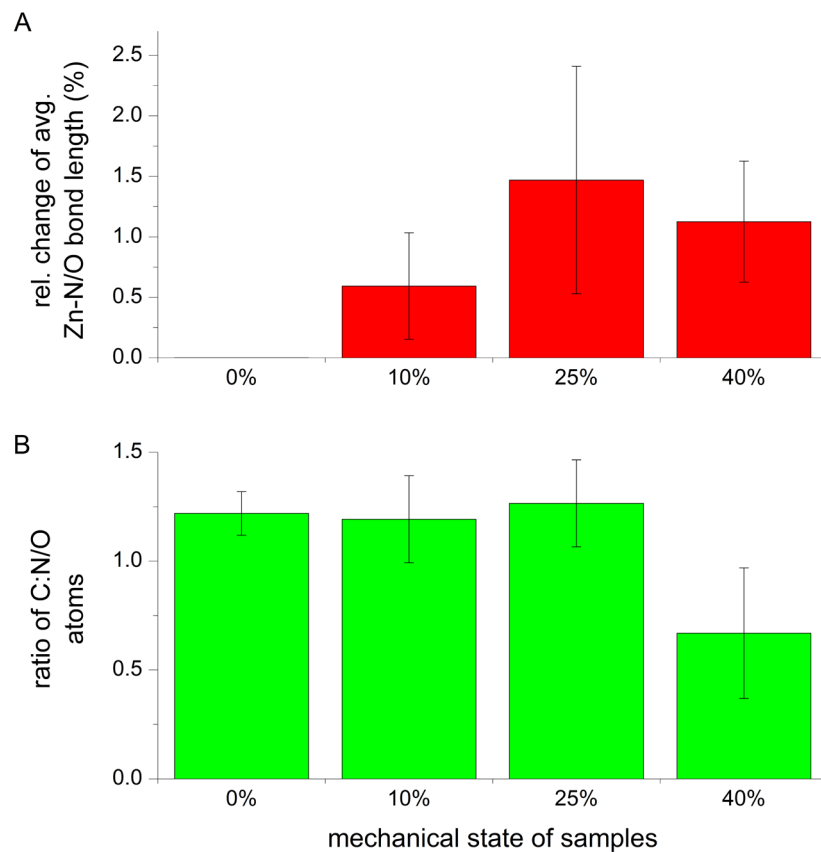


Figure 23 Visualization of EXAFS fitting results for Zn K-edge spectra of *M. californianus* byssal threads prior to and during tensile loading. A) The average strain on 1st shell ligand-Zn bonds. B) The ratio of 2nd shell C atoms to 1st shell N and O metal ligands provides a measure of the relative number of ligands arising from amino acids vs. water. Error bars are uncertainties calculated from the uncertainties of the fit parameters.

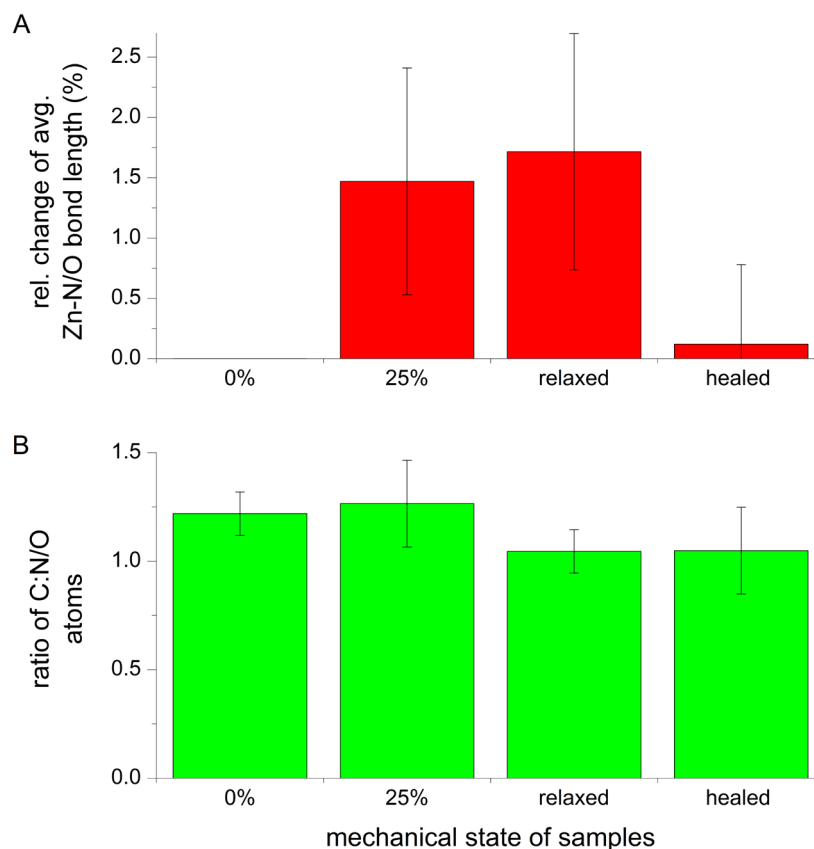


Figure 24 Visualization of EXAFS fitting results for Zn K-edge spectra of *M. californianus* byssal threads prior to and during tensile loading, after relaxation and after healing. Relaxed and healed refer to samples relaxed and healed respectively, after being strained to 25%. **A)** The average strain on 1st shell ligand-Zn bonds. **B)** The ratio of 2nd shell C atoms to 1st shell N and O metal ligands provides a measure of the relative number of ligands arising from amino acids vs. water. Error bars are uncertainties calculated from the uncertainties of the fit parameters.

4.4 DISCUSSION

As outlined in the state of the art section, several previous studies support the existence of His-metal coordination in the core of mussel byssal threads and highlight their possible role as load-bearing sacrificial bonds [33,34,49,60,50]. The ICP-OES and XRF measurements in this study confirm the existence of elevated amounts of Cu and Zn in the core of byssal threads, both of which are known to bind His. Previous measurements on peptides derived from the HRDs from preCols demonstrated the propensity to coordinate transition metal ions as characterized by distinctive peaks in Raman spectroscopy [60]. The Raman spectrum of the core (Figure 18), however, is more complex and had to be deconvoluted by a peak fitting procedure. Peaks were fitted at 1608 cm^{-1} and 1587 cm^{-1} , which possibly correspond to the $\text{N}_\tau\text{-M}$, $\text{N}_\pi\text{-H}$ and $\text{N}_\tau\text{-H}$, $\text{N}_\pi\text{-M}$ metal-bound histidine tautomers, respectively [101]. However, while suggestive, definitive assignments are not possible due to interference from other amino acids including Tyr and Phe in this spectral region.

As mentioned in the results section (Section 4.3.1), the XANES white line intensity confines the average number of first coordination shell Zn-ligands in the byssus core to a number larger than 4 and smaller than 6 [107]. While it was possible to fit the byssal thread Zn-EXAFS by models including 4 and 5 N/O ligands in the first shell (Table 2 and appendix Table 7), fits including 4 ligands required the re-evaluation of the amplitude parameter s_0^2 , previously determined by the fits of the standards, and thus, the most probable coordination number of Zn ions in the byssal thread core is 5. The ratio of second coordination shell C to first coordination shell N/O (Table 3 and Figure 23C), as determined by the EXAFS fitting analysis, is indicative of Zn-coordination primarily by amino acid (AA) ligands rather than by water, which does not add C atoms to the second coordination shell of Zn. Based on the sequence of known thread core proteins (i.e. preCol-NG, preCol-D and TMP-1), possible AA ligands are His, Asp and Glu [34]; however, it is worth noting that analysis of the protein data base (PDB) shows that Zn is 6 times more often observed bound to His than to Asp and Glu taken together [109]. Since the atomic weights of N and O are very close, they are virtually indistinguishable by means of EXAFS fitting analysis, making a definite assignment of the Zn-ligands in the byssus nearly impossible. This is additionally complicated by the fact that XAS measures all Zn coordination sites illuminated by the X-ray beam, providing an average of all coordination structures sampled. Whether the structure fitted by the model represents the exact structure of all Zn ions in the core or only provides an averaged structure representing a mixture of several different possible coordination geometries cannot be distinguished; however, the present results support the hypothesis that Zn ions in the unstretched thread core are coordinated primarily by His residues, with likely contributions from Asp residues as well.

Regardless of the exact coordination in the threads, the observed changes in the bond geometry and ligands occurring during mechanical loading and healing provide important information on the role of metal coordination in byssus mechanics. The shift in edge position (Figure 20) upon stretching of threads implies changes in the total effective charge of the absorbing Zn atoms. These shifts could be due to the change of bond lengths induced by

thread strain, or the exchange of ligands. However, from the current data and knowledge of the system, it is not possible to deduce more information from this observation. Several trends have emerged from the EXAFS fitting models of the stretched, relaxed and healed threads, which taken in light of previous measurements help illuminate the role of metal ion cross-linking in the mechanisms of thread deformation and healing [33,49]. For example, the observation that the sole difference in the EXAFS fitting of the unstrained and 10% strained threads is an increase of the average bond length (Figure 23) limited to the group of short Zn-N/O bonds (Figure 22B) suggests an initial elastic response of AA-Zn bonds to tensile deformation, which is consistent with previous mechanical observations [34,49]. These observations implicate a load-bearing role of His-Zn bonds in the material and therefore, a contribution of these cross-links to the initial thread stiffness. At the other extreme, the sharp drop in second shell C atoms at 40% thread strain (Figure 23B) implies the loss of AA Zn-ligands, which are replaced by H₂O atoms and further supports the view that these load-bearing AA-Zn bonds are sacrificial cross-links that, in fact, rupture during the yield plateau, releasing hidden length and dissipating energy.

Threads stretched to 25% strain fall in the middle of the yield plateau, in which previous results showed an intermediate level of stiffness loss [34] and SAXS studies observed a mixture of folded and unfolded extendable domains [49]. Thus, the EXAFS data are likely to represent a mixture of ruptured and intact AA-Zn bonds. At 25% strain, the length and portion of longer first shell bonds (N/O_{long} in Table 2, Figure 23B) increases, while strain on the shorter first shell bonds (N/O_{short} in Table 2) decreases. The shortening of the Zn- N/O_{short} bonds may suggest the relaxation of previously strained bonds of the short group, due to AA-Zn bond rupture, whereas the increase of Zn- N/O_{long} bond length and portion of N/O_{long} may be due to the further elastic stretching of bonds or alternatively, the breaking of strained bonds and the subsequent re-formation of longer bonds with other nearby AA ligands (Figure 25). However, the fact that bond lengths are not recovered in relaxed threads following removal of load (Figure 22 and Figure 24) supports the hypothesis that the increased length of Zn- N/O_{long} bonds at 25% strain does not arise from elastic stretching of bonds, but rather from bond exchange following rupture of AA-Zn bonds. Such a slip-stick mechanism, in which AA-Zn bonds immediately re-form bonds with new AA ligands following rupture, also seems very likely if the protein chains are not highly extended (in contrast to 40% strain) and is supported by the results of a simulation study on the mechanical behavior of polymer chains containing sacrificial bonding sites [110]. This interpretation is consistent with the aforementioned mixture of folded and unfolded extensible domains and the assumption that sacrificial His-metal bonds must break before the extensible domains can unfold [49].

The study on the self-healing capability of the distal byssal threads was carried out on samples previously loaded to 25% strain and relaxed, and samples which had time to heal for 5 days after being loaded to 25% strain. Interestingly, in spite of removing the load, the average bond length remains higher than in the native state, and the ratio of long to short first shell Zn-N/O bonds remains at a higher than native level. This indicates Zn-AA bonds

remaining in a state similar to 25% thread strain upon thread relaxation, and thus, further supports that the changes in the Zn-coordination environment at 25% thread strain (i.e. bond rupture and ligand exchange) are irreversible on short time scales (i.e. minutes). After healing for five days, the C:N/O ratio stays at the level of the relaxed state; however, the ratio of long to short Zn-N/O bonds decreases over time and the average bond length is lowered close to the initial level in the native unstrained threads. The healing process, therefore, cannot simply be the re-formation of AA-Zn coordination bonds, as proposed previously, but rather must involve the reorganization process of the complex unfolded (denatured) extensible preCol domains and the strengthening of AA-Zn bonds due to a reduction of their bond lengths over time.

Based on *in situ* SAXS measurements performed during cyclic mechanical deformation, Krauss et al. [49] previously proposed that upon relaxation of strained byssal threads, two processes set in – namely, a fast elastic recovery of structural order and a slow recovery of mechanical properties. The former was attributed to the rapid refolding of protein secondary structure, while the latter was ascribed to the slower re-formation of broken sacrificial bonds.[49] The results of XAS in the present study indicate that AA-Zn bonds are present immediately following thread unloading and thus, that the mere re-formation of sacrificial bonds is not sufficient for self-healing. Rather, the recovery of mechanical properties is correlated with a global decrease in the length of the sacrificial AA-Zn bonds over time – possibly, mediated via ligand interchange. In a recent computer simulation study, Nabavi et al. showed that increased backbone vibrations lead to an increase in sacrificial bond length and a decrease in effective bond strength with the bonds sometimes spontaneously rupturing before load was even applied [111] – an effect that could be countered through proper bond topologies (i.e. backbone structure and bond pairing) [110]. This is consistent with single molecule force spectroscopy experiments on small protein domains, which showed that the unfolding force strongly depends on the location of an engineered His-metal bond within the protein fold [112]. These effects of sacrificial bond topology very likely play an important role for the strengthening of sacrificial bonds in the extensible preCol domains as well. This may occur, for example, via factors such as backbone conformation [113,114], bond pairing [110,111], as well as secondary ligand interactions (e.g. hydrogen bonding of primary ligands by other AA [115,116]).

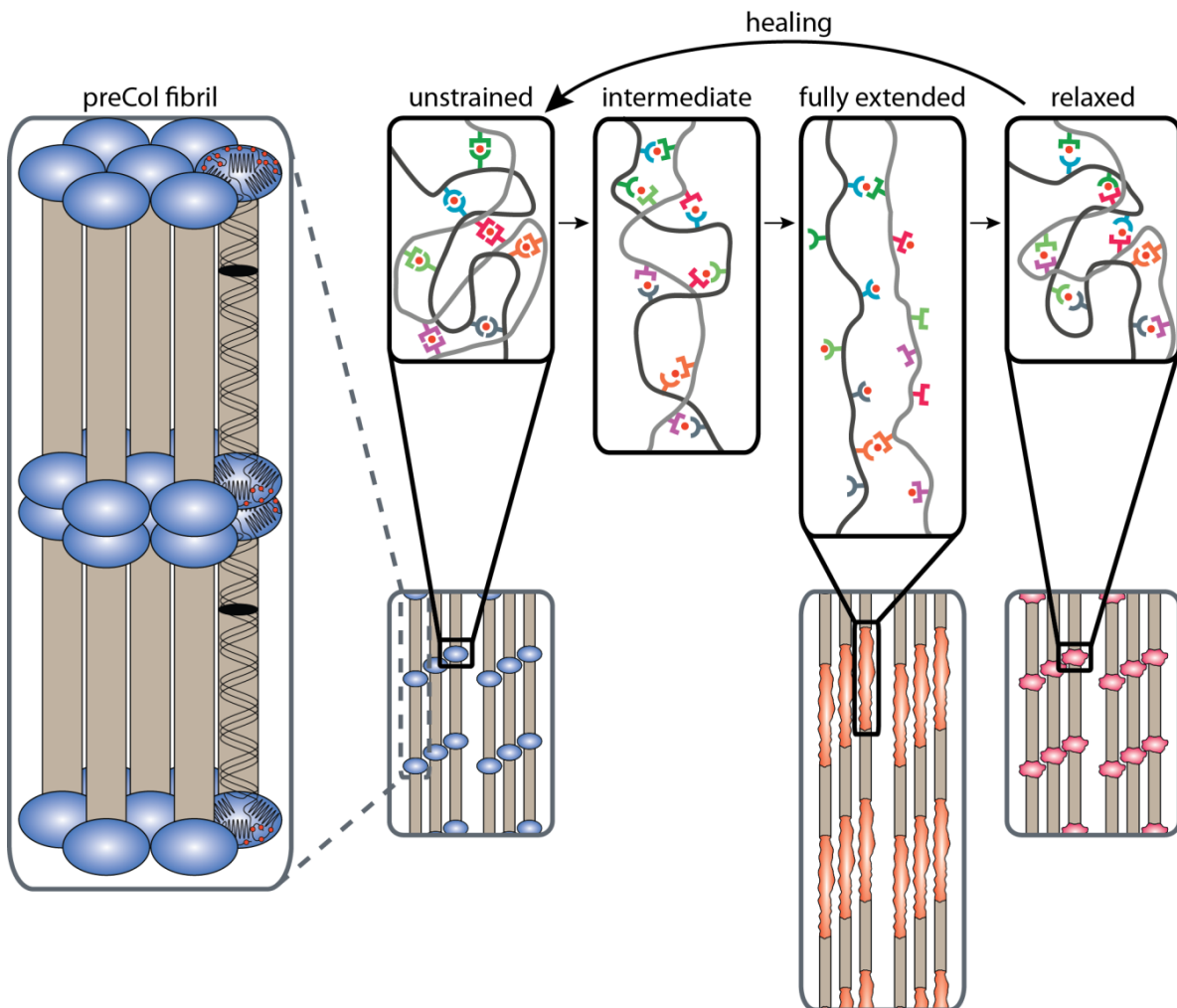


Figure 25 Model of the events taking place during tensile deformation, relaxing and healing of byssal threads, as derived from the combination of XAS results and the current knowledge of the system. The model of the events on the scale of sacrificial bonds (black boxes) is compared to the previously published model of events on the scale of higher order structure (grey boxes) [49]. The unstrained state probably represents the most stable thermodynamic minimum in the folding energy landscape of the extensible preCol domains. The initial sacrificial bond topology is stabilizing this state. At intermediate thread strains, neighboring peptide chains are likely still entangled to some extent. Some of the sacrificial bonds have broken due to excessive bond strains, but the ligands have reformed bonds with other partners while sliding along the entangled chains (slip-stick mechanism). This breaking and reforming of sacrificial bonds is continued until, in the fully extended state, only some of the bonds can reform cross-links, while others are hindered from this and the missing AA-ligands are replaced by water. Upon relaxation of threads, cross-linking bonds are recovered as AA-ligand sites slide past each other (slip-stick mechanism). However, the resulting bond topology differs from the native state. Assuming that the native state represents a most stable thermodynamic minimum in the folding energy landscape, the bond topology in relaxed threads is in a non-equilibrium condition. Thus, the sacrificial bonds break and reform, which spontaneously moves the system towards the native thermodynamic minimum of the unstrained state over time.

Based on these considerations, a new model is proposed here to describe the molecular mechanism of self-healing in mussel byssal threads (Figure 25). Upon removal of load from a strained thread, the elastic framework recoils back to the original length [49] and simultaneously, the unfolded (denatured) extensible preCol domains will begin to explore the protein folding energy landscape [117]. The flanking domains are known to consist primarily of β -sheet conformation [55,118,34], which should refold on the order of nanoseconds to milliseconds [56–58], and therefore, could potentially drive the fast elastic recovery of structural order. However, at the onset of the healing process, sacrificial metal bonds are longer than in their native state and sacrificial bond topology presumably remains compromised and thus, less effective at resisting load. Assuming that the native state represents a most stable thermodynamic minimum in the folding energy landscape, the bond topology in relaxed threads is in a non-equilibrium condition, which spontaneously moves towards this minimum over time. As suggested by the decrease of the ratio of long to short Zn-N/O bonds in the healed threads as compared to the relaxed threads, this most likely occurs via interchange of metal bonds from weak topologies to stronger ones. In this non-equilibrium state, the weaker, longer bonds are more likely to break spontaneously with the possibility to re-form again in an energetically more favorable topology. Over time, the presumed collective effect of numerous breaking and re-forming interchanges is the progressive formation of shorter, stronger bonds. The end result is a slow, thermodynamically driven self-healing process that relies on the inherent lability and dynamicity of AA-Zn bonds and the possibility to tune the thermodynamic and kinetic properties of the bond via topology.

5 CUTICLE

5.1 AIMS OF THIS STUDY

Recent studies have indicated that DOPA-Fe complexes play a crucial role in the mechanics of the byssus cuticle [30,31]. With the reports of large variations of metal concentrations in the byssus depending on the site of collection [38–41], the question arises whether a correlation between the mechanical performance of the cuticle and the specific metals present exists. The focus of this study is therefore on two particular questions: To what extent do DOPA-metal coordination bonds contribute to the mechanical properties of the cuticle? And is there a mechanical effect, if metals besides Fe are integrated into the cuticle via DOPA-binding? Answering these questions will have important implications for mussel ecology and evolution, as well for the design of mussel-inspired metallopolymers [119,120].

In the present study, ICP-OES was used to monitor the concentrations of metals within the distal byssal threads in the native and metal depleted state, as well as in threads treated with different metal solutions. At the same time, the concentration of DOPA was monitored by amino acid analysis. Resonance Raman microspectroscopy was applied to assess and localize the interaction of DOPA with the different metals. Finally, the effects of metal removal and incorporation of different metals into the cuticle on the hardness and stiffness of the cuticle were assessed by nanoindentation. The results provide important insights into the opportunistic and possibly adaptive use of various metal ions by the mussel to fortify mechanical structures.

5.2 EXPERIMENTAL PROCEDURES

5.2.1 Sample Preparation

A total of 144 distal thread parts from the same tank and collection date were split into 3 batches of 48 threads each (Figure 26). Each batch of threads was treated separately for the sake of repetition of measurements. 12 threads of each batch were left untreated (native). The remaining 36 threads of each batch were first stirred for 1 day in citrate buffer at pH 3.86. Afterwards, EDTA treatment was done for 3 days with exchanging EDTA solution every day. The solution consisted of 200mM EDTA and 10mM TRIS-buffer with a pH of 4.34. The threads were washed (stirred) in a 0.1 mM EDTA solution 2 times for 1h each after the last EDTA treatment. 12 threads treated in this way were stored in 0.1 mM EDTA until measurement. The remaining 24 threads were again split into 2 groups of 12 threads. One group was incubated in a 1mM FeCl₃ solution and the other in a 1mM VCl₃ solution for 1h (stirred). The pH of FeCl₃ solution was 2.33, pH of the VCl₃ solution was 2.53. After metal treatment, threads were washed (stirred) in Millipore H₂O 2 times for 1h. The 12 threads from each of the 4 treatment groups of a batch were then each cut into 3 parts. 2 of these parts, each from a different thread, were picked randomly for the nano indentation measurements. This was done to make sure that not always the same region of threads was used for one measurement; however all were from the distal region. A small part of each indentation sample was cut off for Raman measurements. The remaining parts of each thread were split into two groups of 17 pieces for ICP and AAA measurements (Figure 26).

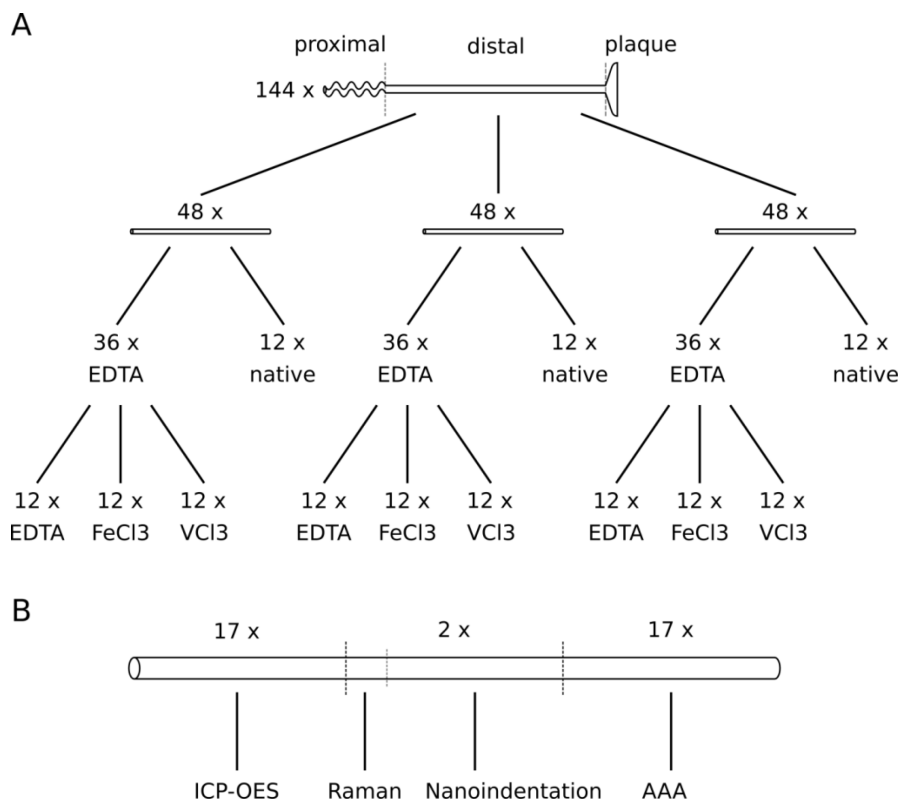


Figure 26 Schematic representation of (A) the grouping of samples used in the cuticle study, and (B) how individual threads were split for the different measurements. Dotted lines represent the points where cuts were made.

5.2.2 Inductively Coupled Plasma - Optical Emission Spectrometry (ICP-OES)

After general sample preparation described above, samples for ICP-OES were freeze dried and then weighed. Subsequently, they were dissolved in 500 μ l aqua regia (167 μ l HNO₃ + 333 μ l HCl) at 40°C for 24h. The resulting solutions were diluted at a 1:10 ratio with Millipore H₂O and emission spectra were recorded with an ICP-OES analyzer (Optima 8000, Perkin-Elmer). A concentric glass nebulizer (type A, Meinhard, Golden, CO, USA) equipped with a glass cyclonic spray chamber (Meinhard, Golden, CO, USA) was used, together with an Argon plasma torch, to atomize the sample solutions. The setup uses a dual échelle polychromator in combination with a CCD detector, as described above, to record sample spectra. Standard solutions, containing the elements in question at a number of different concentrations, were measured to obtain the correlation of element concentration and intensity of spectral lines. Analysis was done with the devices measurement software WinLab32 for ICP-OES.

5.2.3 Amino Acid Analysis

The samples for amino acid analysis were prepared as described above in section 5.2.1. The thread samples were hydrolyzed for 24h in vacuo at 110 °C in 6M HCl with 10% phenol. An Amino Acid Analyzer S433 (Sykam, Eresing, Germany) was used to determine the amino acid composition by ion-exchange chromatography coupled with post-column derivatization of amino acids with ninhydrin. Calibration was performed with a number of differently concentrated amino acid standards containing DOPA and all amino acids except Trp, Asn and Gln. The peaks of the chromatogram were assigned to the individual amino acids based on elution time. From the different areas under each peak at the various standard concentrations, a linear function of area to concentration was extracted. This function was used to determine the amino acid concentrations of the thread samples.

5.2.4 Raman Spectroscopy

Spectra were acquired with a Confocal Raman Microscope (CRM200, WITec, Germany) equipped with a piezo-scanner (P-500, Physik Instrumente, Karlsruhe, Germany). The diode-pumped near infra-red (NIR) laser ($\lambda = 785$ nm, Toptica Photonics AG, Graefelfing, Germany) was focused on the sample through a 60x water immersed objective (Nikon, NA = 1.0). The laser power on sample was set to 15mW. The spectra were acquired using an air-cooled CCD (DU401A-DR-DD, Andor, Belfast, North Ireland) behind a 300gmm⁻¹ grating spectrograph (Acton, Princeton Instruments Inc., Trenton, NJ, USA) with a spectral resolution of 6 cm⁻¹. The lateral spatial resolution of the setup is calculated to 479nm using the simplified Rayleigh criterion

$$r = 0.61 \frac{\lambda}{NA} \quad (30)$$

with numerical aperture NA and excitation laser wavelength λ .

The ScanCtrlSpectroscopyPlus software (Version 1.38, WITec, Ulm, Germany) was used for measurement setup. The cut cuticle surface was localized using the “fast image” option of the software. After localization of the cuticle, 2D spectral images were acquired.

Additionally, at least 5 single measurements were taken from different regions within the cuticle area and averaged. Spectra were exported from ScanCtrlSpectroscopyPlus software and the OPUS software package version 7.0 (Bruker Optik GmbH) was used to subtract a polynomial background and normalize spectra to the area under the aliphatic CH peak (2850 – 3010 cm^{-1}).

5.2.5 Nanoindentation

Samples for nano-indentation were embedded in Epofix, after the general sample preparation described above, and cured overnight. An ultra-microtome (PowerTome XL, RMC Products) was used to obtain smooth transverse cross-section surfaces.

All indentation experiments were carried out according to the protocol previously established by Holten-Andersen et al. [46]. During measurements, the samples were fully submerged in either Millipore H_2O or 0.1mM EDTA. Testing was performed on a TriboScan UBI-1 (Hysitron, Minneapolis, MN, USA) equipped with a Berkovich tip. The location of each indent was chosen after obtaining an image of the sample surface via scanning probe microscopy (SPM). 60 to 90 indents of the cuticle were performed per sample. Two different threads per sample treatment were tested. All indentations were performed in the open loop mode and the loading and unloading rate was 100 $\mu\text{N/s}$. The peak load of about $\sim 1000\mu\text{N}$ was held for 30s to eliminate creep effects. A PMMA standard was used to obtain the tip area function. Hardness and reduced elastic modulus were obtained with the method described above by Oliver and Pharr [95], using the TriboScan measurement software (Hysitron, Minneapolis, MN, USA).

The obtained values of hardness and elastic modulus were statistically analyzed with the R software for statistical computing [121], using the libraries *Rcmdr* [122] and *pgirmess* [123]. The applied statistical testing procedures were the Shapiro-Wilk test for normality of distribution within single samples and treatment groups, Wilcoxon-Mann-Whitney test for comparing samples of the same treatment group, Levene's test for homogeneity of variance between treatment groups, the Kruskal-Wallis rank sum test for analysis of variance of treatment groups with *post-hoc* multiple comparisons according to Siegel and Castellan [124] with Dunn-Šidák correction for analysis of specific pairs of treatment groups for significant differences. The Wilcoxon-Mann-Whitney test and the Kruskal-Wallis rank sum test were applied, since not all distributions passed the Shapiro-Wilk test, and Levene's test rejected homoscedasticity between treatment groups.

5.3 RESULTS

5.3.1 Inductively Coupled Plasma - Optical Emission Spectrometry (ICP-OES)

ICP-OES was performed to track the amount of metals in native threads, threads treated with EDTA and threads treated with EDTA, which were subsequently soaked in aqueous solutions of FeCl_3 and VCl_3 . First the native threads were screened for metals with the ability to form tris-DOPA complexes [125]. Figure 27 shows the results of this first screening. Based on these results, the following ICP-OES measurements were limited to the detection of Ca, Fe and V. Figure 28 shows the levels of these metals in the native and EDTA-treated samples. In native samples iron and vanadium had a concentration of $0.91 \pm 0.25 \mu\text{mol/g}$ and $0.58 \pm 0.10 \mu\text{mol/g}$ of thread, respectively. Calcium was present at a level of $2.05 \pm 0.03 \mu\text{mol/g}$. EDTA treatment substantially lowered the concentrations of iron and vanadium to $0.33 \pm 0.10 \mu\text{mol/g}$ and $0.04 \pm 0.01 \mu\text{mol/g}$, while calcium was only reduced to $1.64 \pm 0.03 \mu\text{mol/g}$. Figure 29 compares the metal concentrations of metal recovery samples, with the concentrations in the native and EDTA-treated state. Treatment with FeCl_3 and VCl_3 resulted in increased levels of iron $3.14 \pm 0.36 \mu\text{mol/g}$ and vanadium $7.44 \pm 2.00 \mu\text{mol/g}$. The concentrations of metals, which were not present in the metal recovery solutions, stayed at the levels of EDTA treatment. It has to be noted that the measurement of calcium concentrations was only performed on one sample per treatment, while the concentrations of other metals were measured for 3 to 5 samples per treatment.

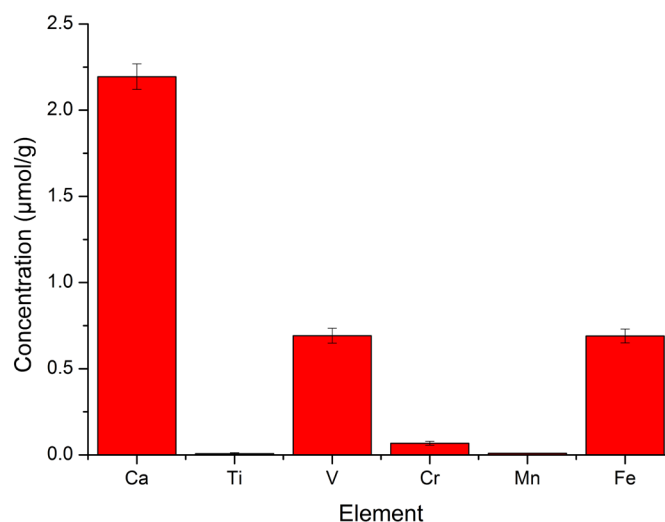


Figure 27 ICP-OES screening of *M. californianus* byssal threads for metals with known ability to form tris-DOPA-metal complexes. Error bars are standard deviations from 2 samples each measured 6 times.

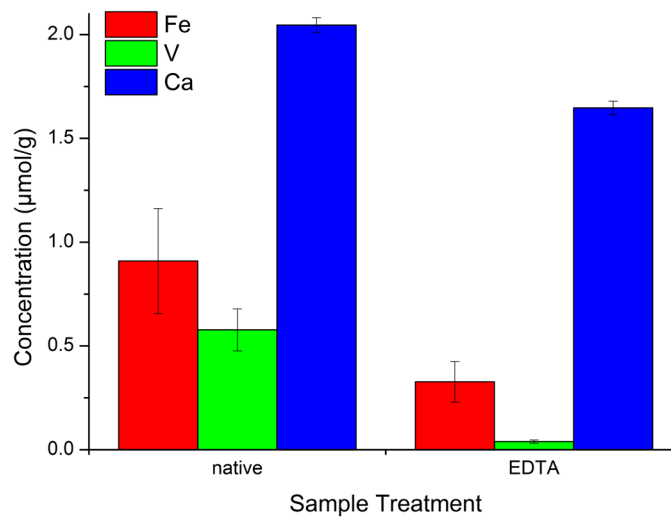


Figure 28 Concentrations of iron (Fe), vanadium (V) and calcium (Ca) in native threads and threads treated with EDTA. Values of Fe and V are the means of 5 measurements. Ca values are means of 2 measurements. The error bars are standard deviations.

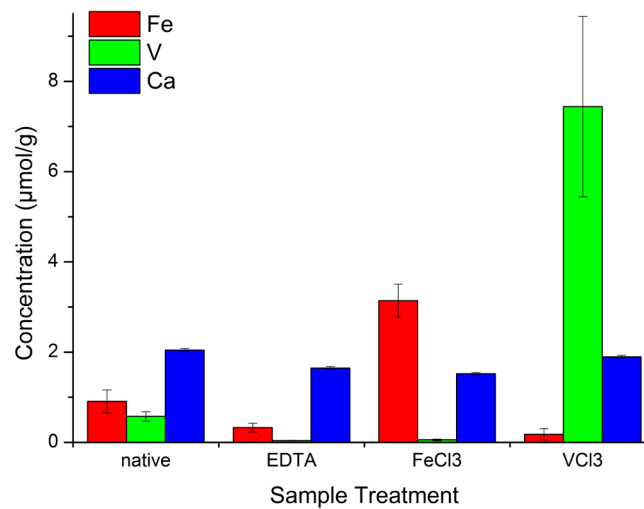


Figure 29 Concentrations of iron (Fe), vanadium (V) and calcium (Ca) in native threads, threads treated with EDTA and EDTA treated threads subsequently soaked in a FeCl_3 or VCl_3 solution. Values of Fe and V are the means of 5 measurements. Ca values are means of 2 measurements. The error bars are standard deviations.

5.3.2 Amino Acid Analysis

Amino acid analysis was conducted in order to obtain the concentration of DOPA in the distal portion of byssal threads. Figure 30 shows an elution profile detected at a wavelength of 570nm of a distal byssal thread sample.

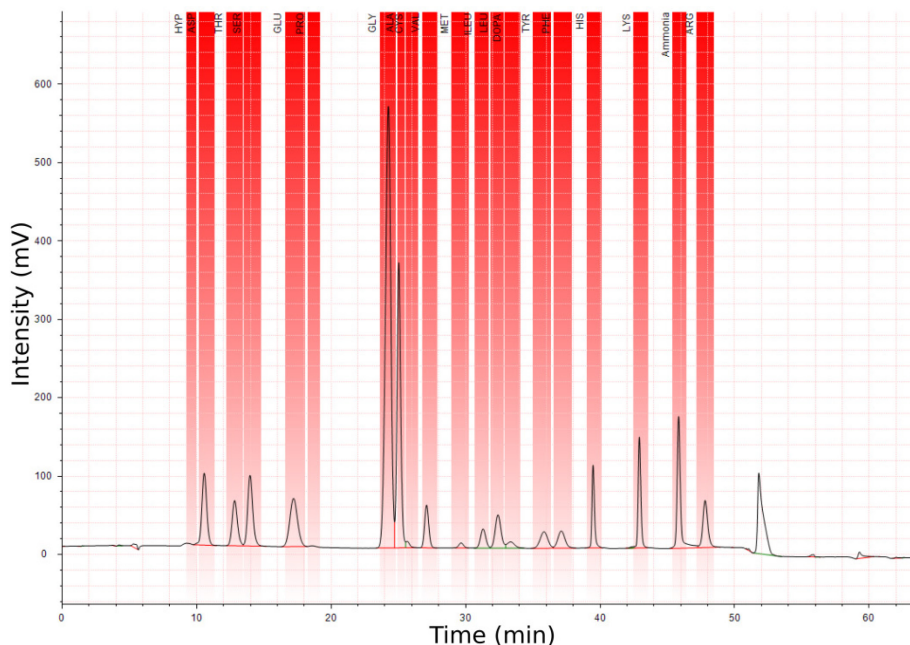


Figure 30 Amino acid analysis elution profile of the distal portion of byssal threads from the species *M. californianus*, collected at a wavelength of 570nm. The amino acids are separated by elution time, so each peak corresponds to the elution of one kind of amino acid. The integral is calculated by subtracting a straight line background (red line) from each individual peak. Peak overlaps are separated by a straight vertical line. To distinguish between Hyp and Pro data was simultaneously collected at a wavelength of 440nm (elution profile not shown).

It was not possible to measure the amino acid composition of only one piece of a distal portion of a byssal thread. To obtain enough signal, it was necessary to use several pieces of thread for one measurement as described in section 5.2.1. Therefore, the results of all measurements were averaged and are compared to published amino acid compositions (from [59,53]) of closely related mussel species in Table 4. The relative concentration of DOPA, in the distal portion of *M. californianus* byssal threads, was found to be $0.82 \pm 0.16\text{mol}\%$ (mean \pm SD), resulting in an absolute concentration of $78 \pm 18\mu\text{mol/g}$ of thread sample.

Table 4 Amino acid composition of distal thread portions of *M. californianus* compared to *M. galloprovincialis* and *M. edulis*.

Interspecies Comparison of Amino Acid Composition of Distal Threads					
Amino Acid	<i>M. californianus</i>		<i>M. galloprovincialis</i> [53,59]	<i>M. edulis</i> [59]	
	Absolute Concentration [$\mu\text{mol/g}$]	Relative Concentration [mol %]	Relative Concentration [mol %]	Relative Concentration [mol %]	Relative Concentration [mol %]
ASX	482 \pm 87	5.07 \pm 0.15	4.67	7.2	5.17
THR	332 \pm 60	3.49 \pm 0.10	2.57	2.8	3.09
SER	461 \pm 81	4.86 \pm 0.10	4.50	6.1	4.75
GLX	496 \pm 89	5.22 \pm 0.15	5.16	4.4	5.21
GLY	3167 \pm 562	33.34 \pm 0.77	34.04	28	34.17
ALA	1407 \pm 267	14.79 \pm 0.57	19.58	16.8	16.21
CYS	20 \pm 7	0.22 \pm 0.08	0.09	0.2	0.13
VAL	272 \pm 54	2.85 \pm 0.22	2.58	3.3	2.44
MET	45 \pm 11	0.47 \pm 0.06	0.56	0.0	0.63
ILE	160 \pm 33	1.68 \pm 0.16	1.06	1.4	1.01
LEU	205 \pm 37	2.16 \pm 0.06	2.39	2.1	2.91
DOPA	78 \pm 18	0.83 \pm 0.16	0.30	1.5	0.18
TYR	176 \pm 34	1.85 \pm 0.08	1.37	2.1	1.50
PHE	166 \pm 29	1.75 \pm 0.06	1.09	1.1	1.09
HIS	311 \pm 61	3.27 \pm 0.20	2.64	1.0	2.19
LYS	373 \pm 64	3.94 \pm 0.11	3.19	3.9	3.76
ARG	333 \pm 58	3.52 \pm 0.22	3.39	2.8	2.00
HYP	561 \pm 101	5.91 \pm 0.27	4.03	8.2	5.80
PRO	457 \pm 84	4.80 \pm 0.13	6.80	4.9	7.74

Amino acids are listed by elution time. Values represent the average of 2 measurements of 11 samples \pm standard deviation. Relative concentrations do not add up to 100 due to rounding of average values. The unit of mol% refers to residues per 100 residues. The absolute concentration unit is μmol of amino acid per g of thread. ASX and GLX refers to Asp and Asn, and Glu and Gln respectively. Values for *M. galloprovincialis* and *M. edulis* are taken from [53,59].

5.3.3 Raman Spectroscopy

Raman spectra of native threads, threads treated with EDTA and threads treated with EDTA, which were subsequently soaked in aqueous solutions of FeCl_3 and VCl_3 , were recorded to detect the interaction of metals with DOPA. Figure 31A shows the averaged spectra of at least 5 measurements per sample. The major peaks, indicated by the vertical lines, are assigned according to [126,30,127,128], and are compared for the different sample treatments in Table 5. Resonance Raman spectra obtained from native thread cuticles are consistent with those previously reported, exhibiting a triad of peaks between $500 - 700 \text{ cm}^{-1}$ corresponding to the oxygen-metal interaction and four peaks between $1150 - 1450 \text{ cm}^{-1}$ corresponding to vibrations in the catechol ring. The treatment with EDTA results in the loss of the resonance signal assigned to metal-DOPA interaction. Depending on the efficacy of the EDTA treatment, remnants of the low energy peaks may be observed, but significantly reduced. Upon treatment with the metal solutions this resonance signal is recovered. However, there are differences in the spectra of the Fe- and V-recovered samples. The resonance peaks between 250 cm^{-1} and 900 cm^{-1} shift to lower wavenumbers for the Fe-treatment compared to the native and V-treated samples. This is also the case for the $\nu \text{ C-O}$ mode peak around 1270 cm^{-1} , which is recovered at a slightly lower 1266 cm^{-1} in the Fe-treated sample. The $\nu \text{ C-C}$ coupled to $\delta \text{ C-H}$ mode peak at 1472 cm^{-1} is shifted to 1480 cm^{-1}

for the Fe-recovery and is recovered at the position of the native sample upon treatment with V.

It was not possible to normalize the intensity of the cuticle spectra relative to one another due to the combined effects of resonance and fluorescence; therefore, 2D-mapping of the cuticle was performed in which it was possible to compare the intensity of the metal-O coordination band of the core to the cuticle (Figure 31B). Relative to the native signal, there is a massive loss in cuticle signal intensity in the EDTA-treated sample such that there is no apparent difference to the core signal intensity. The elevated intensity of the cuticle, relative to the core, is recovered in the Fe-rescue threads; however, the intensity is much lower than observed in the native threads. V-rescue threads on the other hands show a much higher intensity in the cuticle signal relative to the core, when compared to the native state. It is worth emphasizing here that absolute intensity levels between Fe- and V-rescue threads do not provide quantitative information about the relative amount of cross-linking because resonance intensity is highly dependent on the incident laser wavelength and the absorption maxima of the respective metal complex. Nonetheless, these data confirm that both, Fe and V, are capable of DOPA coordination localized in the byssus cuticle.

Table 5 Assignments of observed Raman shifts and comparison with literature values. All values represent wavenumbers in cm^{-1} .

native ^a	native ^b	Fe-recovery ^a	V-recovery ^a	assignment ^{b,c,d,e}
418	415	315	418	ν metal-O
550	550	533	547	δ, ν -chelate
603	596	586	601	ν metal-O (C_3)
635	637	632	635	ν metal-O (C_4)
824	824	818	824	ring breathing
1270	1270	1266	1271	ν C-O
1321	1322	1321	1321	ν C-C
1421	1423	1422	1423	ν C-C
1472	1476	1480	1472	ν C-C + δ C-H

^a this study; ^b [30]; ^c [126]; ^d [127]; ^e [128]
 ν = stretching; δ = out-of-plane bending

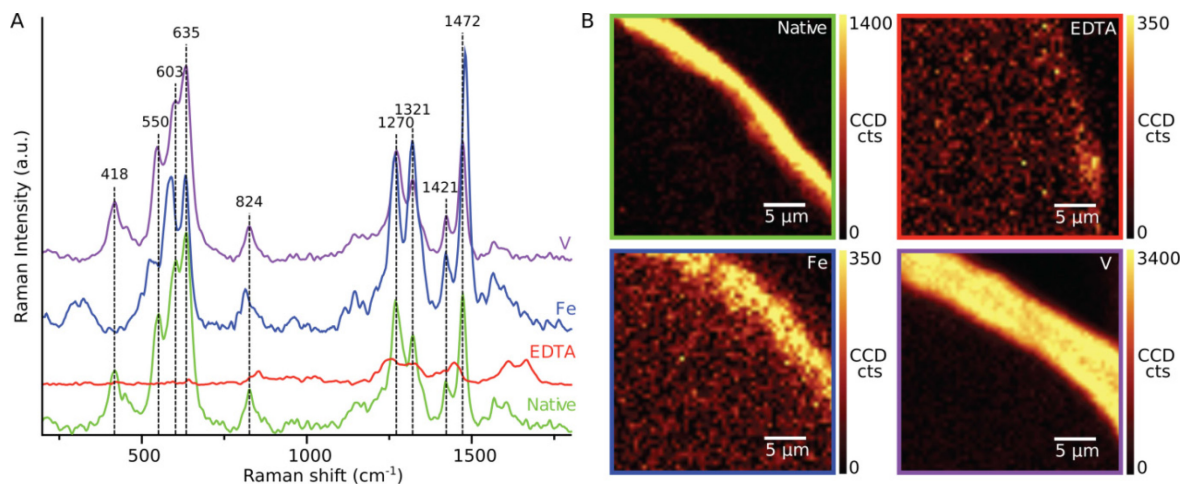


Figure 31 Summary of the Raman investigations on the DOPA-metal interaction of native threads, threads treated with EDTA and EDTA-treated threads subsequently soaked in metal solutions. (A) A comparison of the Raman spectra of the samples described above. All spectra are background corrected but only roughly normalized to the amide I band. The vertical lines indicate the peak positions in the native threads. The resonance signal of metal-DOPA interaction is reduced when metals are removed by EDTA-treatment. Metal recovery leads to recovery of the resonance signal, with the peaks between 250 cm^{-1} and 900 cm^{-1} shifting to lower wavenumbers for the Fe-treatment compared to the native and V-treated samples. (B) 2D Raman images of transverse *M. californianus* thread sections, integrated over the $490 - 696\text{ cm}^{-1}$ wavenumber range. The core intensity provides an internal normalization in this spectral range because it is not expected to be affected by any of the treatments.

5.3.4 Nanoindentation

Nano-indentation was employed in order to investigate the role of metal ions (specifically, Fe and V) in influencing the mechanical properties of the cuticle. Results are summarized in Figure 32 and Figure 33 and Table 6. The cuticles of native samples exhibited reduced elastic modulus (E_r) and hardness (H) values of about 1.2 ± 0.3 and $0.04 \pm 0.01\text{GPa}$, respectively. Metal removal via EDTA treatment resulted in a reduction of E_r and H values of about 85%. The EDTA-treated threads, which were subsequently soaked in metal solutions, exhibited a recovery of E_r to $1.2 \pm 0.2\text{GPa}$ (mean \pm SD) and H to $38 \pm 7\text{MPa}$ (FeCl_3) and $1.1 \pm 0.2\text{GPa}$ and $37 \pm 8\text{MPa}$ (VCl_3). Using the Kruskal-Wallis rank sum test, it was determined that native threads and both FeCl_3 and VCl_3 metal recovery threads exhibited statistically indistinguishable H and E_r values, whereas all three groups were significantly different from the EDTA treated threads (Figure 32). It is worth noting that a Wilcoxon-Mann-Whitney test revealed small, but statistically significant differences (at the $p < 0.02$ level) between threads from each batch containing metal ions; however, the two EDTA treated threads stripped of metals showed identical performance (Figure 33). This has interesting implications for the natural biological variation in thread performance. The mechanical data is correlated to the concentrations of iron and vanadium in Figure 34.

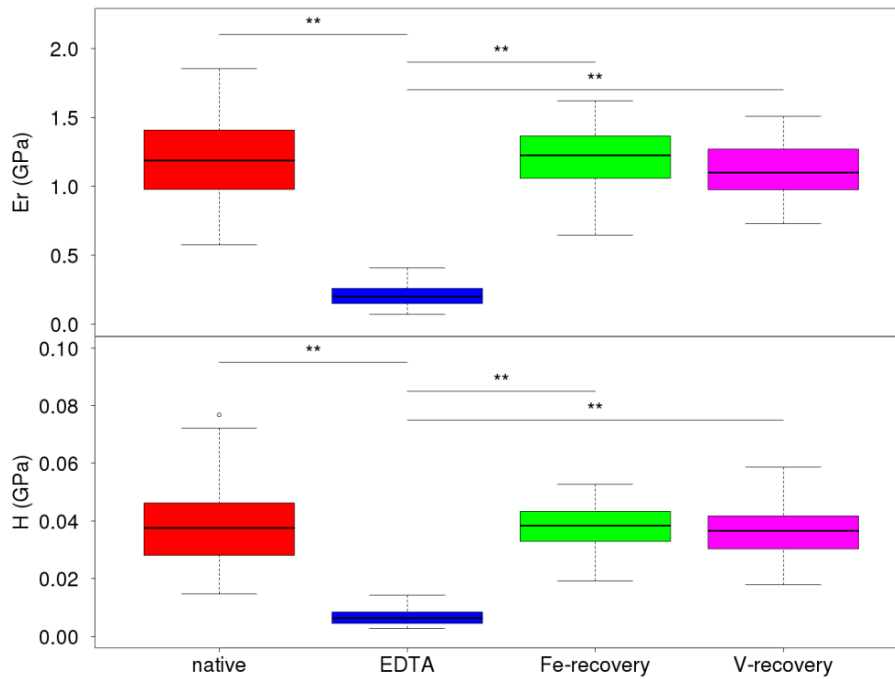


Figure 32 Comparison of measured reduced elastic modulus (E_r) and hardness (H) values. Each boxplot presents the measured distribution of values per treatment group. Lines and stars indicate statistically significant differences at the 0.01 level (Kruskal-Wallis-Test).

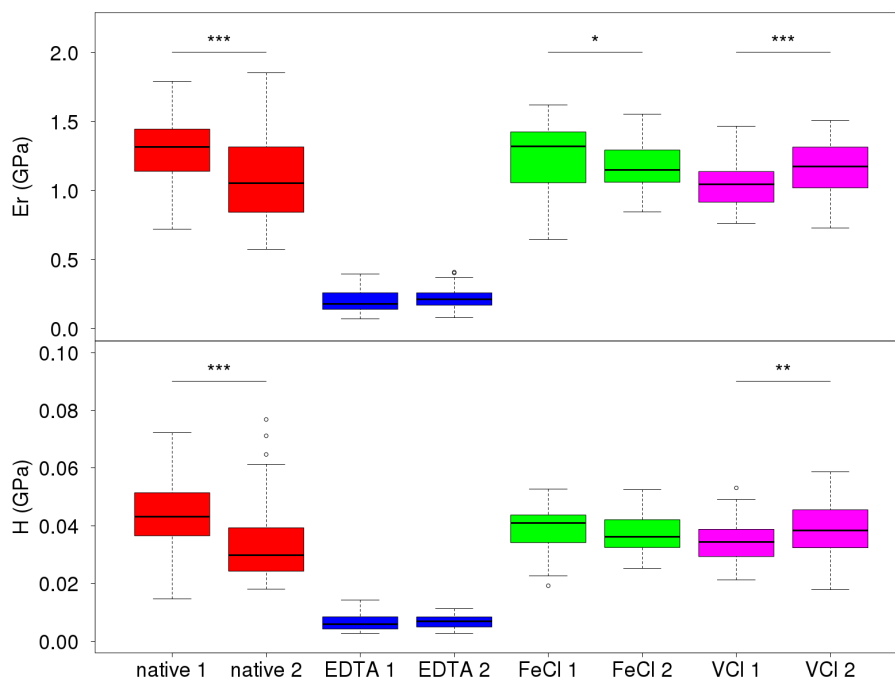


Figure 33 Comparison of measured reduced elastic modulus (E_r) and hardness (H) values. Each boxplot presents the measured distribution of values per sample. Lines and stars indicate statistically significant differences (p-values: ***<0.001, **<0.01, *<0.02; Wilcoxon-Mann-Whitney-Test).

Table 6 Mean values of elastic modulus E_r and hardness H of measurements grouped by treatment.

Sample	N	E_r (GPa)		H (MPa)	
		Mean	SD	Mean	SD
native	148	1.2	0.3	38	13
EDTA	145	0.2	0.1	6	2
FeCl ₃	166	1.2	0.2	38	7
VCl ₃	135	1.1	0.2	37	8

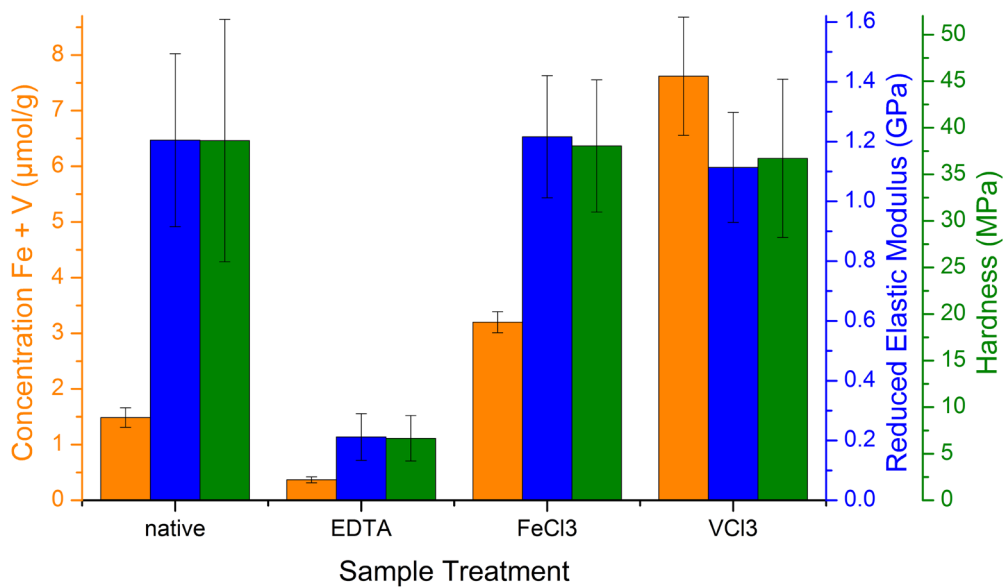


Figure 34 Correlation between the concentration of iron and vanadium and the mechanical performance determined by nanoindentation for native cuticles, cuticles treated with EDTA and EDTA-treated cuticles subsequently soaked in metal solutions. The removal of metals results in a reduction of 85% of the mechanical performance. Even though metals are recovered to higher levels than in the native threads, the mechanical properties are only recovered to the level of the native upon metal recovery treatments. Error bars represent standard deviations of the measurements.

5.4 DISCUSSION

Oil contamination of seawater is known to result in elevated levels of V in mussel tissues, including the byssus [37]. The *M. californianus* mussels, used in this study, were grown in seawater from a region rich in natural oil seeps, and ICP-OES measurements detected elevated amounts of V in their byssal threads (Figure 28). The comparison of the resonance Raman spectra of the native and V-recovered thread cuticles clearly shows the coordination of V by DOPA (Figure 31 and Table 5). While the EDTA treatments resulted in an efficient removal of Fe and V from the byssal threads, the Ca concentration was largely unaffected (Figure 28). Nevertheless, hardness and reduced elastic modulus of the cuticle were reduced by over 80% by EDTA treatment (Figure 32). Both metal recovery treatments, with aqueous solutions of either FeCl_3 or VCl_3 , resulted in the full recovery of the cuticle's native mechanical performance as measured by nanoindentation (Figure 32). No statistical differences in mechanical performance of the two metal recoveries were observed. Interestingly, this suggests that different metals can be used interchangeably as reinforcing cross-link agents in the cuticle of mussel byssal threads.

The interchangeability of V and Fe with respect to the mechanical performance of the byssus cuticle is surprising. In the jaws of the marine worm *Nereis virens*, another biological material based on cross-linking via metal complexes, it was demonstrated that exchanging of metal ions does result in the change the mechanical performance of the material [129]. Both materials, the byssus cuticle and the *Nereis* jaws, depend on the formation of metal complexes for cross-linking. As opposed to the byssus cuticle, in *Nereis* jaws these cross-links are formed by a system of histidine- Zn^{2+} complexes. This could indicate that cross-linking via histidine functions differently than cross-linking via DOPA. However, a study on hydrogels based on cross-linking by DOPA-metal complexes, also demonstrated control over network mechanics by variation of the metal ions present in the material. It was demonstrated that at pH 8, V induces tris-DOPA coordination resulting in a stiffer material when compared to the bis-DOPA-Fe based hydrogel, which formed at the same pH resulting in an altered mechanical performance.[120] This is contrary to the apparent indifference of the byssus cuticle, in terms of the mechanical behavior, to the type of metal ion present in the DOPA-metal complex. Furthermore, the chemistry of V in seawater is rather complex, and it can exist in many dissolved and particulate forms [130,131]. The form of V present in the DOPA-V complexes is likely to influence the stability of the complex. With this variability of metal complex stability the question arises what mechanism is stabilizing the properties of DOPA-metal cross-links in order to accomplish stable mechanics in the byssus cuticle, using different metal ions.

The reduced elastic modulus (E_r) of a non-rigid polymeric material strongly depends on the degree of cross-linking within the material [132]. Therefore, the identical values of E_r in the native and metal-recovered states indicate a stable degree of cross-linking in the cuticle before and after exchange of the metal ions. The number of possible cross-links in the cuticle depends on the number of DOPA residues and the amount of metal ions capable of DOPA-metal complex formation. Assuming bis- or tris-DOPA-metal coordination in the native

cuticle, the expected ratio of DOPA to metal would be 2:1 or 3:1. Yet, the DOPA and metal concentrations observed in this study indicate a 50:1 ratio of DOPA to metals (V plus Fe) in the native state. The metal recovery samples show higher metal concentrations than in the native threads. This results in a decrease of the DOPA to metal ratio from 50:1 in the native case to 25:1 in the case of iron recovery and 10:1 for the vanadium recovery. Since other metals with known ability to form stable tris-DOPA-metal complexes were not detected at significant amounts in the byssal threads (Figure 27), the nanoindentation measurements of the native and metal recovery samples show that the presence of Fe or V is sufficient to fulfill the role of metal ion cross-linker. Furthermore, the excess metal, which is taken up in the metal recovery experiments, does not lead to an increase of reduced elastic modulus and hardness. This indicates, that while the excess metal could (and probably does) bind to DOPA residues, these DOPA residues are not capable of forming additional cross-links in the material. Therefore, there seem to be two populations of DOPA residues in the thread cuticle. One population is able to participate in the cross-linking via formation of bis- and tris-DOPA-metal complexes, while the other is limited to the formation of the mono-complex.

One possible mechanism for this separation of DOPA populations is spatial separation and steric hindrance, due to secondary protein conformation within the thread cuticle. While initially believed to be unstructured, recent evidence using circular dichroism (CD) spectroscopy has demonstrated that MFP-1 possesses a notable degree of polyproline II (PPII) structure, which is an extended protein conformation similar to that observed in a single chain of a collagen triple helix [63]. Another mechanism by which the species of the formed metal-DOPA complex can be influenced is the control of the local pH. While at low pH the formation of the mono-Dopa-metal complex is favored, this shifts to the bis- and finally the tris-DOPA-metal complex with rising pH.[125] This pH dependence has been shown to lead to different mechanics of hydrogels, depending on the species of DOPA-metal cross-linking [25]. Control over the local pH is widely known from the active sites of enzymes, where distinct structuring and shielding of substrate binding pockets from the environment is often used to create a specific pH. Possibly the same strategy applies to the DOPA-metal cross-linking sites within the protein structure of the cuticle.

As previously described, the cuticle is produced by a seemingly coarse secretion process. The details of this process are not well investigated; however, it is known that during the secretion, the proteins undergo a pH shift from about 4 - 5.5 within the ventral foot groove to approximately 8 in the seawater [67,133]. The pH does not only control the species of the formed metal-DOPA complex, it has also been shown that the pH regulates the metal-mediated formation of covalent catechol cross-links in PEG-based hydrogels [134], and a similar mechanism has been suggested to contribute to the curing of the byssus adhesive plaque [135]. At low pH values the reduction of Fe^{3+} to Fe^{2+} leads to the creation of o-quinones and their subsequent reaction to covalent catechol-catechol bonds, whereas increasing the pH favors the Fe^{3+} -catechol coordination bonds. In the production of the mussel byssal threads, this pH dependence is suggested to form covalent diDOPA cross-links

during the time the thread spends in the ventral foot groove.[134,67] Covalent cross-linking, prior to the formation of DOPA-metal complexes at higher pH values, may fix the structural arrangement of MFP-1 within the cuticle, and therefore predetermine which DOPA residues can take part in the formation of bis- and tris-DOPA-metal complexes and which ones are limited to the mono-DOPA-complex. In this model of thread cross-linking, the time the threads spend in the ventral foot groove determines the degree of covalent cross-linking in the thread cuticle. The covalent cross-linking provides the cuticle with some initial stiffness, which is then enhanced by the DOPA-metal cross-links – in the present case by nearly an order of magnitude increase in hardness and stiffness. In a previous study the removal of metals resulted in an only 50% reduction of the cuticle hardness [31]. This smaller decrease in residual hardness following metal removal could be due to differences in the degree of covalent cross-linking as predetermined by the thread formation process. Along these lines, the native properties of the threads in this previous study were higher than measured in the present study [31]. The single difference in the conditions of metal removal between the present study and the previously mentioned was a somewhat higher pH of 5.5 in the latter. Interestingly, this was accompanied by a complete removal of Ca, as opposed to this study where Ca was largely unaffected by the EDTA-treatment. However, the recovery of native Ca levels was not necessary in this study to recover native mechanics. From the current knowledge, the role of Ca in cuticle mechanics remains unanswered and should be the topic of future investigations.

Regardless of the mechanisms responsible, this study clearly shows that a stable mechanical performance of the byssal threads cuticle is not limited to the availability of a single type of metal ion, i.e. Fe. These observations are especially significant when considering the evolutionary fitness of this organism. Mussels are sessile organisms, which reproduce via broadcast spawning. This means that a mussel has little control over the choice of habitat, and once it has settled in a place it has to deal with the present circumstances. Considering the natural variation of metal concentrations in ocean waters, at present and on an evolutionary timescale, the DOPA-metal cross-linking strategy provides a versatile means for the mussel to achieve stable and reliable mechanics in a variety of environments. In other words, the ability of the mussels to utilize various metals without a loss of material performance may well be an adaptation to the unpredictable metal availability.

6 CONCLUSIONS AND OUTLOOK

The present study was focused on protein-metal coordination interactions as a versatile approach for cross-linking and mechanically reinforcing biological materials – employing the mussel byssus as a model material. Biological organisms utilize numerous different cross-linking strategies in order to build mechanically diverse protein-based biological materials, including relatively stiff materials such as silk and tendon, as well as softer materials like whelk egg capsules, elastin or resilin. Within this group of materials, covalent bonds and non-covalent interactions are found to serve different mechanical functions. Covalent bonds provide essentially permanent cross-links with high stability, typically used to reinforce the protein network. Non-covalent interactions (e.g. hydrogen bonds), on the other hand, are transient and weak interactions that provide a flexible and dynamic linkage when isolated, but which can be combined in large numbers to stabilize more complex topologies and secondary structures (e.g. H-bond stabilization of β -sheet structures in silks, or α -helices in keratinous materials) [136,137]. Metal coordination bonds, on the other hand, are a class of chemical interactions with properties that fall in the middle of the spectrum of covalent and non-covalent interactions. They combine high strength with increased lability, making them a unique stable, yet dynamic cross-link. The mechanical properties of materials, however, are not only determined by the type of cross-linking in the material, but are found to depend in a large part on the topology (i.e. combination and arrangement) of the cross-links [111]. Additionally, factors such as protein backbone structure and the hierarchical structuring of a material and its building-blocks are frequently found to play a major role in the determination of the material properties.

The current study uses the mussel byssus as a model system for understanding how metal coordination bonds can be harnessed in biological materials to achieve specific properties. Specifically, the investigations on the thread core explored the hypothesis that His-Zn bonds function as sacrificial bonds in the yield and self-healing behavior of the material. The cuticle study, on the other hand, focused on the contribution of DOPA-metal cross-linking to the mechanical integrity of the hard yet extensible coating, and attempted to understand how tolerant the complex is to variation in metal composition – as can occur in natural environments. The findings of these two projects highlight the importance of the dynamic nature of metal coordination bonds in both cases and perhaps, even provide clues as to why these types of bonds might have been selected for during evolution in the mussel byssus. From a more technological and industrial perspective, the present results may also have implications for the design of mussel mimetic polymers.

The spectroscopic investigation of the fibrous core described in chapter 4 provides strong support for the hypothesis that rupturing load-bearing sacrificial Zn coordination bonds, most likely mediated via His residues in the HRDs, play a vital role in the tensile behavior of threads, including yield and dissipation of mechanical energy during cyclic loading. Furthermore, the findings indicate that the thread healing process, contrary to previously proposed models, is not due simply to the re-formation of broken AA-Zn bonds, but rather involves a higher order reorganization process towards more stable bond topologies. The

inherently labile and dynamic AA-Zn bonds appear to provide the basis for this slow, thermodynamically driven self-healing process, due to their ability to exchange ligand partners until a lower energy state is attained. In light of previous investigations, this study further underlines the importance of the organization of the protein building blocks and their various stabilizing cross-links at multiple length scales to the mechanical behavior of the byssal threads. These findings have potential to improve the current mechanical properties of man-made, self-healing polymers, which will be discussed in the final paragraph.

While the present study provides a more thorough understanding of the mechanisms involved in the tensile deformation and self-healing of byssal threads, many important questions still remain. XAS provided strong evidence for the presence of coordinated Zn ions in the thread core, likely via His ligands; however, their localization at the nano-scale would represent another important milestone in our understanding. One potential approach to resolve this matter would be tip enhanced Raman spectroscopy (TERS). Since previous AFM studies were able to resolve individual preCol domains within the thread core [54], TERS could potentially be able to focus the excitation of Raman spectra to the HRD, which would reduce the occurrence of overlapping bands and provide a means of localizing the metal bonds. Another pending question concerns the (mechanical) role of other metals (e.g. Cu and Ni) detected in the byssal threads, which are capable of binding to His. Possibly, similar to the cuticle, an opportunistic adaptability to the changing availability of ocean metal ions is also maintained in the core. Therefore, XAS experiments focusing on the x-ray absorption edges of these metals could provide additional insights into the working principles of metal-mediated sacrificial bonds. The current XAS experiments suggest the involvement of Asp or Glu in the coordination of Zn; however, the only sufficient source of Asp or (iso)Asp in byssal threads is formed over several days after thread formation by non-enzymatic spontaneous deamidation of TMP-1 [51]. This revives the question of the mechanical contribution of the TMP-1 matrix in the thread core, as it indicates a possible change of Zn-coordination over time, which would certainly be relevant to the thread maturation process and its mechanical function.

The investigation of the thread cuticle presented in chapter 5 clearly demonstrates that DOPA-metal cross-links via Fe or V are sufficient to account for more than 80% of the modulus and hardness of the epoxy-like biological coating. More importantly from a biological perspective, cuticles reinforced by Fe are mechanically indistinguishable from V-fortified cuticles, further highlighting the opportunistic and adaptive features of the material. The current studies were limited to investigation of the contribution of Fe and V; however, the results suggest that any metals able to bind to DOPA with a high enough affinity could fulfill the role as cross-linking agent. Based on these findings, it is tempting to speculate that the stiffening and hardening of the cuticle via metal-DOPA-based cross-linking could be the evolutionary outcome resulting from a life as a sessile organism in a constantly varying and unpredictable environment. Thus, an interesting follow-up study would be to investigate the mechanical recovery of the cuticle properties following rescue with other

metal ions with known affinity to DOPA (e.g. Al, Ti, Cr and Mn). Furthermore, calcium is found in the thread cuticle in high concentration, but is not known to have a strong affinity for DOPA. Future studies should aim at determining what, if any, contribution Ca makes to the cuticle mechanical properties. As a final point, the transient nature of the DOPA-metal cross-links in the cuticle have previously been proposed to enable cuticle self-healing following the propagation of micro cracks in between granules due to extensive tensile deformation [46]; however, this has not been confirmed. Future, studies should focus on clarifying this matter, perhaps by indenting thread cuticles and monitoring cuticle indents over time or by performing tensile testing on the cuticle within an environmental SEM.

The lessons from the combined investigation of the thread core and cuticle highlight the versatility of metal-protein cross-links in influencing the mechanical properties of (bio)polymeric materials. For example, the dynamic nature of metal-protein cross-links allows them to act as reversible sacrificial bonds in the self-healing thread core, whereas in the cuticle it provides the compatibility of the cross-link with other metals necessary for the adaptability of this protective layer to various circumstances (i.e. constantly changing metal availability). Other types of non-covalent interactions may provide similar dynamics, and covalent bonds may be able to provide superior strength of cross-links; however, metal-coordination based cross-links are uniquely capable of providing both features simultaneously. It is perhaps for this reason that the list of biological materials discovered to utilize metal coordination for various specific functions continues to grow [138]. Clearly, the current work demonstrates the validity and potential for expanding the search for new materials.

Following the discovery of metal-protein bonds in the byssus and their proposed roles in underwater adhesion and self-healing, polymer scientists were quick to follow suit by developing so-called “mussel-inspired” metallopolymers that mimic the metal-binding chemistry of either the DOPA-metal or His-metal cross-links [35,25,36]. The current generation of polymeric mimics consists primarily of soft hydrogels based on PEG chains functionalized with either catechol or imidazole and stabilized with appropriate metal ions (e.g. Fe, V, Zn, Cu, Co and Ni). While the metallopolymeric gels are able to reform after being fractured (i.e. self-heal), they exhibit stiffness properties that are 10^5 to 10^7 -fold lower than the core and cuticle, respectively (comparing storage modulus G' of the gels and reduced elastic modulus E_r of the core and cuticle) [35,46,25,36]. Thus, while these materials are certainly capable of healing catastrophic failure, they inherently lack the security features of the byssal threads for preventing the occurrence of catastrophic failure in the first place. The byssal threads, therefore, still hold a remarkable amount of information on how to build not only a self-healing but also a damage-tolerant material that is capable of self-healing. The incorporation of metal-mediated cross-links into polymer systems represents a major step towards the development of self-healing damage-tolerant materials. However, this study strengthens the hypothesis that the topology and organization of the incorporated cross-links at multiple length scales plays a major role in their function as reversible sacrificial bonds. For example, as described by Krauss et al. [49], the addition of an elastic framework

(i.e. hierarchy) as present in the mussel byssal threads is beneficial for initiating the recoil of the released hidden length, which is necessary to enable the healing of metal-mediated cross-links. The incorporation of these concepts should enable the development of the longed-for self-healing and damage-tolerant polymers.

7 REFERENCES

1. Fratzl P: ***Biomimetic materials research: what can we really learn from nature's structural materials?*** *Journal of The Royal Society Interface* 2007, **4**:637–642.
2. Dunlop JWC, Fratzl P: ***Multilevel architectures in natural materials.*** *Scripta Materialia* 2013, **68**:8–12.
3. Dunlop JWC, Fratzl P: ***Biological Composites.*** *Annual Review of Materials Research* 2010, **40**:1–24.
4. Fratzl P, Weinkamer R: ***Nature's hierarchical materials.*** *Progress in Materials Science* 2007, **52**:1263–1334.
5. Jackson AP, Vincent JFV, Turner RM: ***The Mechanical Design of Nacre.*** *Proceedings of the Royal Society of London. Series B, Biological Sciences* 1988, **234**:415–440.
6. Weinkamer R, Dunlop JWC, Bréchet Y, Fratzl P: ***All but diamonds - Biological materials are not forever.*** *Acta Materialia* 2013, **61**:880–889.
7. Dunlop JWC, Weinkamer R, Fratzl P: ***Artful interfaces within biological materials.*** *Materials Today* 2011, **14**:70–78.
8. Chawla KK: ***Composite Materials: Science and Engineering.*** Springer; 2012.
9. Rest M van der, Garrone R: ***Collagen family of proteins.*** *The FASEB Journal* 1991, **5**:2814–23.
10. Schliwa M, Blerkom J van: ***Structural interaction of cytoskeletal components.*** *The Journal of Cell Biology* 1981, **90**:222–235.
11. Knight DP, Vollrath F: ***Comparison of the Spinning of Selachian Egg Case Ply Sheets and Orb Web Spider Dragline Filaments.*** *Biomacromolecules* 2001, **2**:323–334.
12. Lewis RV: ***Spider silk: the unraveling of a mystery.*** *Accounts of Chemical Research* 1992, **25**:392–398.
13. Rising A, Nimmervoll H, Grip S, Fernandez-Arias A, Storckenfeldt E, Knight DP, Vollrath F, Engström W: ***Spider Silk Proteins - Mechanical Property and Gene Sequence.*** *Zoological Science* 2005, **22**:273–281.
14. Shao Z, Vollrath F: ***Materials: Surprising strength of silkworm silk.*** *Nature* 2002, **418**:741–741.
15. Vollrath F, Knight DP: ***Liquid crystalline spinning of spider silk.*** *Nature* 2001, **410**:541–548.
16. Knight DP, Hunt S: ***Fibril structure of collagen in egg capsule of dogfish.*** *Nature* 1974, **249**:379–380.

17. Rapoport HS, Shadwick RE: ***Mechanical Characterization of an Unusual Elastic Biomaterial from the Egg Capsules of Marine Snails (Busycon spp.)***. *Biomacromolecules* 2002, **3**:42–50.
18. Waite JH: ***The formation of mussel byssus: anatomy of a natural manufacturing process***. *Results and problems in cell differentiation* 1992, **19**:27–54.
19. Waite JH, Qin X-X, Coyne KJ: ***The peculiar collagens of mussel byssus***. *Matrix Biology* 1998, **17**:93–106.
20. Yonge CM: ***On The Primitive Significance of the Byssus in the Bivalvia and its Effects in Evolution***. *Journal of the Marine Biological Association of the United Kingdom* 1962, **42**:113–125.
21. Tainer JA, Roberts VA, Getzoff ED: ***Metal-binding sites in proteins***. *Current Opinion in Biotechnology* 1991, **2**:582–591.
22. Holm RH, Kennepohl P, Solomon EI: ***Structural and Functional Aspects of Metal Sites in Biology***. *Chemical Reviews* 1996, **96**:2239–2314.
23. Chang X, Jørgensen AMM, Bardrum P, Led JJ: ***Solution Structures of the R6 Human Insulin Hexamer***. *Biochemistry* 1997, **36**:9409–9422.
24. Lee H, Scherer NF, Messersmith PB: ***Single-molecule mechanics of mussel adhesion***. *Proceedings of the National Academy of Sciences* 2006, **103**:12999–13003.
25. Holten-Andersen N, Harrington MJ, Birkedal H, Lee BP, Messersmith PB, Lee KYC, Waite JH: ***pH-induced metal-ligand cross-links inspired by mussel yield self-healing polymer networks with near-covalent elastic moduli***. *Proceedings of the National Academy of Sciences* 2011, **108**:2651–2655.
26. Birkedal H, Khan RK, Slack N, Broomell C, Lichtenegger HC, Zok F, Stucky GD, Waite JH: ***Halogenated Veneers: Protein Cross-Linking and Halogenation in the Jaws of Nereis, a Marine Polychaete Worm***. *ChemBioChem* 2006, **7**:1392–1399.
27. Broomell CC, Mattoni MA, Zok FW, Waite JH: ***Critical role of zinc in hardening of Nereis jaws***. *J Exp Biol* 2006, **209**:3219–3225.
28. Lichtenegger HC, Schöberl T, Ruokolainen JT, Cross JO, Heald SM, Birkedal H, Waite JH, Stucky GD: ***Zinc and mechanical prowess in the jaws of Nereis, a marine worm***. *Proceedings of the National Academy of Sciences* 2003, **100**:9144–9149.
29. Politi Y, Priewasser M, Pippel E, Zaslansky P, Hartmann J, Siegel S, Li C, Barth FG, Fratzl P: ***A Spider's Fang: How to Design an Injection Needle Using Chitin-Based Composite Material***. *Advanced Functional Materials* 2012, **22**:2519–2528.
30. Harrington MJ, Masic A, Holten-Andersen N, Waite JH, Fratzl P: ***Iron-Clad Fibers: A Metal-Based Biological Strategy for Hard Flexible Coatings***. *Science* 2010, **328**:216–220.

31. Holten-Andersen N, Mates TE, Toprak MS, Stucky GD, Zok FW, Waite JH: ***Metals and the Integrity of a Biological Coating: The Cuticle of Mussel Byssus***. *Langmuir* 2009, **25**:3323–3326.
32. Holten-Andersen N, Zhao H, Waite JH: ***Stiff Coatings on Compliant Biofibers: The Cuticle of *Mytilus californianus* Byssal Threads***. *Biochemistry* 2009, **48**:2752–2759.
33. Harrington MJ, Gupta HS, Fratzl P, Waite JH: ***Collagen insulated from tensile damage by domains that unfold reversibly: In situ X-ray investigation of mechanical yield and damage repair in the mussel byssus***. *Journal of Structural Biology* 2009, **167**:47–54.
34. Harrington MJ, Waite JH: ***Holdfast heroics: comparing the molecular and mechanical properties of *Mytilus californianus* byssal threads***. *J Exp Biol* 2007, **210**:4307–4318.
35. Fullenkamp DE, He L, Barrett DG, Burghardt WR, Messersmith PB: ***Mussel-Inspired Histidine-Based Transient Network Metal Coordination Hydrogels***. *Macromolecules* 2013, **46**:1167–1174.
36. Krogsgaard M, Behrens MA, Pedersen JS, Birkedal H: ***Self-Healing Mussel-Inspired Multi-pH-Responsive Hydrogels***. *Biomacromolecules* 2013, **14**:297–301.
37. Chiffolleau J-F, Chauvaud L, Amouroux D, Barats A, Dufour A, Pécheyran C, Roux N: ***Nickel and vanadium contamination of benthic invertebrates following the “Erika” wreck***. *Aquatic Living Resources* 2004, **17**:273–280.
38. Coombs TL, Keller PJ: ***Mytilus byssal threads as an environmental marker for metals***. *Aquatic Toxicology* 1981, **1**:291–300.
39. Szefer P, Frelek K, Szefer K, Lee C-B, Kim B-S, Warzocha J, Zdrojewska I, Ciesielski T: ***Distribution and relationships of trace metals in soft tissue, byssus and shells of *Mytilus edulis trossulus* from the southern Baltic***. *Environmental Pollution* 2002, **120**:423–444.
40. Szefer P, Ikuta K, Kushiyama S, Szefer K, Frelek K, Geldon J: ***Distribution and Association of Trace Metals in Soft Tissue and Byssus of *Mytilus edulis* from the East Coast of Kyushu Island, Japan***. *Archives of Environmental Contamination and Toxicology* 1997, **32**:184–190.
41. Szefer P, Kim B-S, Kim C-K, Kim E-H, Lee C-B: ***Distribution and coassociations of trace elements in soft tissue and byssus of *Mytilus galloprovincialis* relative to the surrounding seawater and suspended matter of the southern part of the Korean Peninsula***. *Environmental Pollution* 2004, **129**:209–228.
42. Szefer P, Szefer K: ***Metals in molluscs and associated bottom sediments of the southern baltic***. *Helgoländer Meeresuntersuchungen* 1990, **44**:411–424.
43. Lu Q, Danner E, Waite JH, Israelachvili JN, Zeng H, Hwang DS: ***Adhesion of mussel foot proteins to different substrate surfaces***. *Journal of The Royal Society Interface* 2013, **10**:1–11.

44. Silverman H, Roberto F: **Understanding Marine Mussel Adhesion.** *Marine Biotechnology* 2007, **9**:661–681.
45. Benedict CV, Waite JH: **Composition and ultrastructure of the byssus of *Mytilus edulis*.** *Journal of Morphology* 1986, **189**:261–270.
46. Holten-Andersen N, Fantner GE, Hohlbauch S, Waite JH, Zok FW: **Protective coatings on extensible biofibres.** *Nat Mater* 2007, **6**:669–672.
47. Gosline J, Lillie M, Carrington E, Guerette P, Ortlepp C, Savage K: **Elastic proteins: biological roles and mechanical properties.** *Philosophical Transactions of the Royal Society of London. Series B: Biological Sciences* 2002, **357**:121–132.
48. Bell E, Gosline J: **Mechanical design of mussel byssus: material yield enhances attachment strength.** *J Exp Biol* 1996, **199**:1005–1017.
49. Krauss S, Metzger TH, Fratzl P, Harrington MJ: **Self-Repair of a Biological Fiber Guided by an Ordered Elastic Framework.** *Biomacromolecules* 2013, **14**:1520–1528.
50. Vaccaro E, Waite JH: **Yield and Post-Yield Behavior of Mussel Byssal Thread: A Self-Healing Biomolecular Material.** *Biomacromolecules* 2001, **2**:906–911.
51. Sagert J, Waite JH: **Hyperunstable matrix proteins in the byssus of *Mytilus galloprovincialis*.** *J Exp Biol* 2009, **212**:2224–2236.
52. Waite JH, Vaccaro E, Sun C, Lucas JM: **Elastomeric gradients: a hedge against stress concentration in marine holdfasts?** *Philosophical Transactions of the Royal Society of London. Series B: Biological Sciences* 2002, **357**:143–153.
53. Sun C, Waite JH: **Mapping Chemical Gradients within and along a Fibrous Structural Tissue, Mussel Byssal Threads.** *Journal of Biological Chemistry* 2005, **280**:39332–39336.
54. Hassenkam T, Gutschmann T, Hansma P, Sagert J, Waite JH: **Giant Bent-Core Mesogens in the Thread Forming Process of Marine Mussels.** *Biomacromolecules* 2004, **5**:1351–1355.
55. Hagenau A, Papadopoulos P, Kremer F, Scheibel T: **Mussel collagen molecules with silk-like domains as load-bearing elements in distal byssal threads.** *Journal of Structural Biology* 2011, **175**:339–347.
56. Estapé D, Rinas U: **Folding Kinetics of the All- β -sheet Protein Human Basic Fibroblast Growth Factor, a Structural Homolog of Interleukin-1 β .** *Journal of Biological Chemistry* 1999, **274**:34083–34088.
57. Xu Y, Bunagan MR, Tang J, Gai F: **Probing the Kinetic Cooperativity of β -Sheet Folding Perpendicular to the Strand Direction.** *Biochemistry* 2008, **47**:2064–2070.
58. Xu Y, Purkayastha P, Gai F: **Nanosecond Folding Dynamics of a Three-Stranded β -Sheet.** *Journal of the American Chemical Society* 2006, **128**:15836–15842.

59. Lucas JM, Vaccaro E, Waite JH: **A molecular, morphometric and mechanical comparison of the structural elements of byssus from *Mytilus edulis* and *Mytilus galloprovincialis*.** *J Exp Biol* 2002, **205**:1807–1817.
60. Schmidt S, Reinecke A, Wojcik F, Pussak D, Hartmann L, Harrington MJ: **Metal-Mediated Molecular Self-Healing in Histidine-Rich Mussel Peptides.** *Biomacromolecules* 2014, **15**:1644–1652.
61. Cook M: **Composition of Mussel and Barnacle Deposits at the Attachment Interface.** In *Adhesion in Biological Systems*. Edited by Manly RS. Academic Press; 1970:139–150.
62. Haemers S, Leeden MC van der, Frens G: **Coil dimensions of the mussel adhesive protein *Mefp-1*.** *Biomaterials* 2005, **26**:1231–1236.
63. Hwang DS, Zeng H, Masic A, Harrington MJ, Israelachvili JN, Waite JH: **Protein- and Metal-dependent Interactions of a Prominent Protein in Mussel Adhesive Plaques.** *Journal of Biological Chemistry* 2010, **285**:25850–25858.
64. Taylor SW, Chase DB, Emptage MH, Nelson MJ, Waite JH: **Ferric Ion Complexes of a DOPA-Containing Adhesive Protein from *Mytilus edulis*.** *Inorganic Chemistry* 1996, **35**:7572–7577.
65. Tamarin A, Keller PJ: **An ultrastructural study of the byssal thread forming system in *Mytilus*.** *Journal of Ultrastructure Research* 1972, **40**:401–416.
66. Zuccarello LV: **The collagen gland of *Mytilus galloprovincialis*: An ultrastructural and cytochemical study on secretory granules.** *Journal of Ultrastructure Research* 1980, **73**:135–147.
67. Fullenkamp DE, Barrett DG, Miller DR, Kurutz JW, Messersmith P: **pH-dependent cross-linking of catechols through oxidation via Fe^{3+} and potential implications for mussel adhesion.** *RSC Adv.* 2014, **4**:25127–25134.
68. Harrington MJ, Waite JH: **pH-Dependent Locking of Giant Mesogens in Fibers Drawn from Mussel Byssal Collagens.** *Biomacromolecules* 2008, **9**:1480–1486.
69. Zuccarello LV: **Ultrastructural and cytochemical study on the enzyme gland of the foot of a mollusc.** *Tissue and Cell* 1981, **13**:701–713.
70. Edel J, Sabbioni E: **Accumulation, distribution and form of vanadate in the tissues and organelles of the mussel *Mytilus edulis* and the goldfish *Carassius auratus*.** *Science of The Total Environment* 1993, **133**:139–151.
71. Koide M, Lee DS, Goldberg ED: **Metal and transuranic records in mussel shells, byssal threads and tissues.** *Estuarine, Coastal and Shelf Science* 1982, **15**:679–695.
72. Martincić D, Nürnberg HW, Stoepler M, Branica M: **Bioaccumulation of heavy metals by bivalves from Lim Fjord (North Adriatic Sea).** *Marine Biology* 1984, **81**:177–188.

73. Ólafsson J: **Trace metals in mussels (*Mytilus edulis*) from southwest Iceland.** *Marine Biology* 1986, **90**:223–229.
74. George SG, Pirie BJS, Coombs TL: **The kinetics of accumulation and excretion of ferric hydroxide in *Mytilus edulis* (L.) and its distribution in the tissues.** *Journal of Experimental Marine Biology and Ecology* 1976, **23**:71–84.
75. Miramand P, Guary JC, Fowler SW: **Vanadium transfer in the mussel *Mytilus galloprovincialis*.** *Marine Biology* 1980, **56**:281–293.
76. Punt A., Millward G., Jones M.: **Uptake and depuration of ⁶³Ni by *Mytilus edulis*.** *Science of The Total Environment* 1998, **214**:71–78.
77. Atkins P, Paula J de: **Physical Chemistry.** W. H. Freeman and Company; 2006.
78. Kelly S.D. Hesterberg D., Ravel B: **Analysis of Soils and Minerals Using X-ray Absorption Spectroscopy.** In *Methods of Soil Analysis*. Edited by Ulery AL, Drees LR. Soil Science Society of America, Madison, WI, USA; 2008:387–463.
79. Teo BK: **EXAFS: Basic Principles and Data Analysis.** Springer; 1986.
80. Newville M: **Fundamentals of XAFS.** *Reviews in Mineralogy and Geochemistry* 2014, **78**:33–74.
81. Koningsberger DC, Prins R (Eds): **X-Ray Absorption: Principles, Applications, Techniques of EXAFS, SEXAFS and XANES.** John Wiley & Sons, Ltd; 1988.
82. Politi Y, Zizak I: **Biom mineralization Sourcebook: Characterization of Biominerals and Biomimetic Materials.** In *Biom mineralization Sourcebook: Characterization of Biominerals and Biomimetic Materials*. Edited by DiMasi E, Gower LB. CRC Press; 2014:95–113.
83. Ravel B, Newville M: **ATHENA, ARTEMIS, HEPHAESTUS: data analysis for X-ray absorption spectroscopy using IFEFFIT.** *Journal of Synchrotron Radiation* 2005, **12**:537–541.
84. Ferraro JR, Nakamoto K, Brown CW: **Introductory Raman Spectroscopy.** Academic Press; 1994.
85. Smith E, Dent G: **Modern Raman Spectroscopy - A Practical Approach.** John Wiley & Sons, Ltd; 2005.
86. Chalmers JM, Griffith PR: **Handbook of Vibrational Spectroscopy.** John Wiley & Sons, Ltd; 2001.
87. Frisk S., Ikeda RM., Chase DB., Rabolt JF.: **Rotational Invariants for Polarized Raman Spectroscopy.** *Applied Spectroscopy* 2003, **57**:1053–1057.
88. Lefèvre T, Rousseau ME, Pezolet M: **Orientation-insensitive spectra for Raman microspectroscopy.** *Applied Spectroscopy* 2006, **60**:841–846.

89. Skoog DA, Leary JJ: ***Instrumentelle Analytik***. Springer; 1996.
90. Hou X, Jones BT: ***Inductively Coupled Plasma-Optical Emission Spectrometry***. In *Encyclopedia of Analytical Chemistry*. John Wiley & Sons, Ltd; 2006.
91. Hirs CHW, Moore S, Stein WH: ***Isolation of Amino Acids By Chromatography On Ion Exchange Columns - Use of Volatile Buffers***. *Journal of Biological Chemistry* 1952, **195**:669–683.
92. Moore S, Stein WH: ***Chromatography of Amino Acids On Sulfonated Polystyrene Resins***. *Journal of Biological Chemistry* 1951, **192**:663–681.
93. Rutherford SM, Gilani GS: ***Amino Acid Analysis***. In *Current Protocols in Protein Science*. John Wiley & Sons, Inc.; 2009.
94. Cohen G, Yakushin S, Dembiec-Cohen D: ***Protein L-Dopa as an Index of Hydroxyl Radical Attack on Protein Tyrosine***. *Analytical Biochemistry* 1998, **263**:232–239.
95. Oliver WC, Pharr GM: ***An improved technique for determining hardness and elastic modulus using load and displacement sensing indentation experiments***. *Journal of Materials Research* 1992, **7**:1564–1583.
96. Lefèvre T, Rousseau M-E, Pezolet M: ***Protein Secondary Structure and Orientation in Silk as Revealed by Raman Spectromicroscopy***. *Biophysical Journal* 2007, **92**:2885–2895.
97. Andreini C, Bertini I, Cavallaro G: ***Minimal Functional Sites Allow a Classification of Zinc Sites in Proteins***. *PLoS ONE* 2011, **6**:1–13.
98. Schrödinger L: ***The PyMOL Molecular Graphics System, Version 1.3r1***. 2010, [no volume].
99. Kleifeld O, Steen PE Van den, Frenkel A, Cheng F, Jiang HL, Opdenakker G, Sagi I: ***Structural Characterization of the Catalytic Active Site in the Latent and Active Natural Gelatinase B from Human Neutrophils***. *Journal of Biological Chemistry* 2000, **275**:34335–34343.
100. Miura T, Satoh T, Hori-i A, Takeuchi H: ***Raman marker bands of metal coordination sites of histidine side chains in peptides and proteins***. *Journal of Raman Spectroscopy* 1998, **29**:41–47.
101. Takeuchi H: ***Raman structural markers of tryptophan and histidine side chains in proteins***. *Biopolymers* 2003, **72**:305–317.
102. Ji Ji RD, Balakrishnan G, Hu Y, Spiro TG: ***Intermediacy of Poly(I-proline) II and β -Strand Conformations in Poly(I-lysine) β -Sheet Formation Probed by Temperature-Jump/UV Resonance Raman Spectroscopy***. *Biochemistry* 2006, **45**:34–41.
103. Chi Z, Chen XG, Holtz JSW, Asher SA: ***UV Resonance Raman-Selective Amide Vibrational Enhancement: Quantitative Methodology for Determining Protein Secondary Structure***. *Biochemistry* 1998, **37**:2854–2864.

104. Frushour BG, Koenig JL: **Raman scattering of collagen, gelatin, and elastin.** *Biopolymers* 1975, **14**:379–391.
105. Harrington MJ, Wasco SS, Masic A, Fischer FD, Gupta HS, Fratzl P: **Pseudoelastic behaviour of a natural material is achieved via reversible changes in protein backbone conformation.** *Journal of The Royal Society Interface* 2012, **9**:2911–2922.
106. Movasaghi Z, Rehman S, Rehman IU: **Raman Spectroscopy of Biological Tissues.** *Applied Spectroscopy Reviews* 2007, **42**:493–541.
107. Frankaer CG, Knudsen MV, Noren K, Nazarenko E, Stahl K, Harris P: **The structures of T6, T3R3 and R6 bovine insulin: combining X-ray diffraction and absorption spectroscopy.** *Acta Crystallographica Section D* 2012, **68**:1259–1271.
108. Harding MM, Nowicki MW, Walkinshaw MD: **Metals in protein structures: a review of their principal features.** *Crystallography Reviews* 2010, **16**:247–302.
109. Dudev T, Lin, Dudev M, Lim C: **First - Second Shell Interactions in Metal Binding Sites in Proteins: A PDB Survey and DFT/CDM Calculations.** *Journal of the American Chemical Society* 2003, **125**:3168–3180.
110. Nabavi SS, Harrington MJ, Fratzl P, Hartmann MA: **Influence of sacrificial bonds on the mechanical behaviour of polymer chains.** *Bioinspired, Biomimetic and Nanobiomaterials* 2014, **3**:139–145.
111. Nabavi SS, Harrington MJ, Paris O, Fratzl P, Hartmann MA: **The role of topology and thermal backbone fluctuations on sacrificial bond efficacy in mechanical metalloproteins.** *New Journal of Physics* 2014, **16**:013003.
112. Cao Y, Yoo T, Li H: **Single molecule force spectroscopy reveals engineered metal chelation is a general approach to enhance mechanical stability of proteins.** *Proceedings of the National Academy of Sciences* 2008, **105**:11152–11157.
113. Arnold FH, Zhang J-H: **Metal-mediated protein stabilization.** *Trends in Biotechnology* 1994, **12**:189–192.
114. Shen T, Cao Y, Zhuang S, Li H: **Engineered Bi-Histidine Metal Chelation Sites Map the Structure of the Mechanical Unfolding Transition State of an Elastomeric Protein Domain GB1.** *Biophysical Journal* 2012, **103**:807–816.
115. Auld D: **The ins and outs of biological zinc sites.** *BioMetals* 2009, **22**:141–148.
116. Kiefer LL, Paterno SA, Fierke CA: **Hydrogen bond network in the metal binding site of carbonic anhydrase enhances zinc affinity and catalytic efficiency.** *Journal of the American Chemical Society* 1995, **117**:6831–6837.
117. Onuchic JN, Luthey-Schulten Z, Wolynes PG: **Theory of Protein Folding: The Energy Landscape Perspective.** *Annual Review of Physical Chemistry* 1997, **48**:545–600.

118. Hagenau A, Scheidt HA, Serpell L, Huster D, Scheibel T: ***Structural Analysis of Proteinaceous Components in Byssal Threads of the Mussel Mytilus galloprovincialis***. *Macromol. Biosci.* 2009, **9**:162–168.
119. Carrington E: ***The Ecomechanics of Mussel Attachment: From Molecules to Ecosystems***. *Integrative and Comparative Biology* 2002, **42**:846–852.
120. Holten-Andersen N, Jaishankar A, Harrington MJ, Fullenkamp DE, DiMarco G, He L, McKinley GH, Messersmith PB, Lee KYC: ***Metal-coordination: using one of nature's tricks to control soft material mechanics***. *J. Mater. Chem. B* 2014, **2**:2467–2472.
121. R Core Team: ***R: A Language and Environment for Statistical Computing***. R Foundation for Statistical Computing; 2014.
122. Fox J: ***The R Commander: A Basic Statistics Graphical User Interface to R***. *Journal of Statistical Software* 2005, **14**:1–42.
123. Giraudoux P: ***pgirmess: Data analysis in ecology***. 2013.
124. Siegel S, Castellan NJ: ***Nonparametric statistics for the behavioral sciences***. MacGraw Hill Int.; 1988.
125. Sever MJ, Wilker JJ: ***Visible absorption spectra of metal-catecholate and metal-tironate complexes***. *Dalton Trans.* 2004, **7**:1061–1072.
126. Andersson KK, Cox DD, Que L, Flatmark T, Haavik J: ***Resonance Raman studies on the blue-green-colored bovine adrenal tyrosine 3-monooxygenase (tyrosine hydroxylase). Evidence that the feedback inhibitors adrenaline and noradrenaline are coordinated to iron***. *Journal of Biological Chemistry* 1988, **263**:18621–6.
127. Michaud-Soret I, Andersson KK, Que L, Haavik J: ***Resonance Raman Studies of Catecholate and Phenolate Complexes of Recombinant Human Tyrosine Hydroxylase***. *Biochemistry* 1995, **34**:5504–5510.
128. Öhrström L, Michaud-Soret I: ***Quantum Chemical Approach to the Assignment of Iron-Catecholate Vibrations and Isotopic Substitution Shifts***. *Journal of the American Chemical Society* 1996, **118**:3283–3284.
129. Broomell CC, Zok FW, Waite JH: ***Role of transition metals in sclerotization of biological tissue***. *Acta Biomaterialia* 2008, **4**:2045–2051.
130. Cole PC, Eckert JM, Williams KL: ***The determination of dissolved and particulate vanadium in sea water by x-ray fluorescence spectrometry***. *Analytica Chimica Acta* 1983, **153**:61–67.
131. Evans HTJ, Garrels RM: ***Thermodynamic equilibria of vanadium in aqueous systems as applied to the interpretation of the Colorado Plateau ore deposits***. *Geochimica et Cosmochimica Acta* 1958, **15**:131–149.
132. Nielsen LE: ***Cross-Linking-Effect on Physical Properties of Polymers***. *Journal of Macromolecular Science, Part C: Polymer Reviews* 1969, **3**:69–103.

133. Yu J, Wei W, Danner E, Ashley RK, Israelachvili JN, Waite JH: ***Mussel protein adhesion depends on interprotein thiol-mediated redox modulation.*** *Nat Chem Biol* 2011, **7**:588–590.
134. Barrett DG, Fullenkamp DE, He L, Holten-Andersen N, Lee KYC, Messersmith PB: ***pH-Based Regulation of Hydrogel Mechanical Properties Through Mussel-Inspired Chemistry and Processing.*** *Advanced Functional Materials* 2013, **23**:1111–1119.
135. Sever MJ, Weisser JT, Monahan J, Srinivasan S, Wilker JJ: ***Metal-Mediated Cross-Linking in the Generation of a Marine-Mussel Adhesive.*** *Angewandte Chemie International Edition* 2004, **43**:448–450.
136. Keten S, Xu Z, Ihle B, Buehler MJ: ***Nanoconfinement controls stiffness, strength and mechanical toughness of β -sheet crystals in silk.*** *Nat Mater* 2010, **9**:359–367.
137. Miserez A, Guerette PA: ***Phase transition-induced elasticity of α -helical bioelastomeric fibres and networks.*** *Chem. Soc. Rev.* 2013, **42**:1973–1995.
138. Degtyar E, Harrington MJ, Politi Y, Fratzl P: ***Die Bedeutung von Metallionen für die mechanischen Eigenschaften von Biomaterialien auf Proteinbasis.*** *Angewandte Chemie* 2014, **126**:2–23.

8 APPENDIX

8.1 ASSESSMENT OF THE EFFECTS OF DRYING AND RELAXATION ON BYSSAL THREADS

To test the mechanical effect of the sample preparation procedure for the XAS study on *M. californianus* byssal threads, threads were stretched under wet conditions (i.e. approximately 95% rel. humidity) and rested in the strained state under wet or dry (i.e. approximately 5% rel. humidity) conditions. For this test, a tensile stage equipped with a climate chamber was used. The relative humidity of the climate chamber could be adjusted by flushing with water saturated air and nitrogen. This test was carried out for samples loaded to 10% (Figure 35), 25% (Figure 36) and 40% (Figure 37). The resting of strained threads under wet conditions accounts for an approximate 50% decrease in stress over time for all three strain states. When strained wet to 25% or 40% and rested dry, the initial stress decrease (which is due to the time delay until the relative humidity of the climate chamber has been adjusted to the set value) is outbalanced by drying effects. In case of the threads loaded to 10% strain the initial stress is not only recovered, but the stress measured in the fully dried thread exceeds the initial level by approximately 5 MPa. Hence, drying of threads at 10% strain results in stresses which are most likely closer to the stresses at approximately 15% thread strain.

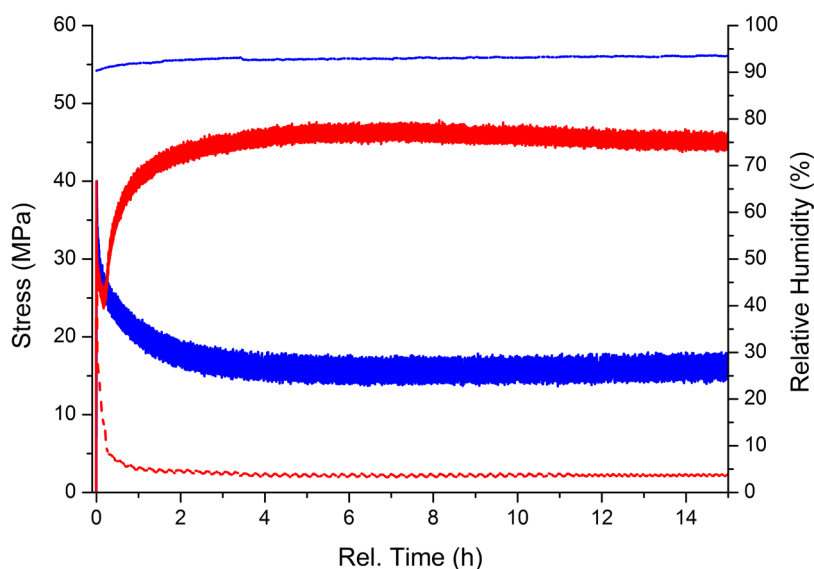


Figure 35 Stress reduction of a byssal thread under wet conditions after deformation to 10% strain (blue) and stress increase of a thread stretched under wet conditions to 10% strain and subsequently dried (red). The thick lines represent the mechanical data and the thin lines the corresponding relative humidity.

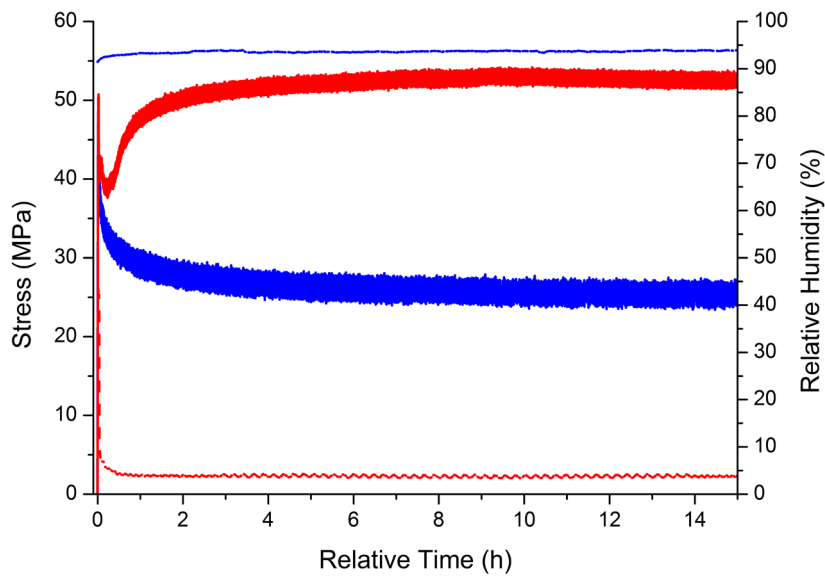


Figure 36 Stress reduction of a byssal thread under wet conditions after deformation to 25% strain (blue) and stress increase of a thread stretched under wet conditions to 25% strain and subsequently dried (red). The thick lines represent the mechanical data and the thin lines the corresponding relative humidity.

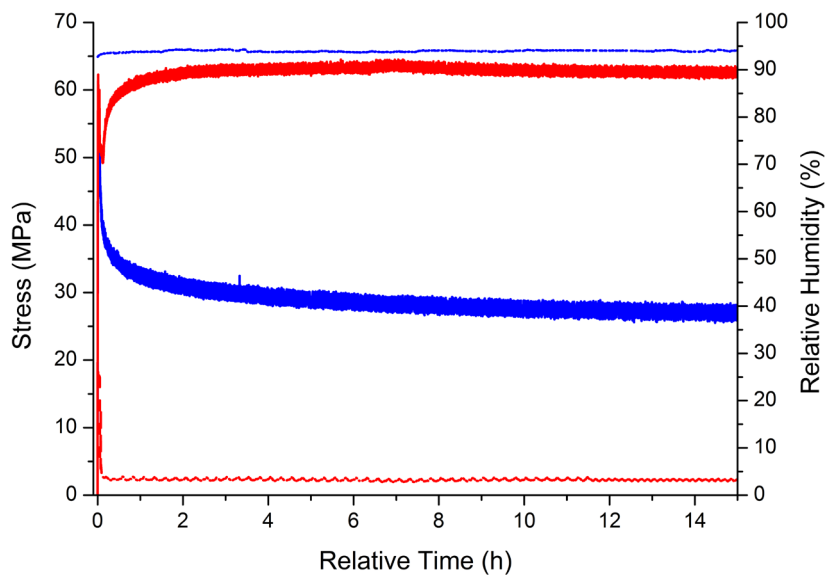


Figure 37 Stress reduction of a byssal thread under wet conditions after deformation to 40% strain (blue) and stress increase of a thread stretched under wet conditions to 40% strain and subsequently dried (red). The thick lines represent the mechanical data and the thin lines the corresponding relative humidity.

8.2 ALTERNATIVE EXAFS FITTING RESULTS FOR N = 4

Table 7 Alternative EXAFS fitting results for Zn K-edge spectra of *M. californianus* byssal threads during tensile loading, relaxation and healing.

EXAFS fitting results										
1 st coordination shell										
sample	s_0^2	E_0 (eV)	N/O _{long}			N/O _{short}				
			R (Å)	N	σ^2 (Å ²)	R (Å)	N	σ^2 (Å ²)		
0% strain	1.13 f	5.02 f	2.01 (0.01)	2.0 (0.1)	0.010 (0.001)	1.95 (<0.01)	2.0 4-N/O _{long}	0.004 (<0.001)		
10% strain	1.09 f	5.26 f	2.02 (0.02)	2.0 (0.2)	0.008 (0.002)	1.97 (<0.01)	2.0 4-N/O _{long}	0.003 (<0.001)		
25% strain	1.12 f	5.26 f	2.05 (0.01)	2.5 (0.7)	0.006 (<0.001)	1.96 (<0.01)	1.5 4-N/O _{long}	0.006 (<0.001)		
40% strain	1.15 f	5.46 f	2.01 (0.01)	3.8 (0.2)	0.006 (<0.001)	-	-	-	-	-
relaxed (25%)	1.18 f	5.26 f	2.05 (0.02)	2.3 (0.5)	0.013 (0.002)	1.98 (<0.01)	1.7 4-N/O _{long}	0.004 (<0.001)		
healed (25%)	1.11 f	5.37 f	2.04 (0.02)	1.6 (0.2)	0.008 (0.001)	1.96 (<0.01)	2.4 4-N/O _{long}	0.010 (<0.001)		
2 nd coordination shell										
sample	s_0^2	E_0 (eV)	C _{long}			C _{short}				
			R (Å)	N	σ^2 (Å ²)	R (Å)	N	σ^2 (Å ²)		
0% strain	1.13 f	5.02 f	2.89 (0.01)	3.9 2xN/O _{long}	0.014 (0.002)	2.57 (0.02)	1.0 ½xN/O _{short}	0.008 (0.002)		
10% strain	1.09 f	5.26 f	2.92 (0.01)	4.0 2xN/O _{long}	0.007 (0.002)	2.58 (0.01)	1.0 ½xN/O _{short}	0.011 (0.003)		
25% strain	1.12 f	5.26 f	2.95 (0.01)	3.5 (1.0)	0.012 (0.003)	2.66 (0.02)	2.0 (0.4)	0.004 (0.004)		
40% strain	1.15 f	5.46 f	2.91 (0.02)	1.9 (1.1)	0.014 (0.005)	2.54 (0.02)	0.8 (0.3)	0.011 (0.005)		
relaxed (25%)	1.18 f	5.26 f	2.85 (0.01)	3.7 (0.9)	0.015 (0.004)	2.52 (0.01)	1.0 ½xN/O _{short}	0.007 (0.004)		
healed (25%)	1.11 f	5.37 f	2.90 (0.01)	3.2 2xN/O _{long}	0.003 (0.002)	2.58 (0.02)	1.2 ½xN/O _{short}	0.003 (0.002)		

The overall degeneracy of 1st shell paths (N/O) was set to 4. s_0^2 was allowed to vary from the experimentally determined value from the fits of the standards. Numbers in parentheses are fit uncertainties. If no uncertainty is given, the formula for the calculation of the parameter is stated.

9 ACKNOWLEDGEMENTS

When I first started to work on this topic I quickly realized how far off this was from anything I had ever worked on before. I, therefore, thank my supervisor Matt Harrington for putting his trust in a trained botanist to be his first PhD student in a project dominated by biochemistry. He is, as he would probably phrase it, a “wicked cool” dude, friend and supervisor, who did everything I could hope for to help me. A group leader like Matt of course reflects in the type of people and atmosphere in our group. In particular I would like to thank Jeannette Steffen, Elena Degtyar, Stefanie Krauss and Antje Reinecke, not only for patiently answering my numerous and at times weird questions, but also for the many hours they spent with me at the synchrotron and in front of other instruments. I also want to thank Robert Seckler and his group at the University of Potsdam, who accepted me as his PhD student and a member of the group.

Speaking of questions brings me to acknowledge the next group of people, namely those who taught me everything I know about the methods applied in this thesis. Thanks go to Yael Politi and Ivo Zizak my local XAS gurus and guides to the world of EXAFS interpretation. I appreciate the introduction to Raman spectroscopy which I received from Admir Masic, Roman Schütz and (again) Matt Harrington, even though that resulted in spending many summer days in that dark Raman room without any windows. I further want to thank Igor Zlotnikov and Petra Leibner for always responding to all those cries for help when doing nanoindentation, and for making the time spent in that lab fun. The tensile testing experiments and sample preparation wouldn't have been possible without the aid and expertise of Michaela Eder, Carmen Weißkopf, Georg Bauer and Luca Bertinetti. A very special thank you goes out to René Genz and the others of the IT team, for constant superb support and recovering my thesis files in the days before submission. Of course I do not only thank all these people for their scientific help, but even more for being friends I was able to count on during my time here at the institute.

I very much enjoyed the atmosphere at the department, which, of course, is due to all the great people who are working here: Agata Olszewska, Marc Widdrat, Christophe Tarabout, Ronald Seidel, Erika Guenther, Felix Repp, John Dunlop, Katharina Tomschek, Sidney Omelon, Susann Weichold, Vanessa Schöppler and Victoria Reichel ... just to name a few of the people who create the great environment that flows through the corridors of our department. This brings me to thank the person responsible for bringing us all together and giving us the opportunity to make this great experience, Peter Fratzl. I enjoyed and learned a lot from the discussions with him and all the others at the department, even though sometimes my brain was hurting afterwards.

Of course I would not be here if it wasn't for my family. I want to thank my parents and sisters for their support, trust and love for the “nutty scientist” who always explained computer problems and high school math in a “too logical” way. I am deeply grateful to my wife Kasia, my son Cajus and “the one to come”, for clearing my head from science when it was necessary, for their support and last, but by no means least, for your unconditional love and acceptance!